

THESIS FOR THE DEGREE OF DOCTOR OF PHILOSOPHY

**The simulation of car and truck tyre vibrations,
rolling resistance and rolling noise**

CARSTEN HOEVER

Department of Civil and Environmental Engineering
Division of Applied Acoustics, Vibroacoustics Group
CHALMERS UNIVERSITY OF TECHNOLOGY
Göteborg, Sweden 2014

The simulation of car and truck tyre vibrations, rolling resistance and rolling noise
CARSTEN HOEVER
ISBN 978-91-7597-056-1

© CARSTEN HOEVER, 2014.

Doktorsavhandlingar vid Chalmers tekniska högskola
Ny serie nr 3737
ISSN 0346-718X

Department of Civil and Environmental Engineering
Division of Applied Acoustics, Vibroacoustics Group
Chalmers University of Technology
SE-412 96 Göteborg
Sweden
Telephone: +46 (0)31-772 2200

Cover:

Contact between road surface (grey) and tyre (coloured) for one time step. For the sake of clarity without tyre profile and not drawn to scale. Clearly visible is how the road asperities deform the tyre.

Printed by
Chalmers Reproservice
Göteborg, Sweden 2014

The simulation of car and truck tyre vibrations, rolling resistance and rolling noise

CARSTEN HOEVER

Department of Civil and Environmental Engineering
Division of Applied Acoustics, Vibroacoustics Group
Chalmers University of Technology

ABSTRACT

The road transportation sector places a severe burden on the environment in the form of CO₂ emissions and road traffic noise. Both of these environmental problems can be related to car and truck tyres. In spite of this, there is a lack of suitable simulation tools for the prediction of rolling noise and rolling resistance and the investigation of the relevant physical processes behind these two quantities.

The purpose of this thesis is to establish a simulation framework which allows for the exploration of the underlying physical processes for rolling resistance and rolling noise. For this, an acoustical tyre/road interaction model aimed at calculating rolling noise is extended and combined with a module for the calculation of rolling losses. The proposed tool consists of a waveguide finite element model of the tyre, which is combined with a non-linear three-dimensional tyre/road contact model to simulate the structural dynamics of a tyre rolling under steady-state conditions on a real road. Rolling resistance is calculated based on the input power into the tyre while the velocity field on the tyre surface is used to determine the radiated sound pressure based on a boundary element method. Tyre vibrations, rolling noise and/or rolling resistance are calculated for different car and truck tyres and a wide selection of road surfaces. There is good agreement with measurements for both quantities, making this the first tool which can be successfully used for the simulation of both rolling resistance and rolling noise. The method is especially suitable for extended parameter studies because of its numerical efficiency.

A number of important research questions are investigated. It is shown that rolling resistance can be split into two parts: one part originating from the large-scale tyre structure deformations, and another part arising from small-scale tread indentations which are highly dependent on road surface texture. An investigation of the free wave propagation on a truck tyre indicates that the structural differences between car and truck tyres lead to some differences in the vibrational behaviour. Additionally, it is investigated how well a certain road surface section is represented by a limited number of road surface scans. It is shown that for most applications and surfaces a minimum number of scan lines from different sample locations are needed if simulation results should be representative of the whole surface.

Keywords: tyres, vibrations, rolling noise, rolling resistance, tyre/road interaction, waveguide finite element, BEM, numerical modelling, road surface properties, parameter study, fuel efficiency

*It isn't the mountain ahead that wears you out;
it is the grain of sand in your shoe.*

List of publications

This thesis is based on the work contained in the following appended papers, referred to by Roman numerals in the text:

Paper I

A comparison between finite element and waveguide finite element methods for the simulation of tire/road interaction.

C. Hoever, A. Tsotras, E.-U. Saemann, and W. Kropp.

In: Proceedings Internoise 2013, Innsbruck, Austria, 15.–18. Sept. 2013.

Paper II

The influence of lateral road surface resolution on the simulation of car tyre rolling losses and rolling noise.

C. Hoever and W. Kropp.

In: Proceedings Internoise 2013, Innsbruck, Austria, 15.–18. Sept. 2013.

Paper III

A model for investigating the influence of road surface texture and tyre tread pattern on rolling resistance.

C. Hoever and W. Kropp.

Submitted to *Journal of Sound and Vibration*.

Paper IV

Simulation of free wave propagation on a truck tyre.

C. Hoever and W. Kropp.

Submitted to *Journal of Sound and Vibration*.

Paper V

The simulation of truck tyre rolling noise.

C. Hoever, W. Kropp, T. Beckenbauer, and H. Brick.

The following publications are not included in this thesis due to an overlap in content or a content going beyond the scope of the thesis:

1. C. Hoever, P. Sabiniarz, and W. Kropp, Investigation of stress-distribution in a car tyre with regards to rolling resistance, in: Proceedings of ISMA2010, Leuven, Belgium, 20–22 September 2010, pp. 3977–3990.
2. C. Hoever, Die effiziente Modellierung des Vibrationsverhaltens eines PKW-Reifens mittels der Waveguide-Finite-Element-Methode, 17. Workshop Physikalische Akustik des Fachausschusses Physikalische Akustik der DEGA und des Fachverbandes Akustik der DPG, Bad Honnef, Germany, 21./22.10.2010 (abstract only).
3. C. Hoever, P. Sabiniarz, and W. Kropp, Waveguide-Finite-Element basierte Parameterstudie zum Rollwiderstand von PKW-Reifen, in: Proceedings DAGA 2011, Düsseldorf, Germany, 21.—24. March 2011, pp. 775–776.
4. C. Hoever, P. Sabiniarz, and W. Kropp, Parameter study of car tyre rolling losses based on waveguide-finite-element modelling, Svenska Mekanikdagar 2011, Chalmers University of Technology, Göteborg, Sweden, 13–15 Juni 2011, p. 129 (abstract only).
5. C. Hoever, P. Sabiniarz, and W. Kropp, Waveguide-finite-element based parameter study of car tyre rolling losses, in: Proceedings 6th Forum Acusticum, Aalborg, Denmark, 2011, pp. 789–794.
6. P. Andersson, C. Hoever, J. Winroth, and W. Kropp, Numerical modelling of tyre/road interaction, Exploratory Workshop: Modern Methods of Vibro-Acoustic Studies With Automotive Applications, University of Pitesti, Romania, November 24–25, 2011.
7. C. Hoever and W. Kropp, Simulationsbasierte Parameterstudie zum Zusammenhang zwischen Rollgeräusch und Rollwiderstand von PKW-Reifen, in: Proceedings DAGA 2012, Darmstadt, Germany, 19.—22. March 2012, pp. 419–420.
8. C. Hoever and W. Kropp, A simulation-based parameter study of car tyre rolling losses and sound generation, in: Proceedings Euronoise 2012, Prague, Czech Republic, 10–13 June 2012, pp. 926–931.
9. P. Andersson, C. Hoever, J. Winroth, and W. Kropp, Numerical modelling of tyre/road interaction, Scientific Bulletin, Automotive Series, 22, 2012.
10. C. Hoever, The influence of modelling parameters on the simulation of car tyre rolling losses and rolling noise, Licentiate thesis, Chalmers University of Technology, Göteborg, Sweden, December 2012.

11. C. Hoever and W. Kropp, The influence of modelling parameters on the simulation of car tyre rolling noise and rolling resistance, in: Proceedings AIA-DAGA 2013, Merano, Italy, 18–21 March 2013, pp. 1601–1604.
12. W. Kropp and C. Hoever, Predicting rolling resistance as function of road surface and tyre profile, in: Proceedings AIA-DAGA 2013, Merano, Italy, 18–21 March 2013, pp. 1605–1608.
13. J. Winroth, C. Hoever, W. Kropp, and T. Beckenbauer, The contribution of air-pumping to tyre/road noise, in: Proceedings AIA-DAGA 2013, Merano, Italy, 18–21 March 2013, pp. 1594–1597.
14. W. Kropp, J. Winroth, C. Hoever, and T. Beckenbauer, Sound generation and sound radiation from tyres, in: Proceedings Internoise 2013, Innsbruck, Austria, 15.–18. Sept. 2013.
15. C. Hoever and W. Kropp, Numerische Simulation von Rollgeräusch und Rollwiderstand von LKW-Antriebsachsenreifen, in: Proceedings DAGA 2014, 10.–13. March 2014, Oldenburg, Germany, pp. 108–109.

Acknowledgements

The initial stages of the research included in this thesis have been financially supported by the European Commission research project *Green City Car*. The funding of the last three years has come from the project *LeiStra3* (Leiser Straßenverkehr 3), financed by the German Federal Ministry for Economic Affairs and Energy, and the German Federal Ministry of Transport and Digital Infrastructure. All financial support is gratefully acknowledged.

I am appreciative of the interesting and fruitful cooperation with the NVH group at Continental Reifen Deutschland. Thank you Uli, thank you Achillefs! I furthermore thank Christina Bückers and Sören Keuchel for the pleasant collaboration within the *LeiStra3* project. Thanks also to Freddy Rietdijk, Victor Finel and Amr Abboud for the help with measurements, to Brett Seward for language support, and to Patrick Sabiniarz for always finding time to answer my questions about the waveguide finite element implementation.

A work like this is never possible without the guidance, support, help, and friendship of other people. I have to thank all my friends and colleagues for the last five years at Applied Acoustics; it has been a pleasure and I am looking forward to more of it! Special hats off to Gunilla and Börje for always keeping things rolling at the division, and to all of you who “volunteered” to proofread this thesis. A special mention to Bart: it’s not your fault that you grew up on the wrong side of the border; otherwise you are the best office mate I could have asked for!

Wolfgang, ein großes Dankeschön! Du hast mich motiviert mich selbst ans Steuer zu setzen und den richtigen Weg zu finden. Hatte ich mich dann mal wieder verfahren, warst Du als Navigator, der sich auch für einen Reifenwechsel nicht zu schade ist, immer zur Stelle.

My family and friends, in Germany and Sweden, shall not be forgotten: you had your part in this as well. Unendlichen Dank meinen Eltern, die mir immer Vorbild und Inspiration sind. Hanna, tack så mycket för allt stöd, uppmuntran och inspiration! Jag är så glad att du finns i mitt liv!

PS: Maybe someone can finally teach me how to correctly pronounce *däckbuller*? I am getting tired of people thinking I am an imaginative baker!

Contents

| | |
|--|--------------|
| List of publications | vii |
| Acknowledgements | xi |
| List of Figures | xviii |
| List of Tables | xix |
| 1 Introduction | 1 |
| 1.1 Background - The environmental impact of car tyre rolling losses and sound radiation | 1 |
| 1.2 Scope of the thesis | 3 |
| 1.3 Outline | 3 |
| 2 On rolling resistance and rolling noise | 5 |
| 2.1 Fundamentals of rolling resistance | 5 |
| 2.2 Fundamentals of rolling noise | 6 |
| 2.2.1 Vibrational mechanisms | 8 |
| 2.2.2 Aerodynamical mechanisms | 11 |
| 2.2.3 Propagation effects | 12 |
| 3 Review of existing models | 15 |
| 3.1 Requirements for a combined rolling resistance and tyre/road noise simulation tool | 15 |
| 3.2 Review of tyre/road noise models | 16 |
| 3.2.1 General overview | 16 |
| 3.2.2 Tyre models | 17 |
| 3.2.3 Contact models | 20 |
| 3.2.4 Radiation models | 23 |
| 3.3 Review of rolling resistance models | 25 |
| 3.4 The proposed simulation tool for rolling resistance and tyre/road noise | 27 |

| | | |
|----------|--|-----------|
| 4 | The tyre/road noise and rolling resistance model | 29 |
| 4.1 | The waveguide finite element tyre model | 29 |
| 4.1.1 | Basic WFE formulation | 29 |
| 4.1.2 | Free response, forced response and damping | 33 |
| 4.1.3 | Element formulation | 36 |
| 4.1.4 | Advantages of WFEM | 37 |
| 4.2 | The tyre/road interaction model | 37 |
| 4.2.1 | Basic contact formulation | 37 |
| 4.2.2 | Small-scale tread/road interaction | 39 |
| 4.2.3 | Implementation details and input parameters | 40 |
| 4.3 | Influence of the tread pattern | 41 |
| 4.4 | The half-space boundary element method radiation model | 43 |
| 4.4.1 | Governing equations | 43 |
| 4.4.2 | Numerical implementation | 45 |
| 4.4.3 | Tyre/road noise specialities | 46 |
| 4.5 | Calculating rolling resistance | 49 |
| 4.6 | Additional remarks on the simulation process | 50 |
| 4.6.1 | Temporal and spatial resolution | 50 |
| 4.6.2 | Conversion between Euler and Lagrange reference system | 50 |
| 4.6.3 | Rotational effects | 51 |
| 4.6.4 | Large-deformation non-linearity | 51 |
| 5 | Estimation of material properties for the WFE tyre model | 53 |
| 5.1 | Available information | 54 |
| 5.2 | Condensation of tyre material properties for shell elements | 55 |
| 5.2.1 | Stress-strain relations for individual layers | 55 |
| 5.2.2 | Force and moment resultants for laminates | 60 |
| 5.2.3 | Transverse shear | 63 |
| 5.2.4 | The elastic stiffness matrix for a shell element | 63 |
| 5.3 | Stiffness parameters for isotropic solid elements | 64 |
| 5.4 | Pre-tension | 65 |
| 5.5 | Viscoelastic material properties | 66 |
| 5.6 | Additional implementation considerations | 67 |
| 5.7 | Modifications for solid element based tyre models | 68 |
| 6 | Application examples | 71 |
| 6.1 | A comparison of FEM and WFEM for the simulation of tyre/road interaction | 71 |
| 6.1.1 | The finite element tyre model | 71 |
| 6.1.2 | Input data | 72 |
| 6.1.3 | Quasi-static simulations | 72 |
| 6.1.4 | Dynamic simulations | 73 |

| | | |
|----------|--|------------|
| 6.1.5 | Concluding remarks | 75 |
| 6.2 | The influence of lateral road surface resolution on rolling loss/noise simulations | 77 |
| 6.2.1 | Road properties | 77 |
| 6.2.2 | Study methodology | 79 |
| 6.2.3 | Results | 80 |
| 6.2.4 | Concluding remarks | 81 |
| 6.3 | Predicting rolling resistance as a function of road surface profile and tyre tread pattern | 82 |
| 6.3.1 | Tyre input data | 83 |
| 6.3.2 | Road properties | 84 |
| 6.3.3 | Rolling resistance calculations | 85 |
| 6.3.4 | Concluding remarks | 88 |
| 6.4 | Simulation of free wave propagation on a truck tyre | 88 |
| 6.4.1 | Dispersion relations | 89 |
| 6.4.2 | Wave shape analysis | 90 |
| 6.4.3 | Concluding remarks | 97 |
| 6.5 | Simulation of truck tyre rolling noise | 98 |
| 6.5.1 | Setup | 98 |
| 6.5.2 | Results | 98 |
| 6.5.3 | Concluding remarks | 101 |
| 7 | Conclusions and future work | 103 |
| 7.1 | Conclusions | 103 |
| 7.2 | Future work | 107 |
| A | Implemented tyre models | 111 |
| A.1 | 205/55 R16 car tyre | 111 |
| A.2 | 175/65 R14 car tyre | 112 |
| A.3 | 315/80 R22.5 truck tyre | 113 |
| B | Simulation configurations | 119 |
| C | Reference frames and coordinate systems | 121 |
| C.1 | Reference frames | 121 |
| C.2 | Coordinate systems | 122 |
| | References | 137 |

List of Figures

| | | |
|------|--|----|
| 2.1 | Main regions of a tyre. | 6 |
| 2.2 | Examples of typical car tyre rolling noise spectra. | 7 |
| 2.3 | Examples of typical truck tyre rolling noise spectra. | 8 |
| 2.4 | Vibrational behaviour of a tyre. | 10 |
| 3.1 | The three parts of tyre/road noise modelling. | 17 |
| 3.2 | The difference between the <i>apparent</i> and <i>real area of contact</i> | 21 |
| 3.3 | Change in contact area during the loading phase. | 21 |
| 4.1 | Flowchart of the rolling noise and rolling loss simulations. | 30 |
| 4.2 | The tyre as a curved waveguide. | 30 |
| 4.3 | WFEM mesh of a slick 205/55 R16 tyre. | 31 |
| 4.4 | Examples of three free response solutions. | 34 |
| 4.5 | Contact geometry between tyre and road. | 38 |
| 4.6 | Small-scale contact modelling using contact springs. | 40 |
| 4.7 | Example of a road surface profile with pronounced unevenness. | 41 |
| 4.8 | Example of tyre/road interaction. | 42 |
| 4.9 | Scaling of contact stiffnesses based on the tread pattern. | 43 |
| 4.10 | Domain definition for the exterior BEM problem. | 44 |
| 4.11 | Tyre, reflecting ground and evaluation surface for BEM. | 46 |
| 4.12 | The effect of static deformation on the BEM mesh. | 48 |
| 4.13 | Rearranging a contact force from Euler to Lagrange. | 51 |
| 5.1 | Tyre cross-section with the most important functional parts. | 54 |
| 5.2 | Comparison of a detailed tyre cross-section and a WFEM mesh. | 55 |
| 5.3 | Shell element. | 56 |
| 5.4 | Fibrous composite layer. | 57 |
| 5.5 | Rotation between principal material axes and shell coordinates. | 59 |
| 5.6 | Laminated shell element. | 60 |
| 5.7 | Solid element. | 64 |
| 5.8 | Tyre cross-section geometry for pre-tension calculations. | 65 |
| 5.9 | Frequency dependency of rubber's Young's modulus. | 67 |
| 6.1 | Size of footprint area for FE and WFE simulations. | 72 |

| | | |
|------|--|-----|
| 6.2 | Load-deflection curves for FE and WFE simulations. | 73 |
| 6.3 | Measured and simulated eigenfrequencies and first modeshapes. . . | 74 |
| 6.4 | Comparison of measured, FE, and WFE mobilities. | 75 |
| 6.5 | Average of road surface profiles. | 78 |
| 6.6 | Road surface spectra and coherence between lateral tracks. | 78 |
| 6.7 | Example of a repetition scheme. | 80 |
| 6.8 | Deviations of rolling loss/noise calculations from reference case. . . | 81 |
| 6.9 | Tyre tread patterns and stiffness scaling factors. | 83 |
| 6.10 | Average <i>MPD</i> for all surfaces. | 84 |
| 6.11 | Measured and simulated C_r rolling resistance. | 85 |
| 6.12 | Tyre and small-scale deformation losses for the CPC tyre. | 86 |
| 6.13 | Distribution of dissipation over the CPC tyre cross-section. | 87 |
| 6.14 | Dispersion relations. | 89 |
| 6.15 | Dispersion relations for symmetric cross-sectional mode shapes. . . | 90 |
| 6.16 | Semi-rigid body modes. | 91 |
| 6.17 | Symmetric out-of-plane cross-sectional mode shapes. | 92 |
| 6.18 | Symmetric in-plane cross-sectional mode shapes. | 92 |
| 6.19 | Symmetric cross-sectional modes with in-/out-of-plane components. | 93 |
| 6.20 | Development of cross-sectional mode shapes for belt extension. . . | 95 |
| 6.21 | Symmetric tread block mode shapes. | 96 |
| 6.22 | Measured and simulated third-octave band rolling noise spectra. . | 99 |
| 6.23 | Comparison of directivity between measurements and simulations. . | 100 |
| | | |
| A.1 | The three tyres modelled in this thesis. | 111 |
| A.2 | Loss factors for the 205/55 R16 tyre. | 112 |
| A.3 | WFEM mesh of the 175/65 R14 tyre. | 112 |
| A.4 | Loss factors for the 175/65 R14 tyre. | 113 |
| A.5 | WFEM mesh of the 315/80 R22.5 tyre. | 114 |
| A.6 | Loss factors for the 315/80 R22.5 tyre. | 114 |
| A.7 | Pre-tension along the tyre cross-section. | 115 |
| A.8 | Input mobilities for the 315/80 R22.5 tyre. | 116 |
| A.9 | Transfer mobilities for the 315/80 R22.5 tyre. | 117 |
| | | |
| C.1 | The Euler and Lagrange reference systems for a rotating tyre. . . . | 121 |
| C.2 | Overview of the different coordinate systems. | 122 |

List of Tables

| | | |
|-----|---|-----|
| 6.1 | Arrangements of lateral tracks used in the simulations. | 79 |
| 6.2 | Considered road surfaces. | 84 |
| B.1 | General simulation parameters. | 119 |
| B.2 | Parameters for the WFE tyre model. | 119 |
| B.3 | Parameters for tyre/road interaction. | 120 |
| B.4 | Parameters for the BEM calculations. | 120 |

1 Introduction

1.1 Background - The environmental impact of car tyre rolling losses and sound radiation

Greenhouse gas emissions and exterior traffic noise are two major environmental issues associated with the road transportation sector. In 2006 the fuel consumption in the road transportation sector was responsible for 23 % of the CO₂ emissions in the European Union (EU) [1] and 26 % in the United States [2]. In both cases the absolute emission values had remained constant or even increased since 1990. It seems unlikely that a reduction of CO₂ emissions can be achieved by a reduction of mileage travelled as there is sustained demand for personal mobility and transportation services in most societies. For Germany, for example, it is predicted that road traffic will increase by 10 % for cars, and by 39 % for trucks, until the year 2030 [3]. Instead, the energy efficiency of existing means of transportation has to be increased in order to reduce the CO₂ emissions.

For vehicles powered by classical combustion engines, only about 10 % to 40 % of the chemical energy stored in the fuel is available as mechanical energy from the engine, the remainder being consumed by engine inefficiency in the form of waste heat [4]. Further reductions caused by friction in the driveline, standby operation or auxiliary appliances (e.g. the A/C system) result in even less mechanical energy being actually available at the axles to drive the wheels. The remaining energy is consumed by aerodynamic drag, rolling resistance and acceleration. Depending on vehicle type and driving conditions, eventually about 5 % to 30 % of the fuel consumption are due to hysteretic losses in the tyres, i.e. rolling resistance [4]. For trucks and other heavy vehicles the energy losses are even higher, ranging from 15 % to 40 %. Accordingly, by decreasing these rolling resistance induced energy losses, the vehicle's fuel consumption can be substantially reduced. The Transportation Research Board of the United States, for example, has come to the conclusion that "a 10 percent reduction in average rolling resistance [...] promises a 1 to 2 percent increase in fuel economy"¹ [5]. Similar numbers have also been reported for the EU [6]. Additionally, Barrand and Bokar [4] have shown that lower rolling resistances not only help in bringing down greenhouse gas emissions but also reduce the release of local pollutants such as CO and NO_x.

¹This equivalent a reduction of the overall yearly fuel consumption in the USA by $3.7 \cdot 10^9$ l to $7.5 \cdot 10^9$ l.

For hybrid and electrically powered cars the influence of the rolling resistance on the overall energy efficiency is expected to be even higher as these vehicle classes feature a greatly improved power train efficiency when compared to vehicles with combustion engines [7]. For these alternative propulsion techniques it is more difficult to assess the actual impact of rolling resistance reductions on greenhouse gas emissions. However, it is safe to assume that an increase in energy efficiency is always ecologically beneficial.

Besides being a significant source of greenhouse gas emissions, the road transportation sector places a further severe burden on a large part of the population in the form of road traffic noise. A recent report by the World Health Organization (WHO) [8] estimates that within the EU about 50 % of the population are regularly exposed to A-weighted road traffic noise levels exceeding the WHO guideline value for outdoor sound levels of 55 dB, and about 10 % to A-weighted road traffic noise levels exceeding 65 dB, i.e. levels with a 20 % to 40 % increased risk for cardiovascular diseases [9]. Other possible noise related health problems include cognitive impairment in children, sleep disturbance, tinnitus and annoyance. As a consequence, the WHO assumes that “at least one million healthy life years are lost every year from traffic-related noise in the western part of Europe” [8]. Although the contribution of noise originating from rail and air traffic cannot be neglected, road traffic noise comprises the main burden of this traffic-related noise [8, 10]. Road traffic noise can be separated into a vehicle’s power train noise, rolling noise and aerodynamic noise. For most vehicle types, including trucks and other heavy vehicles, rolling noise is the dominating noise source at the most common driving speeds of roughly 30 km/h to 100 km/h [11, 12]. Power train noise dominates at lower and aerodynamic noise at higher speeds.

In sum, two of today’s major environmental issues originating from the road transportation sector, namely CO₂ emissions and traffic noise, can be related to tyres. This has been recognised by legislative policy makers, for instance resulting in a new EU-wide labelling scheme for replacement tyres [13] which includes (simplified) information about both the rolling resistance as well as the external rolling noise, or new type approval noise values [14]. In spite of the environmental relevance of tyres with regard to rolling resistance and sound radiation, there is a lack of adequate simulation tools for the investigation of relevant source mechanisms, relations between rolling resistance and rolling noise, or the influence of road surface properties on rolling noise and rolling resistance. This is particularly true for truck tyres.

1.2 Scope of the thesis

The aim of this thesis is to develop a unified tool for the simulation of car and truck tyre rolling noise and rolling resistance. This tool should be detailed enough to capture the relevant properties of the tyre construction and road surface profiles, and to give insight into the fundamental physical source processes for rolling resistance and rolling noise. Yet, it should also be numerically efficient to allow for extended parameter studies, for example for different road surfaces.

For this, an acoustical tyre/road interaction model aimed at calculating rolling noise is extended to allow detailed calculations of rolling losses. Tyre vibrations, rolling noise and/or rolling resistance are calculated for different types of car and truck tyres and a wide selection of road surfaces.

Every numerical simulation is only as good as the input data it is based on. Accordingly, special emphasis is put on the proper definition of tyre input data. A rigorous, yet efficient, scheme for deriving the necessary input data from tyre design data is presented. This facilitates the future use of the simulation package by reducing the necessary implementation effort for new tyres and allowing for more detailed design variations in parameter studies. Additionally, some minimum requirements for the road roughness data used in the tyre/road contact simulations are determined.

Modelling tyre vibrations, rolling resistance and/or rolling noise is a complex task which involves several different simulation stages. At each of these stages decisions about certain modelling parameters have to be made. For validation purposes, results from different simulation stages are compared to measurements or data from the manufacturer's tyre design process whenever possible.

As a final note it shall be added that only exterior rolling noise is covered in this thesis. No efforts are made to investigate the influence of tyre/road interaction on noise and/or vibrations inside the vehicle compartment.

1.3 Outline

The thesis is structured as follows. In *Chapter 2* background information on rolling resistance and rolling noise is given. It is tried to identify the most important physical processes which need to be accounted for in the simulations.

A literature review on existing models for rolling resistance and rolling noise calculations follows in *Chapter 3*. Special attention is paid to the question whether the existing models can be used to simulate rolling losses and rolling noise in a common context. Based on the outcome of the literature review, a simulation tool is proposed.

In *Chapter 4* a more detailed explanation of the proposed simulation tool is given. The fundamental concepts behind the waveguide finite element tyre model,

the non-linear time-dependent contact model, the boundary element radiation model, and the rolling loss calculations are described. It is furthermore explained how these sub-modules interact with each other.

Chapter 5 describes the necessary procedures to derive the tyre's material properties in the waveguide finite element model from actual manufacturer design data. The process is exemplified for a 175/65 R14 car tyre. The necessary adjustments to the procedures for a 315/80 R22.5 truck tyre are discussed as well.

In *Chapter 6* some examples of the application of the simulation tool are presented. Free and forced response calculations for a car tyre are compared to measurements and FE simulations. The necessary number of lateral road surface scans is determined. The influence of tread pattern and road surface properties on the rolling resistance of a car tyre is calculated. Finally, the free response of and the sound radiation from a truck are simulated.

A summary of the work is given in *Chapter 7*. Some suggestions for future work are also presented.

The appended papers, *Paper I* to *Paper V*, provide additional, extended and/or more detailed results and analysis for the cases considered in the summary part of this thesis.

A short description of the different tyre models which are used throughout this thesis is given in *Appendix A*. Important simulation parameters for the different application examples are listed in *Appendix B*. Finally, *Appendix C* gives a quick overview of the various coordinate systems used in the different stages of the simulation process.

2 On rolling resistance and rolling noise

2.1 Fundamentals of rolling resistance

Traditionally, rolling resistance has been associated with a drag force F_R of unit Newton opposing the direction of motion. In ISO 18164:2005 [15], however, it is more generally defined as the mechanical energy converted into heat, E_{diss} , over a distance travelled, L , with a unit of J/m, i.e.

$$F_R = \frac{E_{\text{diss}}}{L} . \quad (2.1a)$$

For steady-state rolling at a speed of V , the rolling resistance can also be expressed in terms of the dissipated power P_{diss}

$$F_R = \frac{P_{\text{diss}}}{V} . \quad (2.1b)$$

As a consequence of Equations (2.1a) and (2.1b) the term *rolling loss* can be used as an equivalent expression for *rolling resistance*. Because there is a linear dependency of the rolling resistance on the axle load F_z under normal operation conditions [16], the *rolling resistance coefficient* C_r has also become a widely used measure to express rolling losses:

$$C_r = \frac{F_R}{F_z} = \frac{P_{\text{diss}}}{F_z V} . \quad (2.2)$$

There is a slight uncertainty with respect to the dependency of (2.2) on the rolling speed V as rolling losses are not in all cases linearly dependent on speed [16, 17]. In spite of this, the rolling resistance coefficient is, due to its widespread use in literature, still a relevant way of expressing the rolling resistance.

About 80% to 95% of rolling losses can be attributed to hysteresis. During rolling, the tyre material is periodically deformed. Due to the viscoelastic properties of the rubber compound, not all of the stored elastic energy can be regained in each cycle. Instead a part of the energy is dissipated. The size of this part is to some extent determined by external factors since the viscoelastic properties of

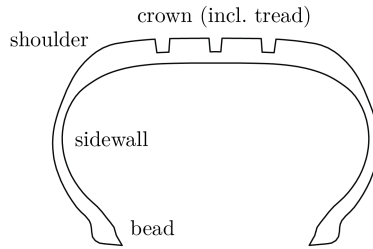


Fig. 2.1 Main regions of a tyre.

the rubber compound are highly temperature and frequency dependent [18]. The main cause of deformation for a rolling tyre is the flattening of the contact patch. This leads to bending of the crown, the sidewalls and the bead area, compression of the tread and shearing of the tread and the sidewall [16] (cf. Fig. 2.1). As a consequence, disturbances propagate inside the tyre structure in the form of waves with a variety of different mode shapes and orders, ultimately resulting in dissipation and also sound radiation.

For the nowadays nearly exclusively used radial tyres, most of the dissipation occurs in the crown and shoulder areas while passing the contact patch [16]. As these areas enter and leave the contact zone, they are subjected to large deformations. In combination with the high loss factor of the tread's rubber material this ultimately results in high hysteretic losses. Possible ways of reducing the rolling resistance include changing the tread geometry or rubber compound, or reducing the tread thickness. Such changes, however, do not only affect rolling losses, but also other important aspects like wear, traction or noise generation. The rolling resistance coefficient is linearly related to road texture depth [19, 20]. This means that rolling losses will be higher on roads with a rougher surface. Additionally, the rolling resistance shows a more or less prominent dependence on a variety of other features such as tyre load, tyre geometry, inflation pressure, driving speed, etc. A thorough description of these effects is outside the scope of the present study, detailed information can for example be found in [16, 17, 21].

2.2 Fundamentals of rolling noise

A rolling tyre is a complex dynamic system. The tyre/road interaction leads to time-varying changes of the tyre geometry which ultimately result in sound generation. Exterior rolling noise is characterised by a very typical A-weighted¹

¹In accordance with the *International System of Units* [22], the unit for A-weighted sound pressure levels is not changed to dB(A) within this work. If A-weighting is applied, it will be

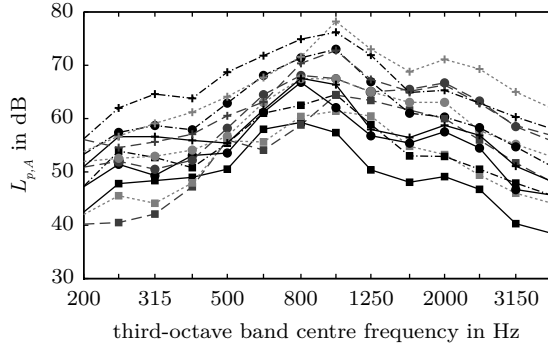


Fig. 2.2 Example of the similarity of typical car tyre third-octave band rolling noise spectra²: coast-by measurements for a 195/65 HR15 tyre at speeds of 50 km/h (■), 80 km/h (●), and 100 km/h (+) on four different road surfaces (indicated by different lines/shades of grey). Microphone position 7.5 m from the road axis at a height of 1.2 m.

third-octave band spectrum, see Figures 2.2 and 2.3 for some examples. The frequency range of interest is in the range of 100 Hz to roughly 4 kHz, with a broad but pronounced peak around 800 Hz to 1.25 kHz for cars, and 500 Hz to 1.25 kHz for trucks. This behaviour is typical for nearly all tyre/road noise spectra [12]; changes are only seen for unusual tyre/road combinations or operating conditions.

Several physical mechanisms contribute to rolling noise. It is usually distinguished between

1. vibrational mechanisms, caused by
 - a) impact, or
 - b) adhesion and friction, and
2. aerodynamical mechanisms, and
3. propagation effects, such as
 - a) the horn effect, and
 - b) pipe resonances.

Items 1a and 1b lead to vibrations of the tyre tread, belt and sidewall, which in turn are radiated as sound. The processes described by item 2 are direct sources of airborne sound. The transmission of sound generated by both of these processes is

²Within this thesis all sound pressure levels are based on the standard reference pressure of $p_0 = 2 \cdot 10^{-5}$ Pa.

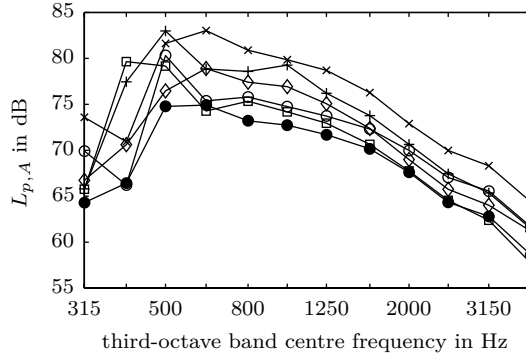


Fig. 2.3 Example of the similarity of typical truck tyre third-octave band rolling noise spectra: close-proximity measurements for two different 315/80 R22.5 tyres on two different road surfaces at speeds of 50 km/h (●/□/◆/×) and 60 km/h (○/+). Average of nine microphones equally distributed over a half-circle around the tyre at 1 m from the centre of the contact patch and a height of 0.25 m.

affected by the mechanical, geometrical and acoustical properties of the tyre and the road surface. This effect is described by item 3.

It is believed that mainly vibrational mechanisms are responsible for low frequency rolling noise up to about 1 kHz, whereas aerodynamical mechanisms dominate above [12]. Yet, the exact contribution of each individual source mechanism is still not completely clear. Certain is only that the relevance can vary considerably depending on tyre, road surface and operating conditions.

2.2.1 Vibrational mechanisms

Impact mechanisms

Impact mechanisms could be described as macro-scale mechanical phenomena leading to tyre vibrations. They can be divided into

- running deflections,
- tread impact, and
- texture impact.

Running deflections are the large scale-deformations of the tyre tread, belt and sidewall at the leading and trailing edges of the contact zone. Time-varying contact forces due to tread patterns or road texture lead to further, mostly radial, excitation of the tread and belt area. While all mechanisms mostly excite the

tyre tread and belt, there is also wave propagation to the sidewalls. Due to the high damping of the tyre material, structural vibrations are mostly limited to the proximity of the contact patch region. For most tyres the size and spacing of tread blocks is randomised to minimise the occurrence of dominating tones in the rolling noise spectra. Due to wear considerations tyres used on the driving axles of trucks often have regular tread patterns, giving rise to problematic tonal components.

Texture impact is caused by the roughness of the road surface. Several studies have shown that for most types of roads rolling noise up to roughly 1 kHz is positively correlated with the road texture amplitudes of wavelengths of about 10 mm and higher [12, 23, 24]. This means that low frequency rolling noise is road texture related.

Impact mechanisms are the dominating source below 1 kHz to 1.6 kHz. In addition, there is a strong indication that the aforementioned broad peak, which is typically visible in tyre/road noise spectra at around 800 Hz to 1.25 kHz, is at least partly related to macro-scale tyre vibrations [12]. Because of the importance of the vibrational behaviour of a tyre for rolling noise, the typical dynamic properties of a tyre are reviewed briefly here. For this the mobility Y , i.e. the complex ratio of a velocity v and a harmonic force F in a dynamic system, is introduced

$$Y(\omega) = \frac{v(\omega)}{F(\omega)}, \quad (2.3)$$

where $\omega = 2\pi f$ is the angular frequency. Y is an input mobility if v is taken at the same location as F , otherwise it is a transfer mobility.

In Fig. 2.4 measured radial input mobilities for a car and a truck tyre are shown. For both tyres, the behaviour is dominated by the rigid body modes and the first circumferential modes in the low frequency region. This region extends to approximately 200 Hz for the truck tyre and, due to the smaller dimensions, up to 300 Hz for the car tyre. In this region the tyre acts like a pre-tensioned ring on an elastic foundation. The behaviour is mostly dominated by the inflation pressure (i.e. the pre-tension), the sidewall stiffness and the mass per unit length of the tyre structure. Damping is relatively low. Due to the tyre curvature, there is strong coupling between in-plane and out-of-plane motion. Because of a higher inflation pressure and a stiffer internal construction the response of the truck tyre is lower than that of the car tyre. With increasing frequency the influence of curvature becomes weaker; after the ring frequency (where the longitudinal wavelength equals the tyre circumference) the tyre can be interpreted as a beam [25]. For typical car tyres the ring frequency is located between 200 Hz and 400 Hz. For truck tyres it is again somewhat lower. The beam behaviour is often not very pronounced because of the appearance of the first cross-sectional modes, which generally also occurs around 300 Hz to 400 Hz for car tyres and around 200 Hz for truck tyres. In this region some differences can be observed between car and truck tyres. The dynamic behaviour of car tyres is dominated by the belt-bending modes around their cut-on

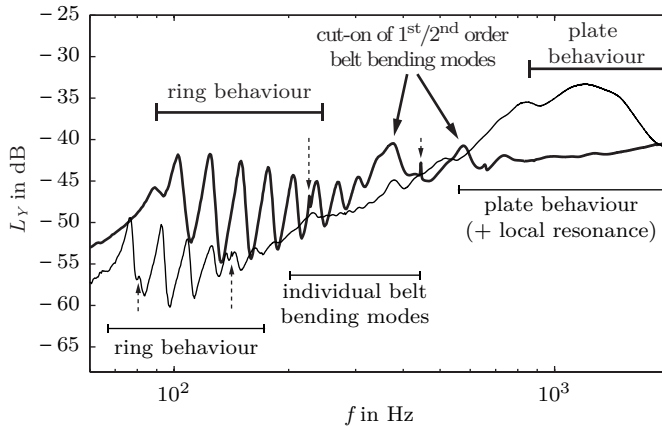


Fig. 2.4 Vibrational behaviour of car and truck tyres exemplified by measured radial input mobilities for excitation at tread centre line. Examples are a 205/55 R16 slick car tyre (thick line, labels in upper part) and a 315/80 R22.5 truck tyre with airplane profile (thin line, labels in lower part). Dashed arrows mark air cavity resonances. $L_Y = 20 \log_{10}(|Y/Y_0|)$, $Y_0 = 1 \text{ N}/(\text{ms})$.

frequencies, visible by the distinct peaks at 370 Hz and 580 Hz in Fig. 2.4. Interestingly, none of these two peaks is resulting from only one cross-sectional mode. Both are rather given by the combination of groups of modes with the same cross-sectional order (i.e. one or two) but different orders in circumferential direction. For the truck tyre, the belt-bending modes of the same cross-sectional order are instead spaced further apart and are visible as individual peaks, albeit with much less pronounced amplitudes. In this frequency region the tyre behaviour depends mainly on the bending stiffness of the belt region and only to a small extent on the pre-tension.

For frequencies above some 800 Hz the tyre dynamics can no longer be attributed to individual modes or mode groups. The tyre mobility resembles that of an infinite flat plate. For the truck tyre the plate behaviour is often not clearly visible as the local deformation of the tread layer at the excitation/response position starts to influence the mobility measurements [26]. Because of this local effect, the amplitude of the input mobility of the truck tyre is higher than that of the car tyre. The influence of the local tread stiffness has also been observed for car tyres, albeit less pronounced. The most important material property in this frequency region is the tread's Young's modulus. The distinctiveness of the local effect is additionally governed by the rubber thickness and the size of the excitation area [27]. For even higher frequencies, typically above 2 kHz for car tyres, in-plane shearing starts to play a role [28, 29].

Furthermore, Fig. 2.4 also shows two sharp peaks at 230 Hz and 450 Hz for the car tyre, and 80 Hz and 160 Hz for the truck tyre. These are caused by the first two circumferential resonances inside the air cavity. While especially the first of these resonances is known to be of importance for noise inside the vehicle cabin [30], they are only of minor relevance for exterior rolling noise [12, 31].

Adhesion and friction mechanisms

Micro-scale adhesion and friction mechanisms are responsible for phenomena like

- stick/slip, and
- stick/snap.

Stick/slip occurs due to tangential forces in the contact zone which are created by the change in tyre radius. These forces are resisted by frictional forces between the tread and the road surface. Friction is caused by hysteresis and adhesion, with the latter describing effects like molecular bonding, mechanical interlocking or pressure differences. When the frictional forces can no longer balance the tangential forces, the tread rubber is free to slip over the road surface, causing mostly tangential vibrations of the tread. Stick/snap occurs when the tyre/road contact is sticky (e.g. for winter tyres on warm days and/or very clean roads). During the separation process at the trailing edge, strong adhesive bonds between the tread rubber and road surface have to be overcome. When a certain number of micro-scale contact junctions have been broken, the remaining will break as well. This avalanche-like effect causes a very sudden acceleration of the tread and maybe also a transient air-flow through the opening slid. The influence of stick/slip motion on sound generation depends on the slip velocity and the tread geometry. In general it is a rather high-frequency phenomena which is only of secondary relevance for rolling noise under steady-state rolling conditions [16]. However, it can be a significant source of noise under acceleration, braking or cornering.

2.2.2 Aerodynamical mechanisms

All sound generation processes which are directly related to air displacement (as opposed to being caused by vibrations) are typically called aerodynamical mechanisms. These processes include

- air turbulence,
- air-pumping, and
- Helmholtz resonances.

Due to the translational and rotational motion of a rolling tyre, air is displaced and dragged around the spinning tyre and wheel. It is assumed that the resulting air turbulences are of relevance for overall noise levels for combinations of high speed, high frequencies and low-noise road surfaces [12].

A phenomenon of great importance for rolling noise is air-pumping. The physical processes behind it have not yet been fully understood. A common theory describes it as the displacement of air in and out of all sorts of cavities formed by the tread and the road surface during contact [12]. At the leading edge air is compressed and forced away from the contact while at the trailing edge air expands and is drawn back into the cavities. Further air displacements occur within the contact patch itself. Air-pumping might also be caused by the displacement of tread rubber by road roughness peaks. The volume of displaced rubber is larger than the volume of the peak, thus causing air displacement [32]. Regardless of which theory is applied, high air pressure gradients make air-pumping a significant, if not the main, noise source for frequencies above approximately 1 kHz to 2 kHz. The rate of air displacement is mainly dependent on the rolling speed; the radiated sound power is assumed to be proportional to the fourth power of vehicle velocity [25].

Helmholtz resonances may be seen as special cases of air-pumping. A Helmholtz resonator is a mass-spring system which is formed by the motion of air in a cavity. When a tread cavity moves out of contact, a mass-spring system is created in the moment the cavity opens again. The air inside the cavity acts as a spring, and the air in the just created small channel acts as a mass. The frequency and amplitude of this resonator change continuously as the cavity moves further out of contact, resulting in a tone burst. In [33] it is shown that this effect has a significant influence on sound radiation for cross-bar type tyres in the 1 kHz to 2.5 kHz range.

Some studies have found a strong negative correlation between high frequency rolling noise and road texture amplitudes of wavelengths less than 10 mm [12, 24]. These results could not be confirmed by other studies [23], meaning that the relation between road surface properties and aerodynamically generated rolling noise remains unclear.

The tyre cavity resonances which have been briefly mentioned in Section 2.2.1 constitute another example of aerodynamical sources.

2.2.3 Propagation effects

The horn effect

Close to the contact region, the geometry between tyre and road resembles that of a horn. The exponentially widening geometry when moving away from the contact patch provides a gradual and smooth impedance match between the narrow throat at the contact edge and the ambient air. This has a significant amplification effect on sound radiation because a majority of the rolling noise sources are situated at

or near the contact patch. The amplification affects the whole frequency range from roughly 300 Hz and upwards. The maximum lies between 1 kHz and 3 kHz, where amplifications of up to 25 dB in the tyre plane have been reported. At high frequencies interference becomes important and complex directivity patterns form [34, 35]. Even for complex pass-by situations, in which distance and angle to the tyre vary continuously and the car body affects the sound propagation, average amplifications of 5 dB to 12 dB per third-octave band have been reported [34]. The horn effect is strongly affected by tyre width and road surface, with smaller tyres and higher surface porosity reducing the amplification effect [34, 35].

Pipe resonances

Pipe resonances occur when standing waves are excited inside the grooves of the tyre tread by nearby vibrational or aerodynamic sound sources. This amplifies the sound created by the source. The resonance frequency depends on the length the pipe, and whether it is open at one or two of the ends. Systems of pipe resonators are formed for every tread pattern in contact with a smooth road surface. The effect on sound radiation depends largely on the individual, hard to determine geometrical properties during contact, and is not speed dependent. In an idealised test case pipe resonances have shown to increase the total A-weighted sound pressure level by 3.5 dB [36]. Pipe resonances are also sometimes classified as a source mechanism, often seeing them as a special case of air-pumping.

3 Review of existing models

3.1 Requirements for a combined rolling resistance and tyre/road noise simulation tool

The public awareness of the environmental and health benefits associated with the reduction of rolling resistance and rolling noise of car and truck tyres has grown. However, the actual physical processes responsible for both quantities are not yet fully understood. In particular there is a lack of knowledge about relevant source mechanisms and the relations between the physical processes leading to rolling resistance and rolling noise.

Besides facilitating the reduction of rolling resistance and/or rolling noise, knowledge in this field is invaluable for evaluating whether reductions can be achieved in both areas simultaneously, or whether this is a contradictory requirement. Extensive experimental data obtained by several authors [37–39] suggests that there is no incompatibility between simultaneous noise and rolling resistance improvements. However, because of the empirical nature of the results, not much insight into the physical processes has yet been obtained. More recently, Boere et al. [20] investigated the influence of different road textures on rolling noise and rolling resistance. However, with the main focus being on the impact of the tyre/road interaction, there was no examination of the physical processes in the tyre. While several authors [40–42] used models capable of capturing the tyre dynamics for rolling resistance calculations, none of them included sound radiation. In view of this, a unified rolling noise/rolling resistance simulation tool should be developed. This tool should be capable of calculating both properties based on the same tyre model and the same boundary conditions.

Ideally, this tool should be detailed enough to capture the relevant properties of tyre construction and road surface profiles, and give insight into the fundamental physical source processes behind rolling resistance and rolling noise. At the same time the tool should be numerically efficient to facilitate its use for the design process of tyres or road surfaces.

In the next two sections, existing tyre/road noise and rolling resistance models are evaluated regarding their suitability for combined simulations of both quantities in a common context. The model proposed in the present study is then described in Section 3.4.

3.2 Review of tyre/road noise models

3.2.1 General overview

Methods for tyre/road noise simulations can generally be divided into three main categories:

1. Statistical models,
2. physical models, and
3. hybrid models.

The statistical models try to establish relations between different sets of empirical data, for example measured road surface profiles and measured sound pressure levels [43, 44]. The mechanical processes in the tyre are of no interest; they are neither simulated nor are any efforts made to understand them. Consequently, statistical models are not a suitable choice within the scope of this thesis.

Physical models, in contrast, try to simulate the actual physical processes responsible for tyre vibration and sound radiation using basic physical laws. The models often either follow an analytical approach in which the tyre is replaced by a simplified structure (like a ring or plate), or they are based on numerical tools like finite element modelling (FEM) or boundary element modelling (BEM). Measured data is only used as input data or for validation purposes.

Hybrid models combine features of statistical and physical models. A typical example would be a statistical model which no longer directly relies on measured road surface profiles because of the non-linearity of the tyre/road interaction. Instead, contact forces calculated by a physical contact model are used as input into the statistical part. This approach is for example used by the SPERoN model [45]. Hybrid models share most of the limitations of statistical models with regards to the obtained physical insight. Because of the limitations of statistical and hybrid models, the focus will be purely on physical models in the following¹.

Tyre/road noise modelling is typically seen as three-part process as shown in Fig. 3.1. The core is a model of the tyre dynamics which allows for free or forced response calculations. To simulate the excitation of the tyre by the road surface, a tyre/road contact module is needed. Because of the interdependency of contact forces and tyre vibrations — the forces cause vibrations, yet at the same time the vibrations influence the forces — there is usually a two-way coupling between the tyre/road contact module and the tyre dynamics module. While these two modules are sufficient to estimate for example hub forces or rolling resistance, an additional module is needed to calculate the actual sound radiation, i.e. the tyre/road noise caused by the tyre vibrations. Variations or extensions of this

¹The interested reader can find more information about statistical and hybrid models in [11, 46]

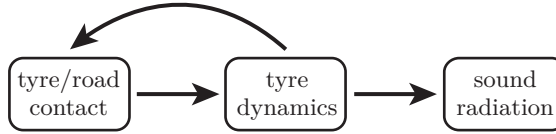


Fig. 3.1 The three parts of tyre/road noise modelling.

three-stage process are obviously conceivable, e.g. to include air pumping or for interior noise calculations.

As the complexity of each of the three mentioned sub-modules is rather high, very few models exist which are able to calculate tyre/road noise. Many models only focus on the tyre dynamics (with or without road contact), and omit sound radiation. For many applications this is sufficient, and if needed, most of these models could be extended by a radiation module. Accordingly, the following review will start with a general selection of tyre models found in the open scientific literature. Contact and radiation models are then described in the subsequent sections.

3.2.2 Tyre models

Since the mid-1960s, a variety of different models for simulating the dynamic response of tyres have been developed. These range from analytical models, based on more or less coarse simplifications of the geometrical and material properties, to highly sophisticated numerical models accounting for the detailed physical properties of tyres.

One of the first models was presented by Böhm [47]. He calculated low frequency free and forced responses of a tyre by modelling it as a pre-tensioned, circular ring (the belt) on an elastic foundation (the sidewall). Through the years, many variations of the same basic approach have been used to model various aspects of tyre dynamics, e.g. by Heckl [25], Kung et al. [48], Kropp [49], or more recently Kindt et al. [50] or Tsotras [51]. The models perform quite well for frequencies below roughly 300 Hz or 400 Hz but generally fail for higher frequencies at which wave propagation across the tyre cross-section starts. This is because the approach does not allow for lateral wave propagation.

Kropp [49] proposed a method to overcome this shortcoming by modelling the complete assembly of belt and sidewalls as a pre-tensioned, orthotropic plate on an elastic foundation. Agreement between modelled and measured input mobilities was good for frequencies up to 2 kHz, with the exception of the lower frequency regions below the ring frequency which were negatively affected by the negligence of curvature. By combining the orthotropic plate model with a two-dimensional multipole based radiation model and a non-linear contact model in which the tread

was modelled by massless uncoupled springs, tyre/road noise could be calculated as well. Agreement with measurements was good below 1.5 kHz. In [52, Paper C] the same tyre model was combined with a BEM radiation approach to investigate differences between full 3D and quasi-3D contact models. Later variations of the orthotropic plate model included incorporating curvature to increase low-frequency performance [53], modelling the sidewalls as separate orthotropic plates being perpendicularly attached to the belt plate [54], or using a two-layer setup of isotropic plates in order to investigate the influence of the tread layer on wave propagation and forced responses in normal and tangential direction [29]. O'Boy and Dowling [55] modelled tyre/road noise for a patterned tyre rolling over a rough road using a bending plate model in conjunction with a contact model similar to Kropp's and a modified Rayleigh integral approach for radiation.

Another variant of the plate approach was proposed by Pinnington [28, 56]. He modelled the tyre as a combination of a flattened, tensioned Timoshenko beam for the belt and line impedances for the sidewalls, however with mixed results. He later extended the model by implementing belt and sidewalls as coupled, curved and tensioned Mindlin plates [57, 58]. With the exception of the cut-on frequencies of the higher-order cross-belt modes good agreement between modelled and measured mobilities was achieved for frequencies below roughly 3 kHz. An additional model which explicitly includes the sidewalls is the one by Lecomte et al. [59]. They combined an orthotropic cylindrical shell for the belt with membrane sidewalls in order to simulate the tyre behaviour in the low frequency region up to 500 Hz.

The presented analytical models are usually comparably simple and fast, and often provide worthwhile insight into physical processes. However, problems arise due to the geometrical simplifications inherent to all of the models. This includes problems with capturing the dynamic behaviour adequately over the whole frequency range of interest for tyre/road noise, the lack of the possibility to determine localised effects, and the need for usually rather involved procedures to determine the needed simplified material properties. The ring models are also not very well suited for proper contact modelling because lateral effects cannot be included.

The rapid development of computer capacity during recent decades has made it possible to perform detailed numerical simulations of tyres using FEM. While early FE models [48, 60, 61] were geometrically only slightly more complex than their analytical counterparts, current implementations are detailed enough to individually model nearly every different material group in the tyre [62, 63]. FE based tyre dynamics models have been the basis for a number of different applications. Kung et al. [48] determined natural frequencies and mode shapes and then used these to calculate the dynamic response at the wheel axle. Richards [62] presented an FE method which allowed for structural-acoustic coupling between the tyre structure and the air cavity. This method was used to determine the influence of the air cavity resonances on tyre vibrations and force transmissibility through the hub. Force transmissibility, along with point mobility, was also simulated using FEM

by Pietrzyk [64]. The response of tyres rolling on a smooth surface was modelled by Fadavi et al. [65] and Lopez et al. [66], who also included rotational effects. The latter model was subsequently also used for rolling resistance predictions [20, 67].

A very extensive FEM approach for rolling car and truck tyres was developed by Brinkmeier et al. [63, 68]. The model is geometrically very detailed, usable for frequencies well above 1 kHz and includes material non-linearity, rotational effects, and excitation by the road surface. For tyre/road noise calculations the structural model was used as input to a finite/infinite element model [68, 69]. Alas, sound radiation was considerably overestimated for rolling tyres at frequencies above 150 Hz to 200 Hz [69], probably due to shortcomings of the contact model, see Section 3.2.3. A similar study was performed by Schutte [70] using ABAQUS.

Generally, FE models have proven to be valuable tools. They are flexible and can easily account for non-linearities, complex materials and geometries. Using FE, objects and processes which are far too complicated to be covered by analytical models can be easily simulated. The use of commercial FEM software can reduce implementation time and the widespread use in industry facilitates data exchange. However, there are still two major problems associated with FEM. Firstly, finite element calculations often provide less insight into the physical processes leading to a result than a comparable analytic model (assuming that this exists). Secondly, requirements on computer capacity are high. The available computation power limits the discretisation size which in turn determines the upper frequency limit of the simulations. Due to this, simulations are usually restricted to frequencies below approximately 500 Hz. In the model of Brinkmeier et al. the frequency range was extended to above 1.5 kHz, but this required a mesh consisting of over 60 000 elements [63]. Even with today's computational resources it seems hardly practical to use FEM for parameter studies covering the whole relevant frequency region for tyre/road noise, i.e. up to around 2 kHz. The practical limits on mesh size also affect contact modelling. To accurately capture three-dimensional road surface and tyre profile variations a high resolution is necessary.

In order to reduce computational costs several approaches which combine parts of traditional FE modelling with analytical methods have been presented in recent years. Finnveden and co-workers developed a model called waveguide finite element method (WFEM) [42, 71, 72]. In this technique the tyre is considered to have constant cross-sectional material and geometrical properties along the circumference. This allows to combine FE modelling of the cross-section with a wave propagation ansatz in the circumferential direction. The resulting eigenvalue problem is formulated in the wave domain and requires specially developed elements. Computational costs remain low because only the cross-section of the tyre is modelled numerically. This considerably extends the usable frequency range; transfer functions were calculated up to 1.6 kHz [71]. The method was first used for tyre modelling by Nilsson [71], who considered the structural and fluid domains, using waveguide finite elements of the thin shell type, fluid type and fluid-structure

coupling type. Calculated transfer functions showed mostly good agreement with measurements up to 1.6 kHz. Thick curved shell and solid waveguide finite elements were developed in [72] and used to model the free and forced response as well as the rolling resistance of a car tyre in [42], low frequency interior and exterior tyre/road noise [73], dispersion and wave phenomena [74], hub forces [75], and tyre/road noise [76].

Waki et al. [77] presented a similar approach in which the tyre is considered as a periodic structure along the circumference. Initially, a short section of the waveguide is modelled using standard commercial FEM. A periodicity condition is then applied. This results in an eigenvalue problem from which the forced response can be calculated using a wave approach. Numerical efficiency is again high and in contrast to the WFEM approach there is no need for specially designed elements. Simulations of input mobility showed good agreement with measurements up to 2 kHz. Alas, no results were shown for other quantities such as transfer mobilities. The method also seems to be prone to numerical problems [78]. A variation of this approach which directly solves for the forced response has been presented by Duhamel et al. [79].

Nearly all of the mentioned models have exclusively been applied to car tyres. After a phase of intensive research on truck tyre vibrations and sound radiation in the United States in the 1970s and early 1980s, e.g. [80–83], research on truck tyre acoustics has been rather limited, especially with respect to mid- and high-frequency simulations. Chae et al. [84] used FE and ring models to predict the low frequency truck tyre response as input parameter for vehicle dynamics simulations. Zhang et al. [85] conducted a modal analysis of a truck tyre using FEM. The analysis was mostly concerned with the influence of tyre construction and material parameters, and the frequency range was limited to approximately 150 Hz. As a part of rolling resistance computations, mobilities for frequencies up to 200 Hz were calculated using a ring model in [86]. More emphasis on acoustically relevant frequency regions was laid in [87], where an orthotropic plate model was used to simulate truck tyre responses up to 4 kHz. Due to the simplicity of the model, results for transfer mobilities were not satisfying. Using their advanced FE model, Brinkmeier et al. [68] calculated the free response of a rotating, and the forced response of a rolling truck tyre below 1 kHz. Alas, only very few eigenforms were shown, their relevance for sound radiation was not discussed, and results were not compared against measurements.

3.2.3 Contact models

In the following section only models implemented for rolling contact will be described; this leaves aside a variety of tyre/road interaction models focusing on the calculation of texture induced pressure distributions [88] or tread viscoelasticity and inertia [89–91].

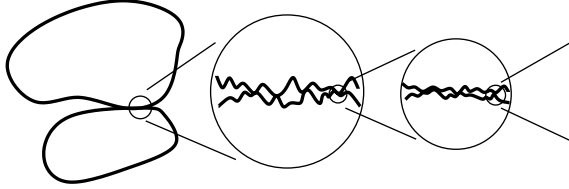


Fig. 3.2 The difference between the *apparent* and *real* area of contact. Due to small-scale surface roughness only discrete parts of the bodies are in contact.



Fig. 3.3 The change in contact area during the loading phase. At time t_1 only the asperity peaks are in contact. At time $t_2 > t_1$ the bodies are closer and the area in contact increases. This causes the contact stiffness to increase as well.

Modelling the interaction between a rolling tyre and the road is a complex task. One of the main challenges is the extent of relevant length scales, ranging from several meters (road unevenness) down to microscopic (road asperities) or even molecular levels (adhesion effects). The size of a typical contact patch is too big to allow a full discretisation down to the smallest relevant length scales. As a consequence, the distinction between the *apparent* and the *real area of contact* between tyre and road becomes important. At small scales, both road and tyre have a certain roughness; contact will only be made between certain parts of the asperities, see Fig. 3.2. Hence, the area which is in contact is only a fraction the size of what it appears to be at a macro-scale level. Additionally, as shown in Fig. 3.3, the contact area changes during loading and unloading. For example, at an early stage of contact only the highest peaks of the asperities are in contact, giving a very small area of contact. At a later stage, larger parts of the asperities are in contact. Thus, the real area of contact — and with it the contact stiffness — changes during the time of the contact.

On a larger length scale another aspect has to be taken into consideration: the tyre is an elastic continuum where the deformation due to a point force at location A will not be limited to just that point. A certain area of the material will be affected, perhaps considerably changing the conditions at another contact point B. Due to inertia, this effect does not happen instantaneously, meaning that past contact forces and deformations influence the contact conditions at the current time. This dynamic interaction can put some constraints on the achievable

resolution for the contact area. Tyre models require a much lower spatial resolution to simulate the dynamic behaviour than what is needed to accurately capture the complex contact processes. Because of the computational costs and the fact that the finer resolution would only be needed in a very small part of the tyre, increasing resolution is typically not an option. Many simpler tyre models do also not explicitly include the tread, in these cases a separate contact law is required to describe the local interaction between road asperities and tread rubber.

Depending on the contact conditions, effects such as friction, adhesion and the tread rubber's viscoelasticity can also become important. Additionally, the frequency, temperature, and strain dependency of the tread's material properties might affect the contact behaviour as well.

The dynamic part of many models for rolling tyre/road contact is based on an approach which was originally used to model bow/string interaction [92]. It is a time-domain formulation in which the dynamics of the contacting bodies are described by their Green's functions. These are convolved with the contact forces to give the response at a specific time due to present and past contact forces. As the contact problem is iteratively solved for each time step, non-linear effects such as the change in contact area during contact can be included. The approach requires the bodies to be linear time-invariant systems (LTI), which puts some constraints on the tyre model. Kropp [93, 94] was the first to apply this technique to tyre/road interaction. His model was two-dimensional (i.e. based on one roughness profile line) and considered normal forces only. The tread was represented by a Winkler bedding, i.e. a set of uncoupled, massless springs with constant stiffness. Larsson et al. [95] presented a three-dimensional version of this model. The coupling of the tread displacement, which is neglected by the Winkler bedding, was accounted for by a tyre model which included a tread layer. The contact law could then be obtained from the first value of the tyre's Green's function. Wullens [52] modelled the tread as an elastic half-space. He also showed that two-dimensional roughness data is not sufficient for accurate calculation of rolling noise spectra, instead lateral variations of tyre and road geometry have to be considered [96]. All these models neglect the microscopic change in contact area during contact. Additionally, the determination of correct stiffnesses for the Winkler bedding or the elastic-half-space is not straightforward. To account for the change in contact area, non-linear contact springs between each matching point of tyre and road were introduced by Andersson and Kropp [97]; they also described a method for obtaining stiffness functions from measured road roughness data. Sabiniarz [75] included tangential forces in the model, but used only linear contact springs. Further implementations of the convolution approach were also presented by O'Boy and Dowling [55], Hamet and Klein [98], Graf [99], and Liu et al. [100].

FEM approaches have been widely used to simulate tyre/road interaction as well. Fadavi et al. [65] calculated the forced response of rolling tyre in contact with a flat rigid ground. Lopez Arteaga [101] did the same to obtain Green's

functions for a loaded, rolling tyre. Brinkmeier et al. [68] used harmonic excitation functions based on measured road surface data for the contact formulation in their FEM simulations of a rolling tyre. Sound radiation could be correctly calculated for shaker excitation of the tyre, however not for real tyre/road contact [69]. To overcome some of the spatial resolution limitations in FE modelling, Lopez Arteaga and coworkers [67, 102] proposed a method in which the tyre/road interaction is split into two parts: the large scale tyre deformations are obtained from an FE model of a tyre rolling on a smooth road, while the tread/road surface interaction is calculated separately using an extended convolution technique in which additional spring/damper sets are added to each contact point to model tread blocks. The technique seems to work quite well for the determination of rolling losses, it is however not clear if the individual calculation and subsequent superposition of large- and small-scale contact effects adequately captures the complex contact dynamics.

A similar distinction between steady-state contact deformation and dynamic road roughness induced displacements has been made by Pinnington [103] who calculated tyre/road contact using a particle-envelope model. In this model the surface profile is divided into different levels of length scales with individual contact stiffnesses. Contact pressure and indentation are calculated based on the combined effect of the different levels. Pressure-displacement relations for a tyre pressed onto a rough surface could qualitatively be described. However, the application of the approach to rolling contact was only coarsely outlined without showing results.

Finally, the modelling of tyre/road interaction under rolling conditions is not limited to sound and vibration applications. Numerous studies deal with tyre/road contact modelling as means for investigating rolling resistance, traction, contact forces under transient conditions, or vehicle dynamics simulations [51, 86, 104, 105]. However, small-scale roughness phenomena and/or tyre dynamics are often neglected in the employed Winkler-bedding type based contact models. While these simplifications are justifiable within the scope of the respective applications, the models cannot be used to accurately model tyre vibrations and rolling noise.

3.2.4 Radiation models

The number of radiation models for tyre/road noise which are described in open literature is quite small. This does not come as a surprise, as the calculation of sound radiation is the last step in a tyre/road noise simulation; reliable contact and tyre models have to be established before radiation can be calculated.

One of the earliest examples of radiation calculations for vibrating tyres is the model of Keltie [83]. He modelled a truck tyre as an infinite circular cylindrical shell with a prescribed velocity field, for which sound radiation could be calculated analytically. Because of the infinite width of the shell and the omission of the road influence, propagation effects as described in Section 2.2.3 could not be modelled.

A model which accounts for these two effects was presented by Kropp [94]. He modelled the combined contribution from the tyre and the reflection at the road surface using a two-dimensional equivalent source approach: the sound field was reconstructed using two multipoles, one for the tyre and a mirrored one for the reflections from the rigid road surface. A correction factor was derived to account for the influence of the finite tyre width. The model was used to calculate the sound radiation of a slick tyre rolling on a drum [93], and the horn effect and the radiation efficiency of different tyre modes [34]. The equivalent sources approach was extended by Bécot [106] to account for ground impedance effects.

Using a Rayleigh integral approach, three-dimensional rolling noise radiation was calculated by Graf [99], and O'Boy and Dowling [55]. The horn effect was included by means of a source specific amplification function which was obtained from separate BEM simulations.

In order to avoid the limitations analytical methods have with the modelling of the complex tyre/road geometry, numerical methods such as BEM have also been used to solve the tyre radiation problem. Ni et al. [107] modelled the noise radiation from the tyre/wheel assembly. Because of numerical constraints they did not include the road in the model and were limited to frequencies up to 350 Hz (which was sufficient for their investigations of interior noise). Due to the necessary discretisation size and the fully populated system matrices, BEM simulations are computationally costly. To reduce the numerical effort, attempts have been made to simulate the ground reflections without the need for discretising it. Brick [108] was the first to use a half-space BEM approach for tyres. This is an efficient BEM implementation which includes the ground reflections in the propagation Green's functions. In Brick's implementation arbitrary ground impedances could also be modelled. The model was used to investigate the horn effect [108], and the contribution of the individual tyre modes to the overall sound radiation of a rolling tyre [76]. Recently, Graham [109] combined the mirror source approach with BEM to investigate the horn effect.

FEM is another numerical alternative for radiation calculations. In FEM the whole domain needs to be discretised which means that discretisation costs are typically higher than for BEM, where only the surfaces of sources or other objects interacting with the wave field have to be discretised. This is at least partially offset by the fact that the FEM system matrices are banded, which makes the numerical solving much more efficient. An FE approach was used by Biermann et al. [69] to calculate the sound radiation from a tyre rolling on a drum. As traditional FEM formulations cannot model domain boundaries with free field radiation conditions, special infinite elements were developed by Biermann et al. Alas, numerical costs were never compared to those of traditional BEM simulations, so it remains unclear which of the two methods has lower computational costs. The same method was used to calculate rolling noise for a truck tyre rolling on two different surfaces in [68], however, results were not compared to measurements.

For sufficiently large problems, the efficiency of BEM can be improved using the fast multipole method in which a tree-like sub-structuring allows parts of the radiation problem to be solved locally [110]. Frequency- and time-domain formulations of fast multipole boundary element methods for tyre/road noise simulations are currently under development [111, 112].

For more specific radiation problems further techniques have been proposed. In order to model air-pumping effects, Wullens [52] used his elastic half-space tyre/road interaction model to calculate the air volume variation in the contact asperities. The volume flow was then assigned to monopoles situated at the leading and trailing edges of the contact patch. The validity of the approach remains unclear as no detailed results were presented. In a very simplified model for interior cabin noise calculations, Rustighi et al. [73] used radiation impedance matrices obtained from BEM to model tyre radiation. Finally, Kuo et al. [113] investigated asymptotic methods for simulating the horn effect. For low frequencies below 300 Hz a compact body scattering model was proposed. Above 3000 Hz good results were achieved using ray theory.

3.3 Review of rolling resistance models

Numerous examples of calculations of rolling resistance are available in the literature (see [5] for an overview). Besides some approaches partly based on measured data [114, 115], most of them follow the same conceptual approach of using a steady-state rolling tyre model to calculate rolling resistance either as a drag force or based on energy dissipation.

Stutts and Soedel [116] used a stationary tension band on an elastic foundation to model the tyre and calculated the rolling resistance from the deflection in the contact zone. In [104] a model of an elastic ring supported by a viscoelastic foundation is used to calculate the hysteretic energy dissipation. Miège and Popov [86] compared several analytical methods for computing rolling resistance, including a flexible ring model. All of the mentioned models are quite similar to the acoustical shell and ring models which have been discussed in Section 3.2.2. They either already allow for the calculation of tyre vibrations (cf. [86] where frequency response functions up to 200 Hz are calculated) or could be extended to do so. Geometrically, however, the used tyre models are over-simplified, limiting the usable frequency range and preventing the calculation of the dissipation distribution over the tyre cross-section.

Bschorr and Wolf [40] seem to be the first to have used a model of the tyre's structural dynamics to draw conclusions about the rolling resistance. However, their rolling resistance estimation was not very detailed as it was merely a by-product of their study on tyre vibrations.

Another commonly used approach is based on finite element modelling of the

tyre, often combining mechanical and thermal models. Typically, an elastic model of the tyre is used to calculate the strain cycles for free rolling. An viscoelastic simulation then gives the heat generation rate as input for a thermal simulation. This process is repeated until the thermal state has converged. Rolling resistance is then calculated in terms of the hysteresis per cycle. Thermal FE models allow identification of the relative contributions of different tyre parts to the overall rolling loss. Models following this approach have been proposed by several authors, e.g. [17, 117–119]. In a more recent work this approach was used by Cho et al. [120] to investigate the influence of different tread patterns on rolling resistance. A slightly different technique was used by Ghosh et al. [121], who calculated the dissipated energy directly out of the strain energy density distribution in a steady-state rolling FE model. An expression involving the ratio of dissipated energy to input energy over one cycle was then used to calculate the rolling resistance. Another method which directly computes the energy loss during for a mechanical FEM was introduced as the *directional incremental hysteretic model* in [122]. Again, rolling resistance was determined as hysteretic loss per cycle. Recently, Ali et al. [123] calculated the rolling resistance of a heavy truck tyre rolling on different non-smooth surfaces from reaction forces obtained by FE simulations. As the road surface profiles were artificially created no comparison to measurements could be made.

The advantage of methods based on FEM is that it is usually possible to use commercial software, thus reducing the implementation effort. The models are also rather geometrically detailed, allowing the extraction of information on the distribution of dissipation inside the tyre. It is furthermore conceivable that most of the mentioned FE models, with the exception of the *directional incremental hysteretic model* [122], could be extended to allow calculations of tyre vibrations. However, resolution requirements on the FE mesh would most probably be too high to allow for models of acceptable numerical complexity.

A general problem with all mentioned methods is the contact implementation. The used tyre/road interaction models are nearly exclusively limited to the large scale deformations caused by static loading of a tyre rolling under steady-state conditions on a smooth road. Even in the few cases where non-smooth surfaces are considered the contact resolution is very coarse: in [123], for example, contact is calculated based on a tyre circumference divided into 60 segments. For the considered heavy truck tyre this corresponds to a contact patch size of 6 cm or more. Accordingly, the small scale variations of road roughness and the complex interrelation between tyre deformation and contact forces which are both essential for the correct modelling of tyre vibrations are typically ignored in FE simulations.

To overcome this limitation, Lopez Arteaga and coworkers have used their two-stage contact model, cf. Section 3.2.3, to calculate the input power into the tyre due to the large-scale steady-state deformation and the dynamic local tread/road interaction. Comparison of results to measurements showed that, while rolling res-

istance was generally overestimated, correct tendencies for different road surfaces were obtained. A limitation of the implementation is that only 2D road roughness data, i.e. without lateral variation, is considered, and that there is no interaction between the tread/road and large-scale-deformation stages. Insight into the physical processes in the tyre is limited as well.

A substantial contribution was made by Fraggstedt [42]. He used a waveguide finite element model to calculate the vibrations and rolling losses of a rolling tyre. Frequency and wave order distributions were shown together with individual element contributions to the overall dissipation. However, the deviations between simulated and measured rolling resistances were slightly higher than for some of the other mentioned methods. Furthermore, only a few different road surfaces were considered and a detailed analysis of the results was missing. As radiation was not included in the model, rolling noise could not be calculated.

3.4 The proposed simulation tool for rolling resistance and tyre/road noise

The review of existing rolling loss and rolling noise models in Sections 3.2 and 3.3 has shown that it is easier to enhance a tyre/road noise model to allow for calculations of rolling losses than vice-versa. Contact and tyre dynamics implementations used for modelling the rolling resistance are too simplified to be used for tyre/road noise calculations. In contrast, models capable of capturing the dynamics of a tyre rolling on a real road have successfully been extended to give reasonable estimates of rolling losses [40, 42, 102]. In view of this, an existing, validated tyre/road noise simulation tool [76] is enhanced with a module for rolling loss calculations. Additional extensions are made to account for the specialities of modelling a truck tyre, and to efficiently include the influence of a tread pattern into the tyre dynamics and contact modules.

Core of the simulation package is a WFE model of the tyre [74]. Previous studies using this model have been based on 205/55 R16 and 175/65 R14 car tyres. Tyre properties are based on detailed tyre design data provided by the manufacturer. For the estimation of the equivalent material properties needed for the model, a thorough physical condensation procedure which captures the complete anisotropic behaviour of the tyre structure is proposed. Both car tyre models are primarily based on shell elements and rely only on isotropic solid elements for the tread layer. Due to the larger dimensions this approach is not feasible anymore for a truck tyre. Accordingly anisotropic solid elements are introduced and used for modelling a 315/80 R22.5 truck tyre.

Tyre/road interaction is modelled using non-linear, convolution based algorithm. As the tread is already included in the WFE tyre model, there is no need for separ-

ate substitute structures like a Winkler-bedding or an elastic half-space. Contact springs are used to account for the small-scale contact stiffness. In contrast to the model described in [97], only linear contact springs are used because the available road roughness data is not sufficient to determine non-linear stiffnesses. Originally also included tangential contact forces (cf. [74]) have been omitted because of their minor relevance for both rolling resistance and rolling noise under steady-state rolling conditions [12, 104]. For the modelling of rolling losses due to small-scale tyre/road interaction non-linear damping is introduced into the contact model. Locally varying spring stiffnesses and damping coefficients are used to model the influence of arbitrary tread patterns.

Sound radiation is calculated using the half-space boundary element method proposed by Brick [108]. Contrary to simpler analytical approaches, this model can adequately handle the complex three-dimensional geometry formed by the tyre and the road. It has been validated for both the horn effect [108], and the sound radiation of a tyre rolling on a drum [76]. The half-space approach considerably reduces the calculation effort. Although only rigid road surfaces are considered in the present study, it allows ground impedance effects to be modelled in future studies.

Finally, rolling losses are calculated based on two different formulations proposed in [42]. Based on contact forces and displacements, the input power into the tyre can be calculated. For steady-state rolling this is equal to the dissipated power. Tyre road/noise is traditionally analysed as frequency spectra. Moreover, the contributions of individual modes to the radiation can be analysed. Based on the waveguide properties of the tyre model, the same is now possible for the rolling losses. Frequency and/or circumferential wave order contributions can easily be identified. This way, rolling resistance and rolling noise can be analysed in the same context, which helps to identify both common and distinctive features. In the second formulation, rolling resistance is calculated by means of the internal dissipation inside the tyre. As the tyre cross-section is represented by individual elements in the WFE approach, it is possible to identify the cross-sectional distribution of losses by calculating the dissipation inside the individual elements. The ability to simultaneously extract detailed information about frequency, wave order and cross-sectional distribution of rolling losses is unique to the WFE approach; with analytical or FE models concessions have to be made in at least one of these fields. The influence of road surface roughness on the rolling resistance can be calculated from the non-linear small-scale damping terms in the contact model.

A more detailed description of the combined simulation tool for rolling resistance and tyre/road noise follows in Chapter 4. The necessary procedures for deriving a WFE tyre model from tyre design data are presented in Chapter 5.

4 The tyre/road noise and rolling resistance model

In this chapter a condensed description of the simulation tool for rolling resistance and tyre/road noise which was proposed in Section 3.4 is given. An overview of the simulation workflow is shown in Fig. 4.1. Each of the three main modules (tyre model, tyre/road interaction, radiation) is of high complexity. Within the scope of this work it is not possible to describe each of the three in every detail. Instead, the aim is to convey those principles fundamental for the understanding of the simulation process as a whole. Literature sources with more detailed information will be referenced when necessary.

Because the model of the tyre dynamics is the core part of the simulation tool, it will be described first in Section 4.1. This is followed by the tyre/road interaction model in Section 4.2, some thoughts on the influence of tread patterns in Section 4.3, and the radiation model in Section 4.4. The two ways to calculate rolling losses are described in Section 4.5. The chapter concludes with Section 4.6, where some additional remarks on the simulation process are made.

4.1 The waveguide finite element tyre model

4.1.1 Basic WFE formulation

The used waveguide finite element approach is identical to the one described in [74, 76]. It is a modified version of the model presented in [42, Paper B], the main differences being the omission of the rim from the assembly and changes in the damping implementation. In the following an overview of WFEM is provided.

A waveguide is a system with constant geometrical and material properties along one (typically “long”) dimension. In this dimension, the motion can be described by a set of propagating waves fulfilling the boundary conditions imposed by the waveguide characteristics. In this sense, and with reference to Fig. 4.2, a tyre is a waveguide for which the motion along the circumferential dimension can be described by waves fulfilling a periodicity condition $\mathbf{u}(\theta) = \mathbf{u}(\theta \pm 2\pi)$, where \mathbf{u} is the tyre displacement and θ the circumferential angle. Typical other waveguide examples include beams and plates [124], or rails [125, 126].

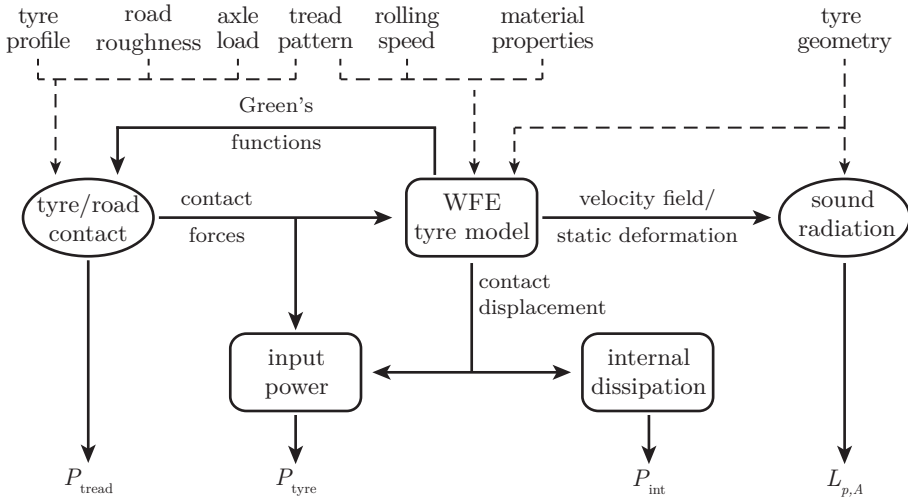


Fig. 4.1 Flowchart of the rolling noise and rolling loss simulations. Dashed lines denote input parameters and solid lines denote calculated properties. Modules in rectangular boxes are using a Lagrangian reference frame and modules in elliptic boxes an Eulerian reference frame (cf. Appendix C.1). Output parameters are the input power P_{tyre} , the internally dissipated power P_{int} , losses due to small-scale tread deformations P_{tread} , and the A-weighted sound pressure level $L_{p,A}$.

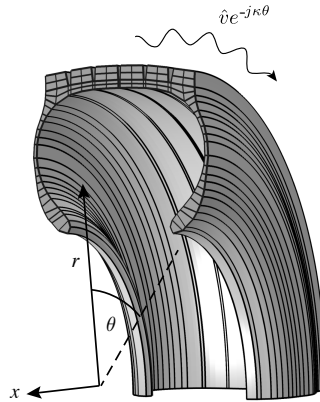


Fig. 4.2 The tyre as a curved waveguide: for the cross-section lying in the (x, r) -plane an FE approximation is used, while in circumferential direction θ wave propagation is assumed. Waves travelling in negative θ direction have to be considered as well, but are not shown here.

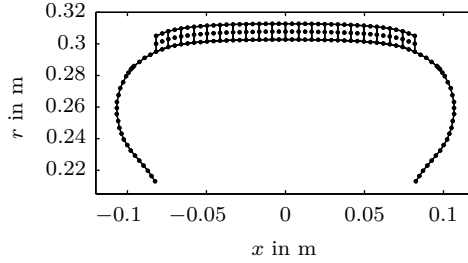


Fig. 4.3 WFEM mesh of a slick 205/55 R16 tyre with 46 shell and 20 solid elements. Each \bullet represents one node.

In WFEM, the waveguide property is used in conjunction with conventional two-dimensional finite element modelling of the waveguide cross-section, see Fig. 4.3. For a cylindrical coordinate system the components of the displacement vector $\mathbf{u} = [u_r \ u_x \ u_\theta]^T$ at a point (r, x, θ) are accordingly given by

$$u_i(r, x, \theta, t) = \mathbf{N}(r, x) \mathbf{v}_i(\theta, t), \quad i = r, x, \theta. \quad (4.1)$$

Herein, $(\bullet)^T$ denotes the matrix/vector transpose, \mathbf{N} is a vector of cross-sectional FE shape functions, and \mathbf{v}_i represents the corresponding nodal degrees of freedom vector. Thus, only the displacements' dependence on the cross-sectional coordinates is approximated using FE modelling. The nodal displacements are functions of the angular coordinate θ and depend on the assumed wave propagation along this dimension.

The derivation of the waveguide finite element formulation of the tyre dynamics starts with Hamilton's principle. This states that of all possible paths along which a dynamic system can move from one point to another in time and space, the one chosen is always the one that minimises the time integral of the difference between the kinetic and potential energies. Mathematically it can be expressed as [127]

$$\delta \int_{t_1}^{t_2} (U - K + A) dt = 0, \quad (4.2)$$

where $t_1 < t_2$ are two arbitrary times and the term

$$L \equiv U - K + A \quad (4.3)$$

is called the *Lagrangian function*. U and K are the strain and kinetic energies of the system, and A is the potential energy of loading.

By assuming viscoelastic material properties, harmonic motion of type $e^{j\omega t}$ (where $j = \sqrt{-1}$), and the absence of volume forces and external traction, U , K and A can be expressed as (see [72] for detailed derivations)

$$U = \int_V \varepsilon^{aT} \mathbf{D} \varepsilon dV, \quad (4.4a)$$

$$K = \int_V \rho \omega^2 \mathbf{u}^{aT} \mathbf{u} dV, \quad \text{and} \quad (4.4b)$$

$$A = - \int_V (\mathbf{f}^H \mathbf{u} + \mathbf{f}^T \tilde{u}^a) dV. \quad (4.4c)$$

ε is the engineering strain vector, \mathbf{D} the complex rigidity matrix, ρ the density, and \mathbf{f} the vector of external surface forces. $(\bullet)^H = (\bullet)^{T*}$, where $(\bullet)^*$ is the complex conjugate. Finally, $(\bullet)^a$ indicates the complex conjugate in a mathematically adjoint system with negative damping. The latter is a conceptual trick necessary to allow the formulation of a variational principle for viscoelastic materials. For details the reader is referred to [72].

In (4.4b) and (4.4c) u is replaced by the waveguide finite element displacement formulation (4.1), and in (4.4a) ε is written in bi-linear form as

$$\varepsilon(r, x, \theta) = \mathbf{E}_0(r, x) \mathbf{v}(\theta) + \mathbf{E}_1(r, x) \frac{\partial \mathbf{v}(\theta)}{\partial \theta}, \quad (4.5)$$

where \mathbf{v} is the vector of all nodal displacements, and \mathbf{E}_0 and \mathbf{E}_1 are matrices depending on the element-specific strain-displacements relations and shape functions and their derivatives. The resulting expressions for U , K and A are inserted into the Lagrangian (4.3). Application of standard procedures for finite element formulation and system assembly gives

$$L = \int_{-\pi}^{\pi} \left(\sum_{k=0}^1 \sum_{l=0}^1 \frac{\partial^k \mathbf{v}^{aT}}{\partial \theta^k} \mathbf{A}_{kl} \frac{\partial^l \mathbf{v}}{\partial \theta^l} - \omega^2 \mathbf{v}^{aT} \mathbf{M} \mathbf{v} - \mathbf{v}^{aT} \mathbf{f} - \mathbf{v} \mathbf{f}^H \right) d\theta, \quad (4.6)$$

where \mathbf{A}_{kl} are generalised stiffness matrices and \mathbf{M} is the mass matrix. Hamilton's principle (4.2) is applied and from the variation of the displacements in the adjoint system a set of coupled ordinary differential equations follows

$$\left[-\mathbf{A}_{11} \frac{\partial^2}{\partial \theta^2} + (\mathbf{A}_{01} - \mathbf{A}_{10}) \frac{\partial}{\partial \theta} + \mathbf{A}_{00} - \omega^2 \mathbf{M} \right] \mathbf{v}(\theta, \omega) = \mathbf{f}(\theta, \omega). \quad (4.7)$$

4.1.2 Free response, forced response and damping

By setting $\mathbf{f} = 0$, the homogeneous case is obtained for which solutions are given by exponential functions of type

$$\mathbf{v}(\theta, \omega) = \mathbf{\Psi}(\omega)e^{-j\kappa\theta}. \quad (4.8)$$

These functions can be physically interpreted as waves of cross-sectional mode shape $\mathbf{\Psi}$ propagating along the circumferential direction with polar wave number κ . Inserting (4.8) into (4.7) gives

$$(-\mathbf{K}_2\kappa^2 - \mathbf{K}_1j\kappa + \mathbf{K}_0 - \omega^2\mathbf{M})\mathbf{\Psi} = \mathbf{0}, \quad (4.9a)$$

where

$$\mathbf{K}_0 = \mathbf{A}_{00}, \quad \mathbf{K}_1 = \mathbf{A}_{01} - \mathbf{A}_{10}, \quad \mathbf{K}_2 = -\mathbf{A}_{11}. \quad (4.9b)$$

This is a twin-parameter eigenvalue problem in ω and κ for which two solution strategies exist. The first option is to specify the frequency ω for which the problem should be solved. In this case a quadratic eigenvalue problem follows. The other possibility is to set κ to a particular wave order which means that (4.9a) reduces to a linear eigenvalue problem which is easier to solve than the quadratic one. Because of the periodicity condition around the tyre circumference, κ can only be set to an integer n . This number represents the order, i.e. the number of full wave lengths, of the wave motion in circumferential direction. For any particular n , a set of eigenvalues $\omega_{n,s}^2$ and eigenvectors $\mathbf{\Psi}_{n,s}$ will be the solution to (4.9a). Herein, each s represents one solution over the cross-section, i.e. one cross-sectional mode shape¹. Examples of three different $\mathbf{\Psi}_{n,s}$ are shown in Fig. 4.4. Applying this ansatz to (4.9a) it is

$$(-\mathbf{K}_2n^2 - \mathbf{K}_1jn + \mathbf{K}_0 - \omega_{n,s}^2\mathbf{M})\mathbf{\Psi}_{n,s} = \mathbf{0}. \quad (4.10)$$

If damping is disregarded, then all \mathbf{K}_i ($i = 0, 1, 2$) and the \mathbf{M} are real and symmetric or skew-symmetric. From this the relation between waves travelling in positive ($n > 0$) and negative circumferential direction ($n < 0$) can be deduced as:

$$\omega_{-n,s} = \omega_{n,s} \quad (4.11a)$$

$$\mathbf{\Psi}_{-n,s} = \mathbf{\Psi}_{n,s}^*. \quad (4.11b)$$

¹Due to the wave ansatz and the high structural damping it is apt to speak of *waves* when referring to the circumferential direction. The solutions for the cross-sectional motion are obtained as eigenvectors for a particular n , which is similar to how mode shapes are obtained for simpler structures. Hence, the cross-sectional motion will be referred to as *modes*.

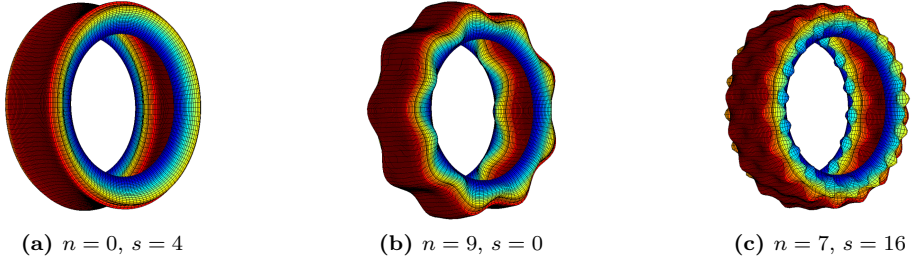


Fig. 4.4 Examples of three free response solutions of type $\Psi_{n,s} e^{-jn\theta}$. Note that due to the wave ansatz, these deformation shapes are not stationary in circumferential direction but move around the tyre. Exceptions are solutions for $n = 0$.

In [76] it is shown that for proportional damping of type $\bar{\mathbf{K}}_i = (1 + j\eta(\omega))\mathbf{K}_i$, (where $i = 0, 1, 2$ and $\eta(\omega)$ being the loss factor) the inhomogeneous version of (4.9a) is given by

$$(-\bar{\mathbf{K}}_2 n^2 + \bar{\mathbf{K}}_1 jn + \bar{\mathbf{K}}_0 - \omega^2 \mathbf{M}) \Xi_n \mathbf{C}_n = \mathbf{F}_n(\omega). \quad (4.12)$$

Herein, Ξ_n is a matrix collecting all free response eigenvectors $\Psi_{n,s}$ for a specific n . \mathbf{C}_n are the amplitudes of the cross-sectional modes s contributing to circumferential order n . $\mathbf{F}_n(\omega)$ results from the expansion of the excitation force $\mathbf{f}(\theta, \omega)$ into circumferential orders. For a tyre circumference which is discretised into C equidistant intervals of length Δ , and a excitation force which is piece-wise constant over the interval $\theta \in [\theta_c - \Delta/2, \theta_c + \Delta/2]$, this expansion gives

$$\mathbf{F}_n(\omega) = \sum_{c=1}^C \mathbf{F}_{\text{lat}}(\omega) \frac{\sin(n\Delta/2)}{n\pi\Delta} e^{-jn\theta_c}, \quad (4.13)$$

where \mathbf{F}_{lat} is the lateral force distribution. By multiplying both sides of (4.12) from the left with Ξ_n^H , the orthogonality property of the cross-sectional modes can be used to derive the modal amplitudes as

$$C_{n,s}(\omega) = \frac{\Psi_{n,s}^H \mathbf{F}_n(\omega)}{[(1 + j\eta(\omega))\omega_{n,s}^2 - \omega^2] \sqrt{m_{n,s}}}. \quad (4.14)$$

The factor $m_{n,s}$ is the modal mass, which is given by the orthogonality relation

$$\delta_{s,t} m_{n,s} = \Psi_{n,s}^H \mathbf{M} \Psi_{n,t}, \quad (4.15)$$

where δ is the Kronecker symbol.

Similar to (4.11a) it follows

$$m_{-n,s} = m_{n,s}. \quad (4.16)$$

The total displacement field on the tyre, $\mathbf{v}(\theta, \omega)$, can finally be obtained as a summation of the contribution of S cross-sectional modes and $-N$ to N circumferential waves

$$\begin{aligned} \mathbf{v}(\theta, \omega) &= \sum_{n=-N}^N \sum_{s=1}^S C_{n,s} \frac{\Psi_{n,s}}{\sqrt{m_{n,s}}} e^{-jn\theta} \\ &= \sum_{n=-N}^N \sum_{s=1}^S \frac{\Psi_{n,s}^H \mathbf{F}_n(\omega)}{[(1 + j\eta(\omega))\omega_{n,s}^2 - \omega^2]m_{n,s}} \Psi_{n,s} e^{-jn\theta}. \end{aligned} \quad (4.17)$$

By virtue of relations (4.11) and (4.16), this can be written as

$$\mathbf{v}(\theta, \omega) = \sum_{n=0}^N \left(\sum_{s=1}^S A_{n,s}(\omega) \Psi_{n,s} e^{-jn\theta} + \sum_{s=1}^S B_{n,s}(\omega) \Psi_{n,s}^* e^{jn\theta} \right). \quad (4.18)$$

For $n > 0$ the amplitudes $A_{n,s}$ and $B_{n,s}$ are given as

$$A_{n,s}(\omega) = \frac{\Psi_{n,s}^H \mathbf{F}_n(\omega)}{[(1 + j\eta(\omega))\omega_{n,s}^2 - \omega^2]m_{n,s}} \quad (4.19a)$$

$$B_{n,s}(\omega) = \frac{\Psi_{n,s}^T \mathbf{F}_{-n}(\omega)}{[(1 + j\eta(\omega))\omega_{n,s}^2 - \omega^2]m_{n,s}}. \quad (4.19b)$$

For the special case $n = 0$ it is

$$A_{0,s}(\omega) = \frac{\Psi_{n,s}^H \mathbf{F}_{\text{lat}}(\omega)}{\pi[(1 + j\eta(\omega))\omega_{n,s}^2 - \omega^2]m_{n,s}} \quad (4.20a)$$

$$B_{0,s}(\omega) = 0. \quad (4.20b)$$

By using (4.18) instead of (4.17) the computational burden can be significantly reduced as the eigenvalue problem (4.10) only needs to be solved $N + 1$ times instead of the original $2N + 1$ times.

While the described modal summation procedure is numerically efficient, it cannot be applied for non-proportional damping², i.e. when different loss factors are applied to the entries of \mathbf{K}_i in (4.12). For some applications it is desirable to assign different loss factors to for example the highly-damped tread rubber and the less damped carcass. In this case the response for a particular wave order n can be calculated (see [75]) by direct matrix inversion of the inhomogeneous version of (4.9a)

$$\mathbf{v}_n(\omega) = [-\mathbf{K}_2 n^2 - \mathbf{K}_1 j n + \mathbf{K}_0 - \omega^2 \mathbf{M}]^{-1} \mathbf{F}_n(\omega). \quad (4.21)$$

Similar to (4.18), the total displacement field can then be expressed as

$$\mathbf{v}(\theta, \omega) = \mathbf{v}_0(\omega) + \sum_{n=1}^N \mathbf{v}_n(\omega) e^{-jn\theta} + \mathbf{v}_{-n}(\omega) e^{jn\theta}, \quad (4.22)$$

where \mathbf{v}_{-n} is obtained from \mathbf{v}_n by reversing the sign of those degrees-of-freedom which correspond to displacements in θ -direction, or to rotations around the r - or x -axes [29].

A considerable disadvantage of the direct procedure is the computational burden which can be quite significant as the matrix inversion has to be performed for every ω and n . For the applications presented in this thesis the modal summation approach is typically at least ten times faster than the direct procedure. Due to this a modal summation approach is used for most of the studies. The exception are the rolling resistance calculations presented in Section 6.3 and *Paper III*.

4.1.3 Element formulation

Only the tyre structure is modelled, but not the air cavity. The fluid/structure coupling is of minor relevance for tyre vibrations [62] unless hub forces are considered. The wheel is also not included in the model. Tyre motion is blocked at the bead.

As very detailed derivations of the elements used in the WFE tyre model can be found in [72, 75], only a very brief overview is given in the following. Two types of elements are available for the tyre cross-section modelling: (an)isotropic, quadrilateral solid elements of Lagrange type with nine nodes, and anisotropic, doubly-curved 3-node deep shell elements accounting for rotational inertia, shearing across the thickness, and pre-tension due to tyre inflation.

While in general linearized strain-displacement relations are used, it is necessary to retain quadratic terms for expressions involving the membrane strains due to

²It is possible to use non-proportional damping while solving (4.10) to obtain damped, i.e. complex, eigenvectors and eigenvalues. However, since the orthogonality relations no longer lead to matrix diagonalisation, the step from (4.12) to (4.14) is no longer possible.

pre-tension [75]. In Section 3.2.3 it was stated that tyre/road contact models which are based on a convolution approach can only be formulated for linear tyre models. This requirement is not violated by the non-linear pre-tension terms used in the shell formulation. The pre-tension terms merely define an initial equilibrium state for the shell elements about which small, linearized vibrational motion is executed. As the pre-tension does not change during a simulation, only linear effects are included in the dynamic response of the tyre. The existence of the tyre's Green's function is assured.

4.1.4 Advantages of WFEM

Compared to purely analytical or numerical tyre models, the presented WFEM approach has several advantages which make it particularly useful for a study as presented here. By modelling the cross-section with individual elements, WFEM can better account for the complex geometry and material properties of a tyre than analytical models can. By applying a wave approach in the circumferential direction, the computational burden is significantly reduced compared to FE models as matrices are smaller and solutions can be restricted to the wave orders of interest. The results are also more readily interpretable as the contributions of individual wave orders can easily be identified. The geometrical accuracy in the cross-section and the numerical efficiency imply that the usable frequency range is larger than when either analytical or FE modelling are used. Results can easily be analysed in any combination of frequency, wave-order and/or, in the case of rolling resistance, cross-sectional distribution. Moreover, the numerical effort is small enough to allow for extended parameter studies.

4.2 The tyre/road interaction model

4.2.1 Basic contact formulation

The contact model is based on the convolution approach as presented by Kropp [94] and its subsequent enhancements by several authors [75, 96, 97, 128].

The time-dependent position of a point e on the tyre surface can be written as

$$Z_e(t) = Z_0(t) - Z_{T,e}(t) + u_e(t), \quad (4.23)$$

where $Z_0(t)$ and $Z_{T,e}(t)$ are the position of the rim centre and the tyre contour as shown in Fig. 4.5. $u_e(t)$ is the dynamic structural response at point e which is caused by the present and past forces at all contact points m . For a linear

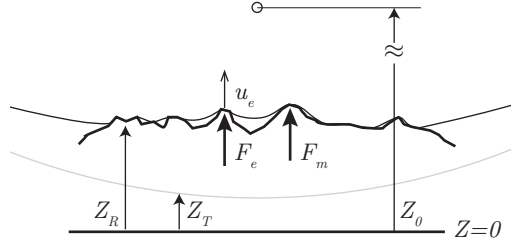


Fig. 4.5 Contact geometry between tyre and road. The reference surface is located at $Z = 0$, the rim centre at Z_0 , the undeformed tyre contour (grey) is given by Z_T and the road roughness profile by Z_R . F_e and F_m are the contact forces acting at points e and m , and u_e is the dynamic response of the structure in point e .

time-invariant system it is given as

$$u_e(t) = \sum_m F_m(t) * g_{m,e}(t) \quad (4.24a)$$

$$= \sum_m \int_{-\infty}^{\infty} F_m(\tau) g_{m,e}(t - \tau) d\tau. \quad (4.24b)$$

$*$ is the convolution operator and $g_{m,e}$ is the displacement Green's function in the Eulerian reference frame for a point e due to a force at point m . Assuming causality and that the system is at rest for times $t < 0$, a time discretised version of (4.24b) for $t_N = N\Delta t$ is obtained as

$$u(N\Delta t) = \sum_m \sum_{n=0}^N F_m g_{m,e}((N-n)\Delta t) \Delta t \quad (4.25a)$$

$$= \sum_m F_m(t_N) g_{m,e}(0) \Delta t + \sum_m \sum_{n=0}^{N-1} F_m g_{m,e}((N-n)\Delta t) \Delta t. \quad (4.25b)$$

As the second term in (4.25b) represents past, known values of the contact forces, it can be considered a constant at each time step. As a matrix expression for all possible contact points m , (4.25b) becomes

$$\mathbf{u}(t_N) = \mathbf{G}_0 \mathbf{F}(t_N) + \mathbf{u}_{\text{old}}(t_N). \quad (4.26)$$

Here, \mathbf{G}_0 is a $m \times m$ matrix containing the values of the Green's functions for $t = 0$. Besides the displacements $\mathbf{u}(t_N)$ also the contact forces $\mathbf{F}(t_N)$ are still unknown in (4.26). By defining $\Delta\mathbf{u}(t_N) = \mathbf{u}(t_N) - \mathbf{u}_{\text{old}}(t_N)$, (4.26) can be rearranged to

$$\mathbf{F}(t_N) = \mathbf{G}_0^{-1} \Delta\mathbf{u}(t_N). \quad (4.27)$$

The inverse \mathbf{G}_0^{-1} is called the influence matrix. It is only defined when the first values of the Green's function are not zero.

From the boundary conditions at the tyre/road interface follows

$$\mathbf{F}(t_N) \geq \mathbf{0} \quad (4.28a)$$

$$\mathbf{d}(t_N) = \mathbf{Z}_{\mathbf{T}}(T_N) + \mathbf{u}_{\text{old}}(t_N) + \Delta\mathbf{u}(t_N) - \mathbf{Z}_{\mathbf{R}}(t_N) \geq \mathbf{0} \quad (4.28b)$$

$$\mathbf{F}(t_N)^T \mathbf{d}(t_N) = 0, \quad (4.28c)$$

where Z_R is the road roughness profile as shown in Fig. 4.5.

Under the omission of adhesion, these conditions state that for each time step t_N there are only two valid states for a contact point e : tyre and road are either in contact with $d_e(t_N) = 0$ and a positive compression force $F_e(t_N)$, or they are separated by a distance $d_e(t_N) > 0$, in which case the contact force $F_e(t_N) = 0$. A non-linear contact problem is formed by (4.27) and the contact constraints (4.28a), (4.28b) and (4.28c). This can be solved iteratively for every time step using for example the (damped) Newton-Raphson algorithm [75, 97].

4.2.2 Small-scale tread/road interaction

As has been pointed out in Section 3.2.3, small-scale roughness phenomena can have a considerable effect on the contact behaviour. The difference between the apparent and the real area of contact affects the contact stiffness (see Figures 3.2 and 4.6a). Moreover, as shown in Fig. 3.3, the real area of contact, and with it the contact stiffness, also changes during the contact duration. One solution to account for this is to use a sufficiently fine resolution of the contact zone. Yet, with respect to the necessary numerical effort, this is often not reasonable. Another solution is to introduce non-linear contact springs between the contact points [97].

The same approach is used here, see Fig. 4.6b. Yet, as the determination of the non-linear contact stiffnesses is a rather advanced task, only contact springs with constant stiffness are used. This means that difference between real and apparent area of contact is included, while the change in contact area during contact is not.

A similar argument can be made for rolling losses induced by the small-scale road roughness. The interaction between the road asperities and the highly damped tread rubber is not adequately represented by a contact resolution which is within

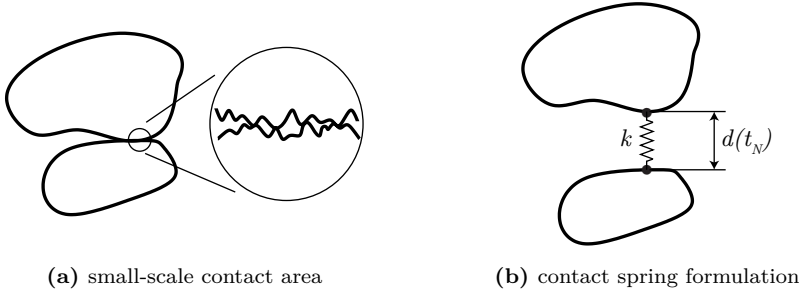


Fig. 4.6 (a) Due to the small-scale surface roughness the real area of contact is smaller than the apparent. (b) Contact springs are introduced to account for this.

numerically reasonable limits. The losses due to the small-scale tread deformations can instead be included by adding a non-linear damping term to the contact formulation. Compared to a viscous damping, a non-linear damping model has the advantage of not resulting in a discontinuous contact force at initial contact and separation. Damping furthermore depends on the indentation which is physically reasonable as the contact area increases with deformation [129].

Introducing contact springs and non-linear damping, the set of equations (4.28) is reformulated to read

$$F_e(t_N) = \left[k d_e(t_N) + c d_e(t_N) \frac{\partial}{\partial t_N} d_e(t_N) \right] \cdot \mathcal{H}\{d_e(t_N)\}, \quad (4.29a)$$

$$\mathbf{d}(t_N) = \mathbf{Z}_R(t_N) - \mathbf{Z}_T(T_N) - \mathbf{u}(t_N). \quad (4.29b)$$

with a spring stiffness k , a damping coefficient c , and the Heaviside operator \mathcal{H} .

Equations (4.29) and (4.27) formulate a new non-linear contact problem which is solved to obtain the time-dependent contact forces in the Eulerian reference frame. The contact forces are then rotated around the tyre and Fourier transformed to yield the frequency dependant forces in the Lagrangian coordinate system.

4.2.3 Implementation details and input parameters

The tyre/road contact modelling is divided into two phases: stationary loading and rolling. During the stationary loading phase, the tyre is slowly pressed onto a road patch until the required axle load F_z is reached. This determines the distance between tyre hub and road, which is kept constant in the following. Now the rolling phase starts. For each time step, the contact regions from the tyre and road surface

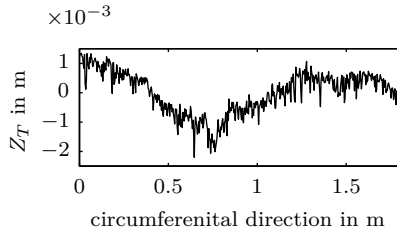


Fig. 4.7 Example of a road surface profile with pronounced unevenness. The position where the static loading is performed influences the average contact force during rolling.

profiles are shifted in accordance with the contact resolution. Using u_{old} from the previous time step, the contact force is calculated. Quasi-steady state conditions are reached after two or three revolutions when low-frequency oscillations induced by the start of rolling have died out. The procedure of keeping the tyre/road approach constant during rolling has some implications. In particular the total contact force will vary with each time step. Especially for roads with a pronounced unevenness, see the example in Fig. 4.7, these variations can be 20% and more. Physically this is not unreasonable as it resembles the influence of the inertia of the car body and the suspension on the tyre/road contact. The effect has to be taken into account when the rolling resistance coefficient is calculated.

The spring stiffness k is estimated based on comparisons of measured and simulated tyre footprints. Non-linear damping has only been used for the study presented in Section 6.3/*Paper III*, where the damping coefficient c was also determined based on footprint considerations. For all other studies c was set to zero.

Accurate results are only obtained when three-dimensional road roughness data is used, i.e. it is not sufficient to calculate tyre/road interaction based on one road surface profile without lateral variation, cf. [52, Paper C] and the results presented in Section 6.2/*Paper II*. Accordingly, throughout this thesis detailed three-dimensional laser scans of drum-mounted road patches or segments of test tracks are used as input data for the tyre/road simulations. An example of a calculated tyre/road interaction is given in Fig. 4.8.

4.3 Influence of the tread pattern

The influence of the tread pattern is twofold. Geometrically, it influences which areas of the tyre are in contact with the ground. This also results in a variation of the local contact stiffness. Additionally, the tread pattern influences the dynamic tyre response. These two effects are particularly pronounced for tyres with large

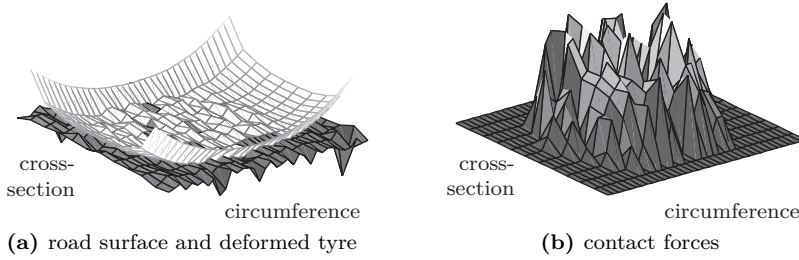


Fig. 4.8 Example of tyre/road interaction.

circumferential grooves, as is the case for two of the tyres considered in this thesis, see Fig. A.1. Accordingly, these voids are included in the WFEM cross-sectional mesh, cf. Figures A.3 and A.5. Individual tread blocks cannot explicitly be included in the tyre geometry as WFEM requires the tyre to be homogenous in circumferential direction. Within the scope of the present study this is no limitation. The eigenfrequencies of typical tread blocks of passenger car tyres are very high in frequency, see [95], and thus outside the frequency regions of interest for both rolling losses and rolling noise. This is not necessarily the case for the larger tread blocks of truck tyres. However, for a WFE truck tyre model which is as detailed as the one shown in Fig. A.5 only the tread dynamics in circumferential direction are neglected. This is of minor importance as long as only radial contact forces for steady-state rolling and not tangential contact forces for accelerating or braking are considered.

While an explicit modelling of tread blocks is not necessary in the tyre modelling, there is an influence of the presence of voids in the rubber on the tread's mass and stiffness. This is a global effect which can be handled by mass and stiffness adjustments of the solid elements forming the tread layer.

A typical tyre profile is shown in Fig. 4.9a. It is possible to include such a tread pattern in the tyre/road contact simulations via the tyre profile \mathbf{Z}_T in Eq. (4.29b). However, the needed spatial discretisation is so fine that the computational burden would be extreme; not only for the contact modelling but also for the tyre response calculations. To keep the numerical effort reasonable, a different approach is chosen, see Fig. 4.9b. Based on the lateral and circumferential contact resolution, the whole tread over the tyre width and circumference is divided into small areas, each representing one individual contact point e in Eq. (4.29). For each of these areas the surface fraction of rubber can be determined in advance as

$$\Phi_{e,r} = \frac{A_{e,r}}{A_{e,r} + A_{e,v}}, \quad (4.30)$$

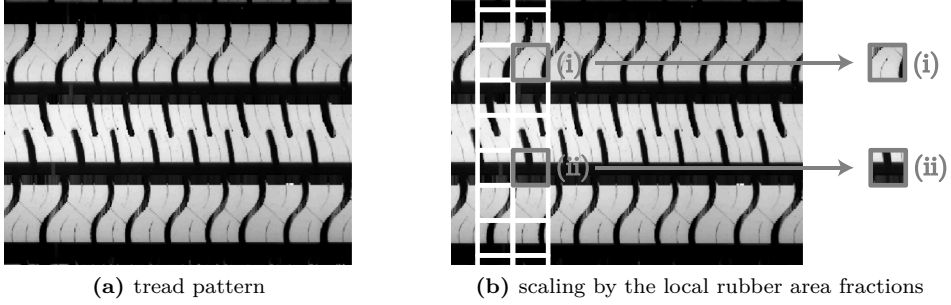


Fig. 4.9 (a) Example of a tread pattern. (b) Scheme for scaling the contact stiffnesses by the amount of rubber in the respective contact patch. There is more rubber in patch (i) than in patch (ii). Accordingly the local contact stiffness in (i) will be nearly unchanged while it will be very little in (ii), i.e. $k_i \gg k_{ii}$.

where $A_{e,r}$ and $A_{e,v}$ denote the rubber and void areas in the contact patch e . $\Phi_{e,r}$ is then used to scale the local contact stiffness, i.e. k is replaced by $k_e = k\Phi_{e,r}$ in (4.29a). A similar approach has been successfully used in the SPERoN model [130]. The damping coefficient c is scaled in the same way.

The lateral size of a contact patch in the tyre/road interaction calculations is equivalent to the width of a solid element in the tyre cross-section mesh, e.g. in Fig. 4.3. By averaging $\Phi_{e,r}$ over the circumference a scaling factor for the stiffness and mass of each solid element is obtained. These scaling factors are applied to the corresponding elements when assembling \mathbf{A}_{kl} and \mathbf{M} in Eq. (4.6).

4.4 The half-space boundary element method radiation model

4.4.1 Governing equations

The basis for the radiation calculations with the half-space BEM is the Helmholtz equation for an homogeneous, non-moving medium

$$\nabla^2 p(\vec{x}) + k_0^2 p(\vec{x}) = -\varphi(\vec{x}), \quad (4.31)$$

where $p(\vec{x})$ is the sound pressure at a point $\vec{x} = (X, Y, Z)$ inside the domain V . ∇^2 is the Laplace operator, $k_0 = \omega/c_0$ the wave number and c_0 the speed of sound in the acoustic domain. $\varphi(\vec{x})$ is a spatially distributed source function representing contribution from harmonic acoustic sources within V .

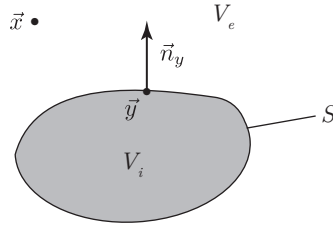


Fig. 4.10 Domain definition for the exterior BEM problem: the internal domain V_i is separated from the external domain V_e by the surface S . The point \vec{x} is located in V_e and \vec{y} lies on S . \vec{n}_y is the normal vector to the surface S in point \vec{y} .

A Green's function $g(\vec{x}, \vec{y})$ is the solution of Eq. (4.31) for a point source at $\vec{y} = (X_s, Y_s, Z_s)$

$$\nabla^2 g(\vec{x}, \vec{y}) + k_0^2 g(\vec{x}, \vec{y}) = -\delta(\vec{x}, \vec{y}), \quad (4.32)$$

with $\delta(\vec{x}, \vec{y})$ as Dirac delta function. For an unbounded three-dimensional space the Green's function is

$$g(\vec{x}, \vec{y}) = \frac{e^{-jk_0 r}}{4\pi r}, \quad (4.33)$$

where

$$r = \|\vec{x} - \vec{y}\| = \sqrt{(X - X_s)^2 + (Y - Y_s)^2 + (Z - Z_s)^2} \quad (4.34)$$

is the distance between the points \vec{x} and \vec{y} .

Multiplication of (4.31) with $g(\vec{x}, \vec{y})$ and (4.32) with $p(\vec{x})$, and subsequent subtraction of (4.31) from (4.32) combines the two equations. After integration over the domain V , indirect application of Green's second identity, and some algebra (see e.g. [108]) the Kirchhoff-Helmholtz integral equation for exterior problems as shown in Fig. 4.10 results as

$$C(\vec{x}) p(\vec{x}) = - \int_S \left(p(\vec{y}) \frac{\partial g(\vec{x}, \vec{y})}{\partial \vec{n}_y} + j\omega \rho_0 v_n(\vec{y}) g(\vec{x}, \vec{y}) \right) dS_y + p_{\text{inc}}(\vec{x}), \quad (4.35)$$

with

$$C(\vec{x}) = \begin{cases} 1 & \vec{x} \text{ in the exterior domain } V_e \\ \frac{1}{2} & \vec{x} \text{ on the surface } S \\ 0 & \vec{x} \text{ in the interior domain } V_i. \end{cases} \quad (4.36)$$

Herein, \vec{y} is taken to lie on the boundary S between the inner and exterior domains V_i and V_e . \vec{x} is located in V_e and $\partial g(\vec{x}, \vec{y})/\partial \vec{n}_y$ is the directional derivative of $p(\vec{y})$ in the direction of the normal vector \vec{n}_y at the surface interval dS_y . ρ_0 is the density of the acoustic medium and v_n is the normal velocity on dS_y . The contribution of an external incident sound field $p_{\text{inc}}(\vec{x})$ is given as

$$p_{\text{inc}}(\vec{x}) = \int_V \varphi(\vec{y}) g(\vec{x}, \vec{y}) dX_S dY_S dZ_S. \quad (4.37)$$

Physically, the right hand side of (4.35) can be interpreted as the contribution of individual volume sources (i.e. monopoles $j\omega\rho_0 v_n(\vec{y}) g(\vec{x}, \vec{y})$), and pressure sources (i.e. dipoles $p(\vec{y}) \partial g(\vec{x}, \vec{y})/\partial \vec{n}_y$) located on the surface S to the sound pressure $p(\vec{x})$.

4.4.2 Numerical implementation

The surface S is discretised into N surface elements and the point \vec{x}_m , $m = 1 \dots N$, is subsequently placed at the centres of all elements. For each position m , the contribution from all surface intervals $j = 1 \dots N$ is calculated. This gives N equations of form

$$\frac{1}{2} p(\vec{x}_m) = - \sum_{j=1}^N \int_{S_j} \left(p(\vec{y}_j) \frac{\partial g(\vec{x}_m, \vec{y}_j)}{\partial \vec{n}_{y_j}} + j\omega\rho_0 v_n(\vec{y}_j) g(\vec{x}_m, \vec{y}_j) \right) dS_{y_j} + p_{\text{inc}}(\vec{x}_m). \quad (4.38)$$

Replacing S_j with constant planar elements and application of one-point Gauss-Legendre quadrature yields

$$\frac{1}{2} p(\vec{x}_m) = - \sum_{j=1}^N \left(p(\vec{y}_j) \frac{\partial g(\vec{x}_m, \vec{y}_j)}{\partial \vec{n}_{y_j}} + j\omega\rho_0 v_n(\vec{y}_j) g(\vec{x}_m, \vec{y}_j) \right) \Delta S_{y_j} + p_{\text{inc}}(\vec{x}_m). \quad (4.39)$$

Stepping through all points \vec{x}_m , $m = 1 \dots N$, on the surface, the following matrix equation is obtained

$$\mathbf{C} \mathbf{p}_S = \mathbf{H} \mathbf{p}_S + j\omega\rho_0 \mathbf{G} \mathbf{v}_S + \mathbf{p}_{\text{inc}}. \quad (4.40)$$

Here, \mathbf{p}_S and \mathbf{v}_S denote the pressure and the normal velocity at the surface elements. The kernel functions $\partial g(\vec{x}_m, \vec{y}_j)/\partial \vec{n}_{y_j}$ and $g(\vec{x}_m, \vec{y}_j)$ are included in the matrices \mathbf{H} and \mathbf{G} , and $\mathbf{C} = \mathbf{I}/2$, with \mathbf{I} as identity matrix.

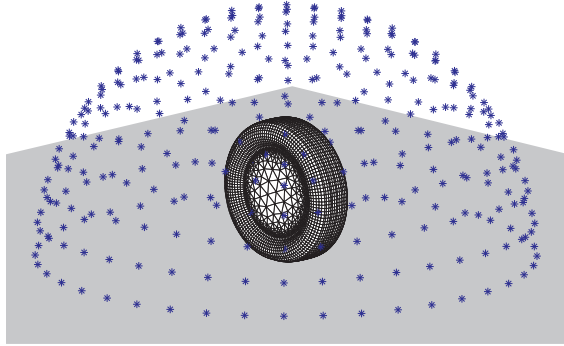


Fig. 4.11 The BEM tyre representation, the reflecting ground and a possible evaluation surface.

Depending on the boundary conditions, \mathbf{v}_S or \mathbf{p}_S or a combination of both are known in (4.40). Sorting the unknown and known parts into left- and right-hand side terms, a set of equations of the form

$$\mathbf{A}\mathbf{x}_S = \mathbf{b} \quad (4.41)$$

is obtained. The solution \mathbf{x}_S gives the unknown boundary values on S . Now that both \mathbf{v}_S and \mathbf{p}_S are known on S , (4.35) can be solved for an arbitrary receiver position \vec{x} in the exterior domain. The procedure involves the same discretisation steps as for Equations (4.38) and (4.39), and yields

$$p(\vec{x}) = p_{\text{inc}}(\vec{x}) - \sum_{m=1}^N \left(p(\vec{y}_m) \frac{\partial g(\vec{x}, \vec{y}_m)}{\partial \vec{n}_{\vec{y}_m}} + j\omega\rho_0 v_n(\vec{y}_m) g(\vec{x}, \vec{y}_m) \right) \Delta S_{y_m}. \quad (4.42)$$

The numerically critical step in BEM is solving (4.41) as the matrix \mathbf{A} has some unfavourable properties. It is fully populated and, as the surface intervals ΔS_{y_j} do not need to be of equal size, is not necessarily symmetric. If CHIEF points are added to avoid possible non-uniqueness problems (cf. [131, Cha. 3]), \mathbf{A} is not even quadratic. As a consequence, storage and computation costs can be quite substantial for BEM.

4.4.3 Tyre/road noise specialities

In the case of the tyre/road noise simulations, the domain surface S is the tyre surface and the vibrational field on the tyre gives the normal surface velocity \mathbf{v} in (4.40). Accordingly, the solution of (4.41) gives the surface pressure \mathbf{p}_S , and

(4.42) can be used to calculate the sound pressure at any arbitrary point around the tyre, for example on an evaluation half-sphere as shown in Fig. 4.11.

An important property which has been left out so far is the reflection at the road surface. In principal, the ground could simply be included in the BEM calculations as another discretised body. However, this raises the already high computational costs even further. It is numerically more efficient to modify the Green's function (4.33) to include the effect of the ground reflection:

$$g(\vec{x}, \vec{y}) = \frac{e^{-jk_0 r_1}}{4\pi r_1} + \frac{e^{-jk_0 r_2}}{4\pi r_2}. \quad (4.43)$$

Here, $r_1 = \|\vec{y} - \vec{x}\|$ and $r_2 = \|\vec{y} - \vec{x}'\|$, where \vec{x} is the position of the receiver and \vec{x}' is the position of \vec{x} after having been mirrored at the ground plane. Eq. (4.43) is valid for the case of a perfectly rigid ground, i.e. the normal ground impedance is $Z_p = \infty$. Formulations for arbitrary ground impedances, which are for example necessary to model reflection at porous asphalt surfaces, have been shown by Brick [108]. Within this work only the rigid case is considered.

Numerically problematic is the simulation of the sound radiation out of the contact region. In the contact area high surface velocities on the tyre coincide with very narrow gaps between tyre and road. This leads to near-singular conditions. To deal with this problem, a two step process is used. First, the tyre is lifted by 1 mm from the road surface. Secondly, an adaptive integration routine as proposed in [108] is used. Elements close to or in the contact region are divided into sub-intervals proportional to the relative distance between element and ground. Gauss-Legendre integration points are then assigned to these sub-elements. The Green's functions and their derivatives are finally given by the sum of the sub-interval values. Using this approach, calculation times are not significantly affected as the total number of elements does not change. The validity of this procedure has been proven by Brick [108] for calculations of the horn-effect.

The spatial resolution of the tyre's vibrational field, which serves as the input data for the BEM calculations, is given by the cross-sectional WFEM mesh and the circumferential tyre discretisation as used in the contact modelling. It is neither physically nor numerically useful to use the full available resolution. If a maximum frequency of interest of 3400 Hz is assumed, the smallest wave length in air is 0.1 m. Applying a six elements per wave length criterion, elements can be 1.67 cm long. The length of the bead to bead cross-section perimeter of for example the 175/65 R14 tyre considered here is 0.35 m and the circumference is 1.82 m. This means that 21 boundary elements over the cross-section and 109 over the circumference are sufficient to fulfil the wave length criteria for the air-borne part. The situation is more complicated for the structure-borne part as there is no simple rule to determine the necessary number of wave lengths which are to be considered for a specific frequency. This is due to the complex interaction

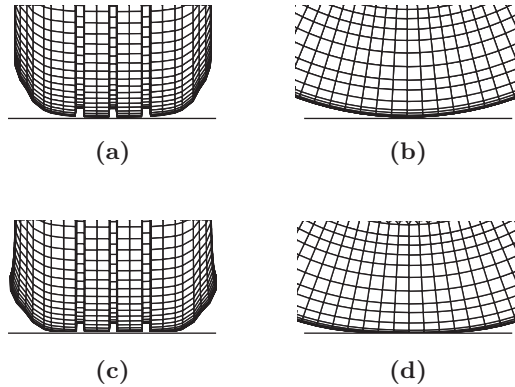


Fig. 4.12 The effect of static deformation on the BEM mesh. (a) front view undeformed mesh, (b) side view undeformed mesh, (c) front view deformed mesh, and (d) side view deformed mesh.

between cross-sectional and circumferential motion, the variety of different wave types, the complex dispersion relations and the large number of existing modes for higher frequencies (cf. Section 6.4 or *Paper IV*). Yet, in [76] it was shown that due to their radiation efficiency mainly low-order tyre modes are responsible for sound radiation in the frequency range up to 3 kHz. This means that not all vibrational orders actually need to be considered for the radiation calculations. In [76] good agreement with measurements was achieved for a maximum order of 24 in circumferential direction and 20 over the cross-section. The same range of orders is used here for the 205/55 R16 and 175/65 R14 tyres. For the 315/80 R22.5 tyre the order is increased to 50 in both directions. Under this condition the required resolution for the airborne part is also sufficient for an accurate description of the vibrational field. The final BEM mesh needs only a fourth of the circumferential resolution and roughly half the cross-sectional resolution of the vibrational mesh.

The importance of the tyre/road geometry in the contact region for the amplification of sound by the horn effect has been discussed in Section 2.2.3. In view of this, the BEM mesh is not based on the original undeformed tyre shape, but on the deformed tyre shape under static loading. The difference is shown in Fig. 4.12. The BEM mesh is completed by adding rigid wheel covers on both tyre sides, see Fig. 4.11. CHIEF points are distributed inside the tyre to avoid numerical irregularities.

4.5 Calculating rolling resistance

Due to energy conservation, rolling losses can be calculated as input power for steady-state rolling conditions. The most general expression for the time-averaged input power into the tyre is given as

$$P_{\text{tyre}} = \frac{1}{T} \sum_i \int_0^{2\pi} \int_0^T F_i(t, \theta) \frac{\partial v_i(t, \theta)}{\partial t} dt d\theta. \quad (4.44)$$

Herein, F_i and $\partial v_i/\partial t$ denote the contact force and tyre velocity for the lateral contact track i . In [42] it is shown that for a WFE tyre model the equivalent expression in the frequency and circumferential wave order domains is given as

$$P_{\text{tyre}} = 2\pi \sum_{n=-N}^N \sum_{m=0}^M j\omega_m [\mathbf{F}_{-n}^H(\omega_m) \mathbf{v}_{-n}(\omega_m) - \mathbf{F}_n^T(\omega_m) \mathbf{v}_n^*(\omega_m)]. \quad (4.45)$$

The nodal forces $\mathbf{F}_{\pm n}$ are given by (4.13) and the nodal displacements $\mathbf{v}_{\pm n}$ can be obtained from (4.17) or (4.21). Eq. (4.45) conveniently allows the identification of the contribution of individual wave orders or frequencies to the rolling losses. Using (4.7), $\mathbf{F}_n(\omega_m)$ can be replaced by

$$[\mathbf{A}_{00} + jn\mathbf{A}_{01} - jn\mathbf{A}_{10} + n^2\mathbf{A}_{11} - \omega_m^2\mathbf{M}] \mathbf{v}_n(\omega_m) = \mathbf{F}_n(\omega_m), \quad (4.46)$$

giving the internally dissipated power P_{int} as

$$P_{\text{int}} = 2\pi \sum_{n=-N}^N \sum_{m=0}^M j\omega_m \cdot \left[\mathbf{v}_{-n}^H \left(\mathbf{A}_{00}^H + jn\mathbf{A}_{01}^H - jn\mathbf{A}_{10}^H + n^2\mathbf{A}_{11}^H - \omega_m^2\mathbf{M}^H \right) \mathbf{v}_{-n} - \mathbf{v}_n^T \left(\mathbf{A}_{00}^T - jn\mathbf{A}_{01}^T + jn\mathbf{A}_{10}^T + n^2\mathbf{A}_{11}^T - \omega_m^2\mathbf{M}^T \right) \mathbf{v}_n^* \right], \quad (4.47)$$

where for the sake of readability the ω_m dependence of $\mathbf{v}_{\pm n}$ has been omitted. For completeness, the Hermitian of \mathbf{M} is retained in the second line even though only real mass matrices are considered here. Obviously, it is $P_{\text{int}} = P_{\text{tyre}}$. The special property of (4.47) is, that it also holds when not the assembled stiffness and mass matrices of the global tyre structure are used, but the element-specific matrices. This way dissipation can be calculated element-wise, which allows to identify the spatial dissipation distribution over the tyre cross-section.

The rolling losses due to small-scale tread indentation are given by a discrete version of (4.44)

$$P_{\text{tread}} = \frac{1}{T} \sum_{i=0}^I \sum_e c d_{i,e} \left(\frac{\partial d_{i,e}}{\partial t} \right)^2 \Delta t, \quad (4.48)$$

where $T = I\Delta t$.

The rolling resistance coefficient C_r is finally calculated based on the sum of the large-scale tyre and small-scale tread losses, i.e. $P_{\text{diss}} = P_{\text{tyre}} + P_{\text{tread}}$ in Eq. (2.2).

4.6 Additional remarks on the simulation process

4.6.1 Temporal and spatial resolution

For a rolling tyre the temporal and spatial resolutions cannot be arbitrarily chosen. For a rolling speed of V and circumferential resolution of N segments, the time resolution is given as

$$\Delta t = \frac{\Delta x}{V}, \quad (4.49)$$

where $\Delta x = L_{\text{circ}}/N$, with L_{circ} as tyre circumference. Due to $f_s = 1/\Delta t$ also the sampling frequency f_s is given. The frequency resolution is determined by $\Delta f = (n_r N \Delta t)^{-1}$, where n_r is the number of tyre revolutions. L_{circ} and V are determined by the tyre and the operating conditions. This makes it nearly impossible to achieve identical resolutions for two different tyres or speeds. N remains as an option to influence the time and frequency resolution. Yet, the available range for N is also limited due to resolution limitations of the WFE tyre model, resolution requirements of the contact model, and available road roughness input data. Often the only possibility is to adjust n_r .

4.6.2 Conversion between Euler and Lagrange reference system

At several stages during the simulation process quantities are transformed from an Euler to a Lagrange reference system³ and vice versa. This is done by a spatial and temporal reorganisation of the quantity as described in [95, Paper 3]. An example of such a transformation is given in Fig. 4.13 for the case of contact force. Similar transformations are performed for the tyre Green's functions during the contact modelling, and the tyre vibrations which serve as input data for the radiation model.

³See Appendix C.2 for a description of the differences between these two.

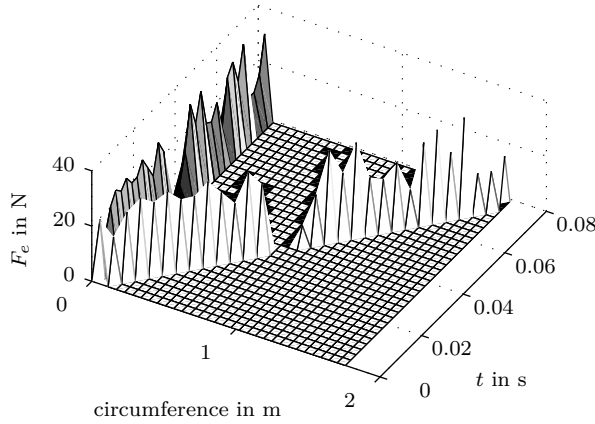


Fig. 4.13 Rearranging a contact force from the Euler to the Lagrange system. In the Euler system the contact force acts at a fixed position on the tyre circumference (grey). In the Lagrange system the force is reorganised to move around the circumference over time (white). Note: The actual spatial and temporal resolution in the simulation is at least 16 times higher than shown here.

4.6.3 Rotational effects

It is undisputed that rotational phenomena like the Doppler shift, centrifugal forces and the Coriolis effect have an influence on the tyre dynamics [52, 132]. This has led to the creation of several tyre models which explicitly include these effects in their system formulations [68, 101, 133]. Despite these efforts, it has not yet been shown that the rotation-induced changes of tyre dynamics actually have a significant influence on sound radiation or rolling losses.

Because of this rotational effects are included in a simplified way in this tyre model. The Doppler shift is, as is shown in [52, 128], already included in the reference system transformation scheme as described in Section 4.6.2. Following an approach proposed in [57], the effect of centrifugal forces is modelled as an increase in pre-tension, see Section 5.4. The influence of the Coriolis effect is not included as it is of minor importance for tyre dynamics [132, 133].

4.6.4 Large-deformation non-linearity

It is a well-known fact that under typical loading conditions tyres exhibit a non-linear behaviour due to large deformations [16]. While the implemented tyre model is capable of capturing the static deformation with the right order of magnitude,

see (c) and (d) in Fig. 4.12, it does not account for the non-linearities caused by these deflections.

The most prominent effect caused by these non-linearities is a softening of the sidewall. In [51] it is shown that for a ring-based tyre model differences in sidewall stiffness between a linear and a non-linear sidewall implementation are around 10% for typical tyre loads. Because the actual sidewall geometry is much more accurately represented in the WFE model than in a ring model, it is assumed that in the case of the present study these differences are smaller. Yet, an underestimation of hub deflection under static load as reported in Section 6.1/*Paper I* might be related to the linear sidewall modelling.

5 Estimation of material properties for the WFE tyre model

As with any other advanced simulation tool, the results obtained by WFE tyre modelling are only as good as the input data they are based on. Here, input data mainly refers to the geometry and material properties of the tyre. While the geometry is relatively straightforward to obtain and only subject to slight variations based on the inflation pressure, determination of material properties is very difficult. A tyre is a geometrically complex, inhomogeneous and highly anisotropic laminated structure consisting of dozens of different materials ranging from rubber to textiles and steel (cf. Fig. 5.1¹). Bulk material properties are subject to changes with tyre age, temperature, or type, strength and frequency of loading. Many material properties are additionally modified during the course of the manufacturing process, with the extent of changes being difficult to quantify and somewhat varying for each single tyre. Further, simulation results are likely to be affected by numerical damping, discretisation effects and similar phenomena which require modification of “real” material parameters as a countermeasure.

The estimation of the tyre material properties for WFE modelling is considered to be a two stage process. Initially, the properties need to be estimated based on available data and external factors. This is followed by a further manual or automatic optimisation of properties, for example with respect to measurements. Although it is assumed that this second step is always necessary, the quality of data provided after the first step is crucial; if it is good, only slight adjustments might be needed, if it is bad finding suitable values in the optimisation process might be very time-consuming or impossible.

The WFEM cross-section representation is usually a simplified version of the real structure, as is shown in Fig. 5.2. This requires the determination of material input data by what could be described as a condensation process, i.e. a procedure which replaces a complex heterogeneous assembly of different materials with an artificial homogeneous material having the combined material properties of the original setup. An example is shown in Fig. 5.2 where a typical liner-ply-rubber sidewall assembly is replaced by one artificial “sidewall” element with unknown

¹A detailed description of the tyre construction including the functions and properties of the different parts is outside the scope of this text. The reader is instead referred to standard tyre textbooks [16] or information available from the manufacturers [134].

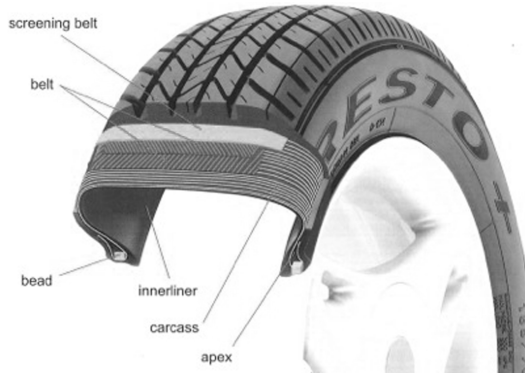


Fig. 5.1 Tyre cross-section with some of the most important functional parts. Note that the *carcass* is also referred to as *ply* in this thesis. Illustration courtesy of Continental Reifen Deutschland GmbH.

material properties. The determination of the condensed properties is generally not easy (as exemplified by [55, 135], where a 3D viscoelastic multilayer model of a tyre belt is used to estimate the input parameters for a bending plate tyre model), and introduces another possible source of error into the simulations.

In the following a condensation technique using input data provided by the tyre manufacturer is described. It is based on a procedure suggested by Altena [136], and includes techniques from shell theory and composite materials analysis [137–139]. The method is demonstrated for the example of a tyre model in which the belt and the sidewall are represented by shell elements as shown in Fig. 5.2. Some variations of the material parameter estimation technique are necessary if the bulk of the tyre is modelled by solid elements instead. This is discussed in Section 5.7.

5.1 Available information

For the demonstration of the condensation approach a 175/65 R14 tyre is used. It has a typical car tyre tread pattern dominated by three circumferential grooves, see Fig. A.1b. The manufacturer provided information about the tyre geometry (including the material sections) and basic material properties. From this, the isotropic bulk properties (i.e. Young’s modulus, Poisson’s ratio and density) are known for all materials. For composite material sections like the belt and ply also the average cord volume fraction and the cord angle are given. Additional information includes the temperature- and frequency-dependency of rubber materials, modal damping coefficients, and the lateral void content ratio for the tread.

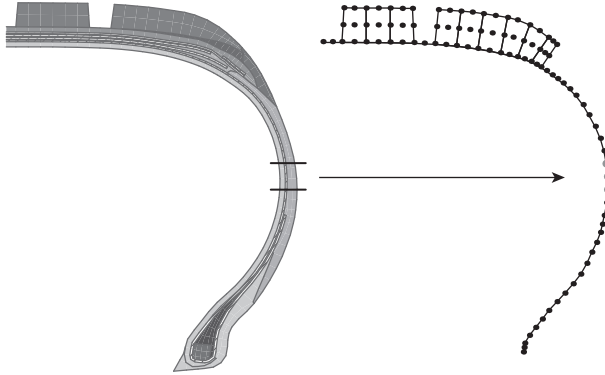


Fig. 5.2 Comparison of a detailed tyre cross-section and a WFEM mesh. The marked sidewall area composed of liner, ply and sidewall material layers is represented by a single shell element (marked grey) in the WFEM mesh.

5.2 Condensation of tyre material properties for shell elements

5.2.1 Stress-strain relations for individual layers

For an anisotropic shell as depicted in Fig. 5.3 the engineering stress-strain relations according to classical Kirchhoff-Love shell theory are given as

$$\begin{bmatrix} \sigma_\xi \\ \sigma_\theta \\ \tau_{\xi\theta} \end{bmatrix} = \begin{bmatrix} Q_{11} & Q_{12} & Q_{16} \\ Q_{12} & Q_{22} & Q_{26} \\ Q_{16} & Q_{26} & Q_{66} \end{bmatrix} \begin{bmatrix} \epsilon_\xi \\ \epsilon_\theta \\ \gamma_{\xi\theta} \end{bmatrix}. \quad (5.1)$$

σ_ξ , σ_θ and ϵ_ξ , ϵ_θ are the in-plane normal stresses and strains, $\tau_{\xi\theta}$ and $\gamma_{\xi\theta}$ denote the in-plane shear stress and strain, and Q_{ij} are the entries of the reduced stiffness matrix connecting stresses and strains. Eq. (5.1) is also valid for any of the individual material layers constituting the tyre laminate.

The determination of the Q_{ij} values is dependent on the material characteristics for the specific layer. Large parts of the tyre, i.e. all rubber material, can be classified as homogeneous and isotropic. Yet, for example the belt and ply, which constitute the core of the tyre, are fibrous composites, i.e. they consist of steel or textile fibres (also called cords) embedded in a rubber matrix. Each of these composite layers is heterogeneous and, depending on the angle between the cords and the tyre coordinate system, either orthotropic or anisotropic. Procedures for obtaining the Q_{ij} for both of the material groups are described in the following.

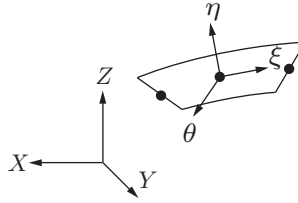


Fig. 5.3 Shell element with curvilinear coordinate system (ξ, η, θ) and global coordinate system (X, Y, Z) . Note: “shell element” refers both to the condensed WFEM shell elements (for which node positions are marked by \bullet) as well as the shell-like individual material layers.

Isotropic layers

For the homogenous and isotropic rubber layers in the tyre, (5.1) reduces to

$$\begin{bmatrix} \sigma_\xi \\ \sigma_\theta \\ \tau_{\xi\theta} \end{bmatrix} = \begin{bmatrix} Q_{11} & Q_{12} & 0 \\ Q_{12} & Q_{22} & 0 \\ 0 & 0 & Q_{66} \end{bmatrix} \begin{bmatrix} \epsilon_\xi \\ \epsilon_\theta \\ \gamma_{\xi\theta} \end{bmatrix}, \quad (5.2)$$

where

$$Q_{11} = Q_{22} = \frac{E}{1 - \nu^2}, \quad Q_{12} = \frac{\nu E}{1 - \nu^2}, \quad Q_{66} = \frac{E}{2(1 + \nu)}. \quad (5.3)$$

E and ν are the material’s Young’s modulus and Poisson’s ratio. Due to the isotropic properties, there is no coupling between in-plane strain and shear, i.e. $Q_{16} = Q_{26} = 0$.

Composite layers

The determination of the stress-strain relations for composite layers as shown in Fig. 5.4 is a multi-step procedure. First, the relationship of the composite’s “apparent” material properties to the cord and matrix properties needs to be established. The two constituting materials in a fibrous composite usually have highly different properties (as exemplified by the combinations of steel or textile cords embedded in a rubber matrix being typical for tyres). Which of them is dominating the composite’s behaviour can vary with direction or type of load. A widely used procedure to determine the properties of the fibrous composite is the *mechanics of materials* approach [139, Cha. 3.2]. It assumes that the constituting materials are homogeneous and isotropic. The properties are calculated in a layer-specific, local coordinate system (cf. Fig. 5.4), where the 1-axis is along the cord direction,

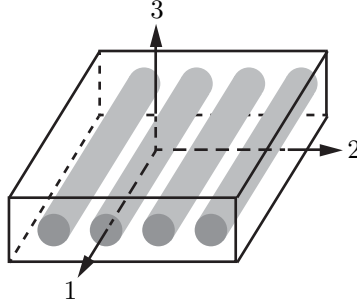


Fig. 5.4 A fibrous composite layer with its local (1, 2, 3)-coordinate system.

the 2-axis is the in-plane normal to the cord direction and the 3-axis is the out-of-plane direction. This establishes the composite layer as an orthotropic material with principal axes coinciding with the (123)-axes. The Young's modulus in the cord direction, E_1 , and the Poisson's ratio ν_{12} can then be directly estimated using the *rule of mixtures*:

$$E_1 = E_c V_{f,c} + E_m V_{f,m} \quad (5.4)$$

$$\nu_{12} = \nu_c V_{f,c} + \nu_m V_{f,m} . \quad (5.5)$$

Herein, E_c (ν_c) and E_m (ν_m) are the Young's moduli (Poisson's ratios) of the cord and the matrix material, and $V_{f,c}$ and $V_{f,m}$ are the volume fraction of the cords respectively the rubber matrix in the composite:

$$V_{f,c} = \frac{vol_c}{vol_c + vol_m} \quad (5.6)$$

$$V_{f,m} = 1 - V_{f,c} , \quad (5.7)$$

where vol_c and vol_m are the volumes of the cords and the matrix.

Several techniques exist for the approximation of the composite's characteristics in the 2-direction. One of these techniques are the *Halpin-Tsai equations* [139]:

$$E_2 = E_m \frac{1 + \zeta \alpha V_{f,c}}{1 - \alpha V_{f,c}} \quad (5.8)$$

$$G_{12} = G_m \frac{1 + \zeta \beta V_{f,c}}{1 - \beta V_{f,c}} , \quad (5.9)$$

where

$$\alpha = \frac{E_c/E_m - 1}{E_c/E_m + \zeta} \quad (5.10)$$

$$\beta = \frac{G_c/G_m - 1}{G_c/G_m + \zeta}. \quad (5.11)$$

G_{12} is the shear modulus in the 12-plane, and G_c and G_m are the isotropic shear stiffnesses of the cord and matrix materials, given as

$$G_i = \frac{E_i}{2(1 + \nu_i)}, \quad \text{for } i = c, m. \quad (5.12)$$

The parameter ζ is a measure of the influence of the fibre reinforcement on the composite material and depends for example on fibre and packing geometry, or boundary conditions. It can either be determined from measurements or be approximated as

$$\zeta = \begin{cases} 2 + 40V_{f,c}^{10}, & \text{for } E_2, \\ 1 + 40V_{f,c}^{10}, & \text{for } G_{12}. \end{cases} \quad (5.13a)$$

Finally, the still missing Poisson's ratio ν_{21} is given by reciprocity as

$$\nu_{21} = \frac{\nu_{12}E_2}{E_1}. \quad (5.14)$$

Using Equations (5.4) to (5.14) an expression for the stress-strain relations of the orthotropic fibrous composite in the local (1, 2, 3)-coordinate system can be obtained as

$$\begin{bmatrix} \sigma_1 \\ \sigma_2 \\ \tau_{12} \end{bmatrix} = \begin{bmatrix} Q_{11} & Q_{12} & 0 \\ Q_{12} & Q_{22} & 0 \\ 0 & 0 & Q_{66} \end{bmatrix} \begin{bmatrix} \epsilon_1 \\ \epsilon_2 \\ \gamma_{12} \end{bmatrix}, \quad (5.15)$$

where

$$Q_{11} = \frac{E_1}{1 - \nu_{12}\nu_{21}} \quad (5.16a)$$

$$Q_{22} = \frac{E_2}{1 - \nu_{12}\nu_{21}} \quad (5.16b)$$

$$Q_{12} = \frac{E_2\nu_{12}}{1 - \nu_{12}\nu_{21}} = \frac{E_1\nu_{21}}{1 - \nu_{12}\nu_{21}} \quad (5.16c)$$

$$Q_{66} = G_{12}. \quad (5.16d)$$

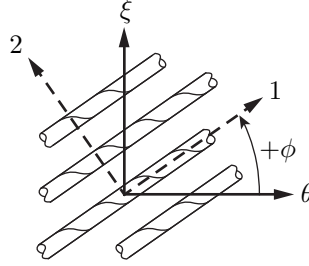


Fig. 5.5 Definition of the rotation direction between the principal material axes of the fibrous composite and the curvilinear WFEM shell coordinates.

Because the local (1, 2, 3)-coordinate system aligns with the material's principal axes of orthogonality, there is — similar to the isotropic case in (5.2) — again no coupling between in-plane strain and shear. For a fibrous composite which is rotated by an angle ϕ with respect to a global coordinate system as shown in Fig. 5.5, the stress-strain relations in the global coordinate system can be obtained by a coordinate transformation procedure (see e.g. [139, Cha. 2]). The final result is

$$\begin{bmatrix} \sigma_\xi \\ \sigma_\theta \\ \tau_{\xi\theta} \end{bmatrix} = \begin{bmatrix} \bar{Q}_{11} & \bar{Q}_{12} & \bar{Q}_{16} \\ \bar{Q}_{12} & \bar{Q}_{22} & \bar{Q}_{26} \\ \bar{Q}_{16} & \bar{Q}_{26} & \bar{Q}_{66} \end{bmatrix} \begin{bmatrix} \epsilon_\xi \\ \epsilon_\theta \\ \gamma_{\xi\theta} \end{bmatrix}, \quad (5.17)$$

where

$$\bar{Q}_{11} = Q_{11} c^4 + 2(Q_{12} + 2Q_{66}) c^2 s^2 + Q_{22} s^4 \quad (5.18a)$$

$$\bar{Q}_{12} = (Q_{11} + Q_{22} - 4Q_{66}) c^2 s^2 + Q_{12}(c^4 + s^4) \quad (5.18b)$$

$$\bar{Q}_{16} = (Q_{11} - Q_{12} - 2Q_{66}) c^3 s + (Q_{12} - Q_{22} + 2Q_{66}) c s^3 \quad (5.18c)$$

$$\bar{Q}_{22} = Q_{11} s^4 + 2(Q_{12} + 2Q_{66}) c^2 s^2 + Q_{22} c^4 \quad (5.18d)$$

$$\bar{Q}_{26} = (Q_{11} - Q_{12} - 2Q_{66}) s^3 c + (Q_{12} - Q_{22} + 2Q_{66}) c^3 s \quad (5.18e)$$

$$\bar{Q}_{66} = (Q_{11} + Q_{22} - 2Q_{12} - 2Q_{66}) c^2 s^2 + Q_{66}(c^4 + s^4) \quad (5.18f)$$

and

$$c = \cos \phi \quad (5.19a)$$

$$s = \sin \phi. \quad (5.19b)$$

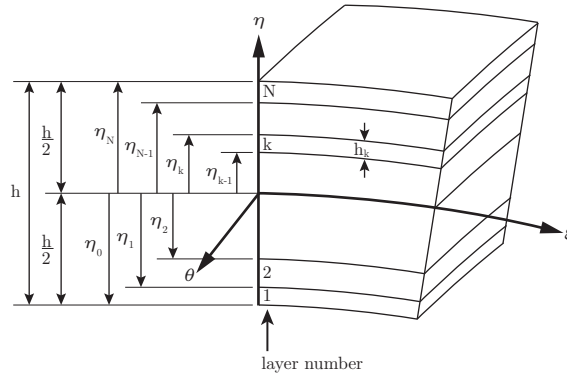


Fig. 5.6 Laminated shell element.

The terms \bar{Q}_{16} and \bar{Q}_{26} vanish for $\phi = n\pi/2$, $n = 0, 1, 2, \dots$, implying that the composite is orthotropic with respect to the global coordinate system. For all other ϕ the composite is anisotropic with coupling of in-plane stress and shear. This is for example the case for the nowadays almost exclusively used radial tyres, where the placing of the steel cords in the belt at a certain diagonal angle to the tread centreline is a crucial design property to increase strength and stability. As a consequence, the fibrous belt composite is anisotropic with regards to the tyre coordinate system. Then again, the ply cords are laid at 90° to the centreline, implying that the ply composite remains orthotropic².

5.2.2 Force and moment resultants for laminates

With Equations (5.2) and (5.17) the stress-strain relations for individual isotropic or composite material layers have been determined. However, many elements used in the WFE analysis are laminates consisting of multiple layers of different material groups, as is exemplified in Figures 5.2 and 5.6. The combined macromechanical behaviour of such a laminate can be expressed using *classical lamination theory*. In this theory, the complex, three-dimensional elasticity problem involving the whole laminate domain is reduced to expressions for the resulting laminate middle-surface membrane strains and bending curvatures. Presuming that the resulting shell obeys classical Kirchhoff-Love theory, there is only a linear variation of strain across the shell thickness, i.e.

²For the less common diagonal bias and belted bias tyre types the ply cords are also laid diagonally to the centreline, giving them anisotropic material behaviour with respect to the tyre coordinate system.

$$\begin{bmatrix} \epsilon_\xi \\ \epsilon_\theta \\ \gamma_{\xi\theta} \end{bmatrix} = \begin{bmatrix} \epsilon_\xi^0 \\ \epsilon_\theta^0 \\ \gamma_{\xi\theta}^0 \end{bmatrix} + \eta \begin{bmatrix} \kappa_\xi \\ \kappa_\theta \\ \kappa_{\xi\theta} \end{bmatrix}, \quad (5.20)$$

where $[\epsilon_\xi^0 \ \epsilon_\theta^0 \ \gamma_{\xi\theta}^0]^T$ denote the strains at the shell middle-surface and $[\kappa_\xi \ \kappa_\theta \ \kappa_{\xi\theta}]^T$ the middle-surface curvatures. By inserting (5.20) in (5.2) or (5.17) the stresses in the k th layer can be related to the shell middle-surface strains and curvatures as

$$\begin{bmatrix} \sigma_\xi \\ \sigma_\theta \\ \tau_{\xi\theta} \end{bmatrix}_k = \begin{bmatrix} \bar{Q}_{11} & \bar{Q}_{12} & \bar{Q}_{16} \\ \bar{Q}_{12} & \bar{Q}_{22} & \bar{Q}_{26} \\ \bar{Q}_{16} & \bar{Q}_{26} & \bar{Q}_{66} \end{bmatrix}_k \cdot \left[\begin{bmatrix} \epsilon_\xi^0 \\ \epsilon_\theta^0 \\ \gamma_{\xi\theta}^0 \end{bmatrix} + \eta \begin{bmatrix} \kappa_\xi \\ \kappa_\theta \\ \kappa_{\xi\theta} \end{bmatrix} \right]. \quad (5.21)$$

The resultant normal forces per unit width, N , and moments per unit width, M , which act on the shell middle-surface, can be obtained by summing up the integrals of the layer stresses over the layer thicknesses as follows

$$\begin{bmatrix} N_\xi \\ N_\theta \\ N_{\xi\theta} \end{bmatrix} = \int_{-h/2}^{h/2} \begin{bmatrix} \sigma_\xi \\ \sigma_\theta \\ \tau_{\xi\theta} \end{bmatrix} d\eta = \sum_{k=1}^N \int_{\eta_{k-1}}^{\eta_k} \begin{bmatrix} \sigma_\xi \\ \sigma_\theta \\ \tau_{\xi\theta} \end{bmatrix}_k d\eta \quad (5.22)$$

and

$$\begin{bmatrix} M_\xi \\ M_\theta \\ M_{\xi\theta} \end{bmatrix} = \int_{-h/2}^{h/2} \begin{bmatrix} \sigma_\xi \\ \sigma_\theta \\ \tau_{\xi\theta} \end{bmatrix} \eta d\eta = \sum_{k=1}^N \int_{\eta_{k-1}}^{\eta_k} \begin{bmatrix} \sigma_\xi \\ \sigma_\theta \\ \tau_{\xi\theta} \end{bmatrix}_k \eta d\eta. \quad (5.23)$$

Herein, h is the thickness of the laminate shell and the η_k denote the directed distance from the middle-surface to the top of the k th layer as shown in Fig. 5.6. For the thickness of a layer it is thus $h_k = \eta_k - \eta_{k-1}$. By inserting (5.21) into (5.22) and (5.23), and using the fact that the $(\bar{Q}_{ij})_k$ are constant within a layer, the forces and moments can be written in a combined matrix form as (see [139, Cha. 4] for details)

$$\begin{bmatrix} \hat{N} \\ \hat{M} \end{bmatrix} = \begin{bmatrix} \mathbf{P} & \mathbf{PQ} \\ \mathbf{PQ} & \mathbf{Q} \end{bmatrix} \begin{bmatrix} \boldsymbol{\epsilon} \\ \boldsymbol{\kappa} \end{bmatrix} \quad (5.24)$$

where

$$\hat{\mathbf{N}} = [N_\xi \quad N_\theta \quad N_{\xi\theta}]^T \quad (5.25a)$$

$$\hat{\mathbf{M}} = [M_\xi \quad M_\theta \quad M_{\xi\theta}]^T \quad (5.25b)$$

$$\boldsymbol{\epsilon} = [\epsilon_\xi^0 \quad \epsilon_\theta^0 \quad \gamma_{\xi\theta}^0]^T \quad (5.25c)$$

$$\boldsymbol{\kappa} = [\kappa_\xi \quad \kappa_\theta \quad \tau_{\xi\theta}]^T \quad (5.25d)$$

and

$$\mathbf{P} = \begin{bmatrix} P_{11} & P_{12} & P_{16} \\ P_{12} & P_{22} & P_{26} \\ P_{16} & P_{26} & P_{66} \end{bmatrix} \quad (5.26a)$$

$$\mathbf{PQ} = \begin{bmatrix} PQ_{11} & PQ_{12} & PQ_{16} \\ PQ_{12} & PQ_{22} & PQ_{26} \\ PQ_{16} & PQ_{26} & PQ_{66} \end{bmatrix} \quad (5.26b)$$

$$\mathbf{Q} = \begin{bmatrix} Q_{11} & Q_{12} & Q_{16} \\ Q_{12} & Q_{22} & Q_{26} \\ Q_{16} & Q_{26} & Q_{66} \end{bmatrix} \quad (5.26c)$$

with

$$P_{ij} = \sum_{k=1}^N (\bar{Q}_{ij})_k (\eta_k - \eta_{k-1}) \quad (5.27a)$$

$$PQ_{ij} = \frac{1}{2} \sum_{k=1}^N (\bar{Q}_{ij})_k (\eta_k^2 - \eta_{k-1}^2) \quad (5.27b)$$

$$Q_{ij} = \frac{1}{3} \sum_{k=1}^N (\bar{Q}_{ij})_k (\eta_k^3 - \eta_{k-1}^3). \quad (5.27c)$$

Herein, \mathbf{P} and \mathbf{Q} are extensional and bending stiffness matrices while \mathbf{PQ} is a stiffness matrix coupling normal forces with bending curvatures (and vice-versa, bending moments with in-plane strains). For a laminate, \mathbf{PQ} vanishes only under very special conditions. For many other examples often the assumption is made that extension and bending are independent of each other. This does not hold at large in this case.

5.2.3 Transverse shear

No assumptions have so far been made about the transverse shear across the element thickness. In a manner similar to (5.24) it can be expressed in terms of resultant middle-surface transverse forces as

$$\hat{\mathbf{T}} = \mathbf{G}\boldsymbol{\gamma} \quad (5.28)$$

where

$$\hat{\mathbf{T}} = [T_{\xi\eta} \quad T_{\theta\eta}]^T \quad (5.29a)$$

$$\boldsymbol{\gamma} = [\gamma_{\xi\eta} \quad \gamma_{\theta\eta}]^T \quad (5.29b)$$

and

$$\mathbf{G} = \begin{bmatrix} G_{11} & G_{12} \\ G_{12} & G_{22} \end{bmatrix}. \quad (5.30)$$

As a first simplification it is assumed that there is no coupling between shear in the ξ and θ directions, i.e. $G_{12} = 0$. In [140] a deep shell approximation for the remaining terms is given as

$$G_{11} = \frac{1}{4}(P_{11} + 2P_{66}) \quad (5.31a)$$

$$G_{22} = \frac{1}{4}(P_{22} + 2P_{66}). \quad (5.31b)$$

5.2.4 Determination of the elastic stiffness matrix for a shell element

Combining (5.24) with (5.28) all resulting forces and moments for the laminate are obtained as

$$\begin{bmatrix} \hat{\mathbf{N}} \\ \hat{\mathbf{M}} \\ \hat{\mathbf{T}} \end{bmatrix} = \begin{bmatrix} \mathbf{P} & \mathbf{PQ} & \mathbf{0} \\ \mathbf{PQ} & \mathbf{Q} & \mathbf{0} \\ \mathbf{0} & \mathbf{0} & \mathbf{G} \end{bmatrix} \begin{bmatrix} \boldsymbol{\epsilon} \\ \boldsymbol{\kappa} \\ \boldsymbol{\gamma} \end{bmatrix}, \quad (5.32)$$

where $\mathbf{0}$ are zero matrices of appropriate size. By comparison of (5.32) with the formulation of the WFEM shell element given in [72], the elastic stiffness matrix $\mathbf{D}_{\text{shell}}$ of the shell element can be identified as

$$\mathbf{D}_{\text{shell}} = \begin{bmatrix} \mathbf{P} & \mathbf{PQ} & \mathbf{0} \\ \mathbf{PQ} & \mathbf{Q} & \mathbf{0} \\ \mathbf{0} & \mathbf{0} & \mathbf{G} \end{bmatrix}. \quad (5.33)$$

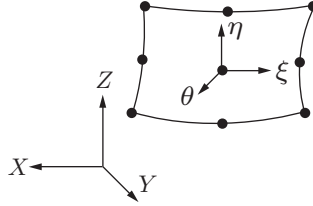


Fig. 5.7 Solid element with curvilinear coordinate system (ξ, η, θ) and global coordinate system (X, Y, Z) . Node positions marked by \bullet .

5.3 Stiffness parameters for isotropic solid elements

If only the tread consisting of one layer of homogeneous, isotropic rubber material is modelled with solid elements the determination of the elastic stiffness matrix \mathbf{D}_{sol} is straightforward. \mathbf{D}_{sol} follows from the engineering stress-strain relations for isotropic solids [141, Cha. 2]

$$\boldsymbol{\sigma}_{\text{sol}} = \mathbf{D}_{\text{sol}} \boldsymbol{\epsilon}_{\text{sol}} \quad (5.34)$$

as

$$\mathbf{D}_{\text{sol}} = \frac{E}{(1+\nu)(1-2\nu)} \begin{bmatrix} 1-\nu & \nu & \nu & 0 & 0 & 0 \\ \nu & 1-\nu & \nu & 0 & 0 & 0 \\ \nu & \nu & 1-\nu & 0 & 0 & 0 \\ 0 & 0 & 0 & \frac{1-2\nu}{2} & 0 & 0 \\ 0 & 0 & 0 & 0 & \frac{1-2\nu}{2} & 0 \\ 0 & 0 & 0 & 0 & 0 & \frac{1-2\nu}{2} \end{bmatrix}, \quad (5.35)$$

The stress and strain vectors in (5.34) are defined as

$$\boldsymbol{\sigma}_{\text{sol}} = [\sigma_{\xi} \quad \sigma_{\eta} \quad \sigma_{\theta} \quad \tau_{\xi\eta} \quad \tau_{\xi\theta} \quad \tau_{\eta\theta}]^T \quad (5.36a)$$

$$\boldsymbol{\epsilon}_{\text{sol}} = [\epsilon_{\xi} \quad \epsilon_{\eta} \quad \epsilon_{\theta} \quad \gamma_{\xi\eta} \quad \gamma_{\xi\theta} \quad \gamma_{\eta\theta}]^T. \quad (5.36b)$$

Herein, the extensional stresses and strains are given by the σ_i and ϵ_i , the τ_{ij} and γ_{ij} are the shear stresses and strains, and the coordinate system is defined by Fig. 5.7.

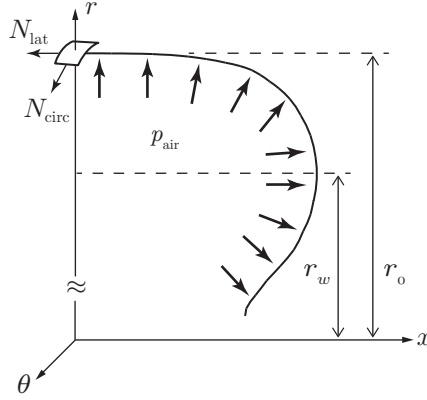


Fig. 5.8 Tyre cross-section geometry for pre-tension calculations.

5.4 Pre-tension

The pre-tension of the ply and belt cords caused by the manufacturing process and the inflation pressure considerably influences the dynamic behaviour of the tyre. As it is extremely difficult to measure pre-tension in the cured tyre, usually no useful pre-tension data can be provided by the tyre manufacturer. Estimations of the pre-tension in lateral and circumferential direction are possible by treating the tyre as a doubly curved membrane surface as shown in Fig. 5.8. Force equilibrium considerations [16, Cha. 6]³ then give the lateral and circumferential pre-tensions for the tread centreline as

$$N_{\text{lat}} = \frac{p_{\text{air}}}{2r_0} (r_0^2 - r_w^2) \quad (5.37)$$

$$N_{\text{circ}} = R_{\theta} \left(p_{\text{air}} - \frac{N_{\text{lat}}}{R_{\xi}} \right). \quad (5.38)$$

p_{air} is the air pressure in the tyre cavity, r_0 the radius at the tyre centreline and r_w the radius at the widest point of the tyre cross-section. The radii of curvature in lateral and circumferential direction, R_{ξ} and R_{θ} , are given as

$$R_{\xi} = \left| r \frac{(1 + x'^2)^{\frac{1}{2}}}{x'} \right| \quad (5.39a)$$

³Note the typo in the original formulation of (5.38) in [16].

and

$$R_\theta = \left| \frac{(1 + x'^2)^{\frac{3}{2}}}{x''} \right|, \quad (5.39b)$$

with

$$x' = \frac{dx}{dr}, \quad x'' = \frac{d^2x}{dr^2}. \quad (5.40)$$

As the ply cords run perpendicular to the tread centreline they cannot support circumferential pre-tension. Hence, N_{circ} is only non-zero for the shoulder and crown areas of the tyre containing belt cords. It seems reasonable to estimate the variation in N_{circ} for these areas by varying x and r in (5.39). The determination of values for N_{lat} outside the tread centreline is not as straightforward, especially for the sidewall areas of the tyre [16]. In [42, Paper B] an estimation of the lateral pre-tension at a point (x, r) on the tyre cross-section is given as

$$N_{\text{lat}}(x, r) = N_{\text{lat}} \frac{r_0}{r}. \quad (5.41)$$

Owing to the lack of better alternatives, this is taken as a basis for estimation of the lateral pre-tension distribution.

Equations (5.37) and (5.38) are based on static equilibrium considerations, for a rotating tyre there is an additional contribution from the centrifugal force to the circumferential pre-tension which is given as [57]

$$N_{\text{circ}, \Omega} = \mu \Omega^2 r_0^2. \quad (5.42)$$

Herein, Ω is the angular velocity of the tyre and μ is the belt's mass per unit area. The effective circumferential pre-tension is finally given by the sum of N_{circ} and $N_{\text{circ}, \Omega}$.

5.5 Viscoelastic material properties

The dynamic properties of rubber depend strongly on the temperature and the frequency of oscillation [16]. An example of this is given in Fig. 5.9 where the relation between the frequency-dependent dynamic Young's modulus $E_{\text{dyn}}(f)$ and the static Young's modulus E_{stat} , i.e. the one for $f = 0$ Hz, is shown for temperatures of 20°C and 55°C. These are typical temperatures for mobility measurements and real rolling conditions. Similar relations can be observed for the loss factor.

For two of the three tyres used in the simulations dynamic Young's moduli are available from the manufacturer for 20°C and 55°C. As mobility measurements

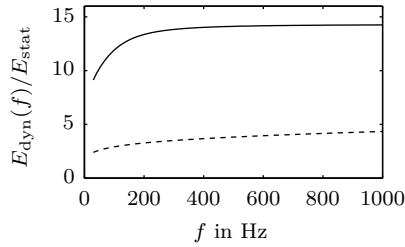


Fig. 5.9 Example of the frequency dependency of the Young's modulus of a rubber material for 20°C (—) and 55°C (---). No data available below 30 Hz, but it is $E_{\text{dyn}}(0 \text{ Hz})/E_{\text{stat}} = 1$.

are not feasible for 55°C, it is not possible to validate the condensation results or the obtain loss factor data for this temperature. Because of this material values for 20°C are taken as basis for all simulations. In most cases the frequency dependency of the Young's moduli is ignored, instead the values at 200 Hz are taken for all frequencies. The exception are the studies presented in Sections 6.4 and 6.5, i.e. *Papers IV* and *V*. For these the Young's moduli for the rubber materials are, slightly simplified, assumed to be frequency dependent below 200 Hz. For higher frequencies constant values are used.

Theoretically, the damping properties of individual elements in the WFE model can be determined in a similar way as the element stiffness in Section 5.2 if adequate damping data for the constituting material groups is available. This leads almost certainly to non-proportional damping. If this is not wanted or if no input data is provided, damping properties can be based on measurements instead. Low- to mid-frequency loss factors can for example be obtained from half-power bandwidth evaluations of the first few resonance peaks in a measured input mobility, or from modal damping measurements.

5.6 Additional implementation considerations

The WFEM mesh is directly based on the tyre geometry as provided by the manufacturer. For a mainly shell-based model the shell elements are as far as reasonable placed in accordance with the neutral layer of the laminate they correspond to.

Because the shell elements have no geometric extension in the η -direction (the thickness is a material property for shells), the geometry of the solid elements modelling the tread layer has to be adjusted to keep shell and solid elements connected in the WFE model. In order to change to size of the solid elements as little as possible, the tread layer is moved down half the shell element thickness.

Circumferential grooves are modelled by removal of solid elements from the tread layer if necessary. An example of this is shown in Fig. A.3. Lateral tread voids are included as outlined in Section 4.3.

The material data derived by the condensation procedure gives good initial match between simulated and measured mobilities, see e.g. [142, Appendix C]. The agreement can be further improved by adjustment of the material parameters, either manually or by using an optimisation procedure such as the genetic algorithm described in [142, Appendix B].

5.7 Modifications for solid element based tyre models

So far, the estimation of material input data has been discussed for a WFE tyre model in which the majority of the structure is modelled by shell elements and solid elements are only used for the tread rubber.

A better representation of the tyre geometry, especially for truck tyres, is achieved by modelling the bulk of the tyre structure using solid elements instead, for example as shown in Fig. A.5. This also reduces the need to determine material parameters for elements encompassing several material groups. A drawback is the higher numerical effort due to the increased number of degrees-of-freedom.

The solids are no longer restricted to pure rubber regions in such a model. Instead, they consist of mixtures of steel cords and rubber in the belt and apex regions. Accordingly, as a first step the solids have to allow for orthotropic material behaviour. \mathbf{D}_{sol} in (5.34) changes to [139]

$$\mathbf{D}_{\text{sol}} = \begin{bmatrix} D_{11} & D_{12} & D_{13} & 0 & 0 & 0 \\ D_{12} & D_{22} & D_{23} & 0 & 0 & 0 \\ D_{13} & D_{23} & D_{33} & 0 & 0 & 0 \\ 0 & 0 & 0 & D_{44} & 0 & 0 \\ 0 & 0 & 0 & 0 & D_{55} & 0 \\ 0 & 0 & 0 & 0 & 0 & D_{66} \end{bmatrix}, \quad (5.43)$$

where the (1, 2, 3)-coordinate system aligns with the material's principal axes of orthogonality, and

$$\begin{aligned} D_{11} &= \frac{1 - \nu_{23}\nu_{32}}{E_2 E_3 \Lambda}, & D_{22} &= \frac{1 - \nu_{13}\nu_{31}}{E_1 E_3 \Lambda}, & D_{33} &= \frac{1 - \nu_{12}\nu_{21}}{E_1 E_2 \Lambda}, \\ D_{12} &= \frac{\nu_{12} + \nu_{32}\nu_{13}}{E_1 E_3 \Lambda}, & D_{23} &= \frac{\nu_{23} + \nu_{21}\nu_{12}}{E_1 E_2 \Lambda}, & D_{13} &= \frac{\nu_{13} + \nu_{12}\nu_{23}}{E_1 E_2 \Lambda}, \\ D_{44} &= \frac{E_1}{2(1 + \nu_{12})} = G_{12}, & D_{55} &= \frac{E_3}{2(1 + \nu_{31})} = G_{13}, & D_{66} &= \frac{E_2}{2(1 + \nu_{23})} = G_{23}, \end{aligned}$$

with

$$\Lambda = \frac{1 - \nu_{21}\nu_{12} - \nu_{23}\nu_{32} - \nu_{13}\nu_{31} - 2\nu_{21}\nu_{32}\nu_{13}}{E_1 E_2 E_3}.$$

Material properties in the (ξ, η, θ) -element coordinate system are again given by the transformation equations (5.18) if no rotation of the 3-axis is necessary. Properties for fibrous composite layers are given by an extension of the *Halpin-Tsai* approach for the 3-direction which has not been considered in Section 5.2.1. E_3 , ν_{13} , ν_{31} , G_{31} , and ν_{32} are obtained in similar ways as is done for the 2-direction. G_{23} is given by Equations (5.9) and (5.11) where ζ is replaced by $\zeta_{G_{23}} = (4 - 3\nu_m)^{-1}$, see [138]. Finally, [139] gives ν_{23} as

$$\nu_{23} = \nu_m \frac{1 + \zeta_{G_{23}} \gamma V_{f,c}}{1 - \gamma V_{f,c}} \quad (5.44)$$

$$\gamma = \frac{\nu_c/\nu_m - 1}{\nu_c/\nu_m + \zeta_{G_{23}}}. \quad (5.45)$$

Properties for solid elements consisting of several different material layers, e.g. in the belt region, are obtained using the *rule of mixtures*.

The number of solid elements with more than one material group can be significantly reduced by continuing to model the ply using shell elements. This also avoids the need to introduce a pre-tension term into the element formulation for the solids.

6 Application examples

In the following some application examples of the presented tyre/road noise and rolling resistance model are given. All examples constitute condensed versions of the findings of *Papers I* and *V*.

Specific details about the tyre models used in each of the examples can be found in Appendix A. Further simulation parameters are listed in Appendix B.

6.1 A comparison of FEM and WFEM for the simulation of tyre/road interaction

This is a condensed version of Paper I.

The WFE method presented in this work is intended to be used for the simulation of rolling noise and rolling resistance. An important aspect for these applications is an accurate description of the road induced excitation: both the high frequency vibration field and quasi-static contact area need to be captured accurately. In this work FE and WFE models of a 175/65 R14 tyre are compared in terms of traditional NVH properties such as mobility and modal frequencies, and in term of contact behaviour such as footprint shape and structural stiffness. This way the potential of the WFE method for the modelling of both the excitation and the response of a rolling tyre is critically examined.

6.1.1 The finite element tyre model

The FE representation of the tyre is based on a software developed and used by Continental AG. A 3D model composed of 100 circumferential sections is used. The rubber components of the tyre are modelled with brick elements using a hyper-elastic material law. A composite formulation is used for the construction zones with cord reinforcement. The inflated-loaded tyre equilibrium for the comparison of the footprint size and the load-deflection curve is calculated with a nonlinear algorithm which takes the stress induced by the 200 kPa inflation pressure into account. The eigenanalysis is performed under consideration of the temperature and frequency dependency of the viscoelastic properties. Forced response is calculated using a modal summation approach.

6.1.2 Input data

The tyre geometry (including the material sections) and bulk material properties are known and shared between both models. Due to the simplified nature of the cross-sectional mesh used in the WFE simulations, a condensation procedure as described in Chapter 5 and further property optimisation with respect to measured radial mobilities is necessary (see [142] for details). In the FE model, the different material groups are modelled individually and no further material optimisation is performed. In both tyre models viscoelastic properties for 20°C and 200 Hz are used. The WFE model's original purpose is to simulate tyre vibrations due to tyre/road interaction, meaning that both contact deformation and dynamic response are determined simultaneously. Accordingly, in the present study viscoelastic properties are used for both the quasi-static and the dynamic WFE simulations. In the case of FEM, the standard procedure of considering viscoelasticity only for the dynamic simulations is followed. A common proportional damping model using a frequency depending loss-factor is incorporated in both models.

6.1.3 Quasi-static simulations

In Fig. 6.1 the predicted tyre footprint sizes for both methods are compared to each other for five different tyre loads. For a load of 3000 N both methods give approximately the same footprint size. For lower loads, WFEM overestimates the footprint area in comparison to the FEM results, with a maximum area deviation of 44 % for 1000 N. In contrast, for higher loads WFEM underestimates the area, at most with 24 % at 5000 N. All variations in area are mostly due to differences in the circumferential direction; the footprint size in lateral direction matches well between both methods apart from the case of 1000 N load.

Considerably bigger differences between FE and WFE simulations are visible in the load-deflection curves plotted in Fig. 6.2. While both curves exhibit the expected slight non-linearity [16], for any given load the deflection in the FE

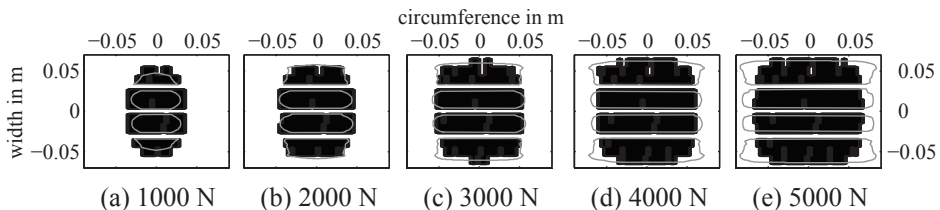


Fig. 6.1 Size of footprint area for different tyre loads for FE (—) and WFE simulations (solid black area).

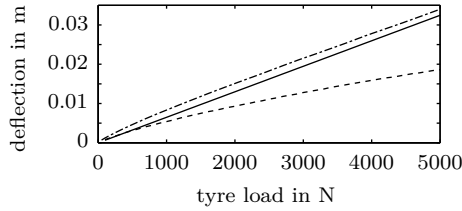


Fig. 6.2 Load-deflection curves for FE (---), and WFE simulations (-·-) and Eq. (6.1) (—).

model is always considerably higher than that in the WFE model. The differences between the two models rise from 56 % at 1000 N to 82 % at 5000 N. Also plotted in Fig. 6.2 is an empirical linear load-deflection approximation (see [16]) given as

$$d = L \cdot (0.00028P\sqrt{(-0.004AR + 1.03)S_N(S_N AR/50 + D_R)} + 3.45)^{-1}, \quad (6.1)$$

where d is the deflection, L the load in kg, P the inflation pressure in kPa, AR and S_N are the aspect ratio and nominal section width as printed on the tyre, and D_R is the rim diameter in mm. The FE results are roughly of the same order as these approximation results.

6.1.4 Dynamic simulations

In Fig. 6.3a the results of FE and WFE eigenfrequency analyses are compared to measured eigenfrequencies. With the sole exception of the last eigenmode, the FE predictions are always within 10 % of the measured frequencies. The highest differences generally occur for asymmetric mode shapes. The average deviation over all modes is 4.2 %. The WFEM simulations exhibit considerable variations of more than 20 % from the measured eigenfrequencies for asymmetric modes of circumferential orders zero to two. For the symmetric modes of orders zero and nine, deviations are more than 10 %. All other eigenfrequencies are predicted with less than 10 % error, with an average of 9.5 %. Contrary to the FE results, there is no clear difference in accuracy between predictions of symmetric and asymmetric modes.

Measured and simulated mobilities for two circumferential angles and positions on the tyre sidewall and near the tread centre line are given in Fig. 6.4. In the measurements the rim is not fixed as in the simulations, but freely suspended. Due to this all simulated mobilities have an additional low frequency resonance which is not visible in the measurements. This peak is caused by the symmetric mode of order one, see Fig. 6.3b. Starting with the input mobility in Fig. 6.4a, it

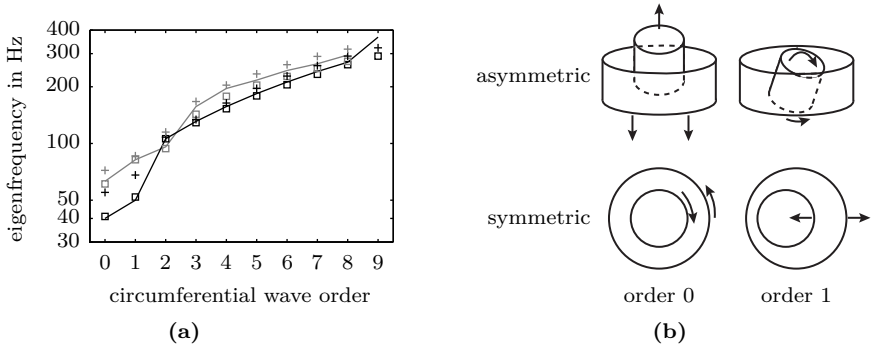


Fig. 6.3 (a) Comparison of eigenfrequencies obtained from measurements (—), FEM (\square) and WFEM (+). Eigenfrequencies for symmetric modeshapes in black, for asymmetric in grey. (b) Principle shape of the first four eigenmodes.

can be observed that the WFEM results match better with the measured mobility in the frequency range from 100 Hz to roughly 260 Hz than the FEM simulations do. Between 260 Hz and 500 Hz neither simulation result is particularly good. However, in contrast to the WFEM results, FE results at least exhibit a similar shape compared to the measurements. Above 500 Hz WFEM again seems to be slightly closer to the measured mobility amplitudes than FEM is.

Fig. 6.4b shows the transfer mobility for a receiving position on the tread centre line at an circumferential angle of 180° to the excitation. Similar tendencies as for the input mobility are visible with WFEM performing better than FEM below 260 Hz and above 500 Hz. For intermediate frequencies both methods show some deviations from the measured mobility. Yet, general tendencies are still captured equally well by both methods. The transfer mobility for a position at the tyre sidewall and a circumferential angle of 0° is shown in Fig. 6.4c. Though the first two measured resonances are better approximated by WFEM, both methods are having equal difficulties to correctly determine resonance frequencies and amplitudes up to 300 Hz. Yet, for frequencies between 120 Hz and 450 Hz the WFEM prediction is closer to the measured mobility than the FEM result. For higher frequencies only FEM is capable of capturing the general features and amplitude levels of the measured mobility. Finally, for a sidewall position at 180° (Fig. 6.4d) WFEM is again better for lower frequencies up to 180 Hz. For higher frequencies both methods struggle somewhat to accurately predict the measured mobility in detail.

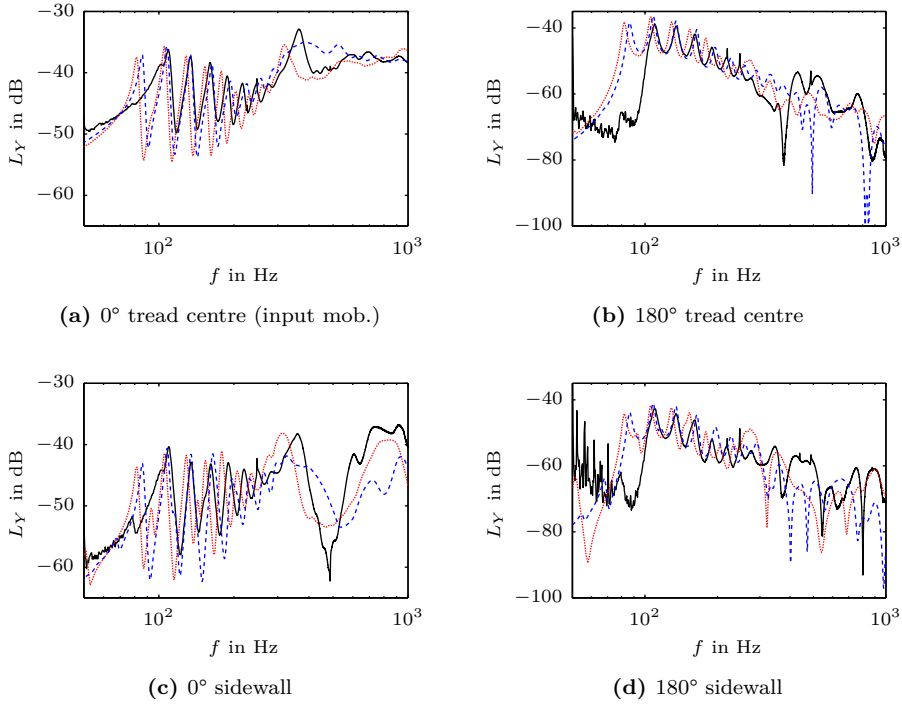


Fig. 6.4 Comparison of mobilities from measurement (—), WFE (---), and FE simulations (· · ·), with $L_Y = 20 \log_{10}(|Y/Y_0|)$, $Y_0 = 1 \text{ N}/(\text{ms})$.

6.1.5 Concluding remarks

Looking at the quasi-static simulations, three major observations can be made: Firstly, the WFE footprint predictions are remarkably good for a dynamic model which is not optimised for static calculations. Secondly, and this is linked to the previous observation, the influence of the contact spring stiffness k on the contact force Eq. (4.29a) has to be taken into account in the footprint analysis. This stiffness is load-dependent; yet, in the present study a constant value derived for a load of 2820 N is used. This partly explains the good match for the load of 3000 N and the over- and underestimations for lower respectively higher loads. Thirdly, in contrast to the footprint analysis, there are major differences in the load-deflection analysis between the WFE results on the one hand and the FE and empirical approximation results on the other hand. This is seen as an indication that the stiffness of the tyre's sidewall in the WFE model is too high. Indeed, the

FE model can capture the non-linear softening of the sidewall membrane under loading. This is not possible in WFEM as the sidewall is modelled according to its inflated geometry. Additionally, there might be problems with modelling the entire sidewall thickness by one layer of shell elements, for example in terms of material parameter estimation or element stiffness.

An important observation for the dynamic analysis is the fact that the measurement results for the eigenfrequency analysis and the mobility measurements show some discrepancies. This can be expected for a viscoelastic structure. Free and forced response measurements correspond to different strain conditions for the rubber components of the tyre, resulting in different dynamic stiffness properties. The extent of the observed discrepancies depends on the participation of the rubber stiffness in each of the modes. Both eigenmodes of the zeroth order and the asymmetric mode of order one are not visible in the measured mobilities, cf. Fig. 6.3b. Hence, they are not accounted for in the WFE material optimisation process. This is unfortunate because all of these modes are mainly dependent on sidewall stiffness (and partly pre-tension). A possible incorrect sidewall modelling in WFE is also indicated in the mobility plots in Fig. 6.4. This may be taken as an indication of the complexity of the model property update process, given that the influence of complete construction zones can be dominant in one test and completely absent in another.

In view of an optimisation of material properties with regards to mobilities ranging up to 1 kHz, it is also rather unfortunate to use 200 Hz as reference frequency for the viscoelastic properties. For many frequencies initial material values are too soft; yet this was a conscious choice given the requirement to include contact deformation calculation in WFEM. By accounting for this in the optimisation process, the WFE tyre model becomes overly stiff for frequencies considerably lower than 200 Hz. This is visible in the semi-rigid body modes and the quasi-static calculations. Though the FE model is also based on material values for 200 Hz, it does not exhibit the same problems as the WFE model. This can be partly explained by the fact that no further adjustment of material parameters is done which could lead to a stiffening of the model. The effect of this can be seen in the high-frequency regions of the mobilities on the tread centre line which are slightly worse than those predicted by WFEM. Another difference between the models is that the geometry and the different material groups are included in detail in the FE model, whereas geometric simplifications and material condensation are used in the WFE model.

In summary, the presented WFE tyre model generally seems to be capable of producing results of the same quality as the FE tyre model does. However, it seems that the WFE model needs more optimising for the particular task than FEM, where the same basic model gives good results for quasi-static and dynamic simulations depending only on whether viscoelasticity is included or not.

6.2 The influence of lateral road surface resolution on rolling loss/noise simulations

This is a condensed version of Paper II. Main difference is the omission of results for the 205/55 R16 tyre.

The accurate description of the tyre/road interaction under rolling conditions is crucial for the simulation of rolling resistance and rolling noise. Besides an accurate contact model, input data of sufficiently high quality is required. Accordingly, the measurement effort for the road roughness profiles is high: in the rolling direction distances of several meters need to be scanned at positions less than a millimetre apart. While in the lateral direction a lower resolution can be accepted, still between ten and twenty parallel profile tracks are required under perfect conditions. Yet, in reality road surface scans are typically restricted to very few lateral tracks due to limited resources. The present study evaluates how rolling resistance and rolling noise simulations are affected if the number of independent lateral road scans is less than the number of lateral tracks in the contact model.

6.2.1 Road properties

The considered road surface profiles are based on detailed laser scans of the following road surfaces:

- (A) Drum-mounted ISO 10844 [143] road replica surface,
- (B) drum-mounted generic rough road surface,
- (C) ISO 10844 [143] road surface,
- (D) 0/8 stone mastic asphalt (SMA), and
- (E) 5/8 surface dressing.

For the surfaces A and B scans of 15 lateral tracks with a length of nine tyre revolutions exist. For surfaces C to E 20 lateral tracks of length 2.95 m and a lateral spacing of 0.01 m are available. The resolution in rolling direction is 0.2 mm for all road surfaces. Due to the limited data in lateral direction, detailed analysis of the surfaces is only possible in the rolling direction. Assumptions about the properties in lateral direction can only be made based on differences or similarities between parallel tracks. The lateral profile average for the first meter of all scans is shown in Fig. 6.5. The highest amplitudes are as expected recorded for the generic rough (B) and surface dressing (E) surfaces. The smoothest surface is the ISO surface (C). The drum mounted surfaces A and B are both characterised by a pronounced unevenness.

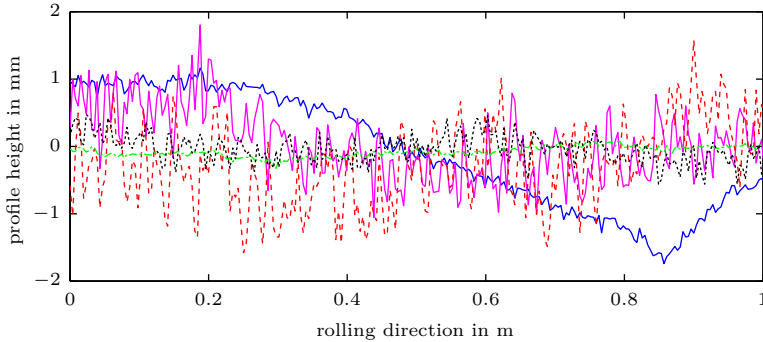


Fig. 6.5 Average of the road surface profile over all lateral tracks for the first meter in rolling direction. A (—), B (---), C (-·-·), D (···) and E (—).

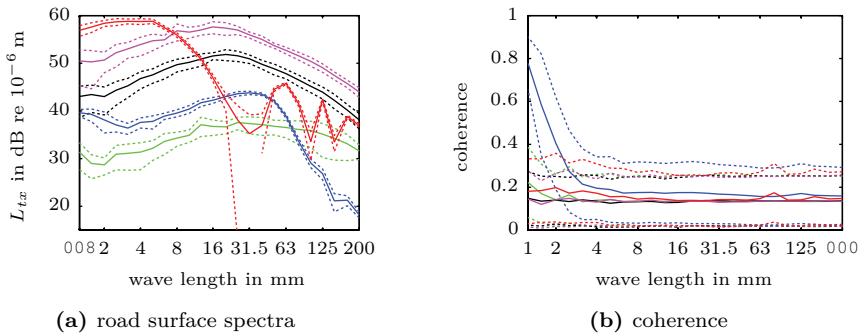


Fig. 6.6 Third-octave band averages (—) and standard deviations (···) of (a) road surface spectra over all lateral tracks and (b) coherence between lateral tracks. A (—), B (—), C (—), D (—) and E (—). Missing data denotes outlier.

The amplitude differences are also visible in Fig. 6.6a where road surface spectra L_{tx} [144] are given as mean values over all lateral tracks. The additionally shown standard deviations reveal that for most of the surfaces a quite pronounced variation between the individual lateral tracks exists. This is further emphasised by Fig. 6.6b which shows the mean and the standard deviation of the coherence between the lateral tracks (calculated according to [145]) for each road surface. Apart from the shortest wave lengths for surface A, coherence between the parallel tracks is bad and standard deviations are large.

Tab. 6.1 Arrangements of lateral tracks used in the simulations. Arabic numerals denote the position of a lateral track with regard to the reference contact simulation with complete lateral information. * denotes a reversed track. Alphabetic characters denote that longitudinal segments from surface scans being longer than one tyre revolution are used as lateral tracks (see text).

| config. | arrangement lat. tracks | config. | arrangement lat. tracks |
|------------------|-----------------------------------|---------|-------------------------------|
| reference | 1 2 3 4 5 6 7 8 9 10 11 12 | IV.a | 1 2 3 4 1 2 3 4 1 2 3 4 |
| I.a | 1 1 1 1 1 1 1 1 1 1 1 1 | IV.b | 5 6 7 8 5 6 7 8 5 6 7 8 |
| I.b | 6 6 6 6 6 6 6 6 6 6 6 6 | V | 1 2 3 4 5 6 1 2 3 4 5 6 |
| II.a | 1 2 1 2 1 2 1 2 1 2 1 2 | VI.a | 1 1* 1 1* 1 1* 1 1* 1 1* 1 1* |
| II.b | 5 6 5 6 5 6 5 6 5 6 5 6 | VI.b | 6 6* 6 6* 6 6* 6 6* 6 6* 6 6* |
| III.a | 1 2 3 1 2 3 1 2 3 1 2 3 | VII.a | a b c d e f a b c d e f |
| III.b | 5 6 7 5 6 7 5 6 7 5 6 7 | VII.b | a b c d e f f e d c b a |

For the contact simulations, all surface scans are resampled to match the resolution of the tyre model. The tyre is divided into 512 intervals over the circumference, giving a circumferential contact revolution of slightly less than 4 mm. In lateral direction, the contact size is associated with the size of the solid elements in the WFE model. This gives twelve contact tracks for the 175/65 R14 tyre which is a sufficiently high number for rolling noise calculations [52, Paper C].

6.2.2 Study methodology

The influence of the available lateral road surface data on the calculation of rolling noise and rolling resistance is examined by replacing individual distinct tracks in the reference configurations of twelve independent, unique lateral tracks with already present tracks. The number of available unique lateral tracks is assumed to range from one to half of the full data. Additionally, the repeated tracks are taken from different lateral locations in the reference configuration, and the beginning and end of the scan might be reversed. The scans of surfaces A and B are several tyre revolutions long. This allows for yet another repetition scheme in which later segments in rolling direction are used as lateral segments instead: for example, if the scan is four revolutions long, then the second revolution is used as second lateral track, the third revolution as third lateral track and so forth. A complete overview of all repetition schemes is given in Tab. 6.1, and an example of one case is shown in Fig. 6.7. Results are expressed as differences to simulation outcomes for the reference case. For rolling losses this is done in terms of the rolling resistance coefficient C_r and for rolling noise the overall or third-octave band A-weighted sound pressure level $L_{p,A}$ is used.

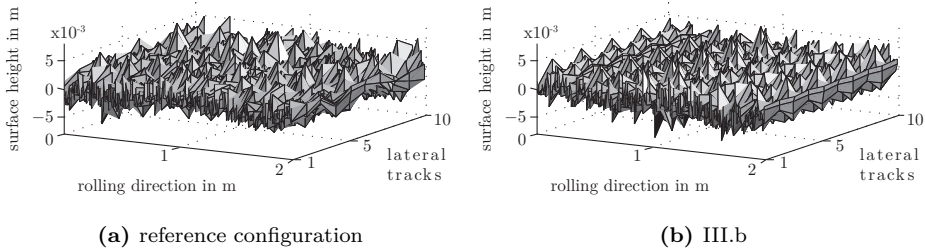


Fig. 6.7 Surface E with (a) complete lateral information and (b) reduced lateral information (III.b).

6.2.3 Results

Results for the rolling loss calculations are given in Fig. 6.8a. For the two ISO road surfaces A and C, and the SMA surface D, the variations of the rolling resistance coefficient C_r with respect to the reference case are less than 5% regardless of the number of unique lateral tracks and the applied repetition scheme. Considerably higher deviations are obtained for the rough surface B and the surface dressing E if only one or two tracks are repeated (schemes I, II and VI). The deviations are in the order of 5% to 40%, and vary depending on which lateral tracks are repeated (*a* or *b* configurations). For surface B four or more surfaces are necessary to reliably keep the variation below 5%. In the case of surface E, deviations of more than 10% are still obtained even when half of the lateral tracks are unique (scheme VI). Finally, results for cases where the lateral tracks are taken from longitudinal scans being longer than one revolutions, scheme VII, show an accuracy which is approximately between that obtained with three or four repeated tracks.

For rolling noise calculations the dependency of the total A-weighted sound pressure level $L_{p,A}$ on the lateral track data is even more pronounced, see Fig. 6.8b. Independent of road surface, plain repetition of just one lateral track (scheme I) leads to a gross overestimation of the sound pressure levels. While the introduction of some lateral variation by reversing every other track, scheme VI, considerably reduces the deviations, the error is still more than 1 dB for all surfaces but the drum-mounted ISO surface A. Using two or more unique tracks, deviations are less than 1 dB for both ISO surfaces (A/C). For surface D, the same accuracy is achieved with three or more original tracks. In the case of the generic rough and surface dressing surfaces B and E, variations of less than 1 dB can only reliably be obtained when at least six independent lateral scans exist. Similar to the results obtained for the rolling losses, the accuracy obtained with scheme VII is better than for just one lateral track (I), but not particularly better than that for scheme

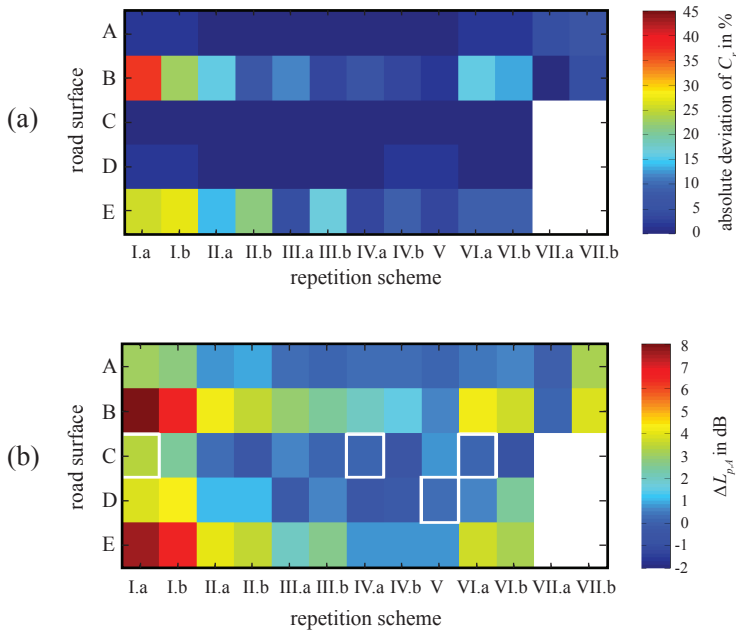


Fig. 6.8 Deviations of rolling loss and rolling noise calculations from the reference case. White areas denote omitted calculations. Rolling noise only: White frames denote cases where the deviation in all dominating third-octave bands is < 1 dB.

VI which is also based on only one lateral track. Moreover, results for a particular scheme again vary depending on which tracks are repeated (*a* or *b* configurations).

The rolling noise simulation results can be further analysed if third-octave band spectra are considered. Deviations of less than 1 dB in all of the most relevant third-octave bands (i.e. those dominating the overall level) are only observed in five cases as shown by the white frames in Fig. 6.8b. All of these cases are for surfaces C and E. No clear relations to a particular repetition scheme can be seen.

6.2.4 Concluding remarks

In order to answer the question whether an adequate simulation of rolling noise and/or rolling losses is possible if the number of available lateral road surface scans is limited, two different aspects have to be considered. The first one is how representative one particular track is for the whole surface. In Section 6.2.1 it could be shown that for typical road surfaces considerable differences exist between scans on parallel lines of the same surface. This is reflected in the rolling noise and

rolling resistance simulations, where huge differences can be observed for results obtained with the same basic repetition scheme, but different initial lateral tracks, for example II.a and II.b. The influence of the chosen individual track becomes the smaller the larger the number of unique tracks is, because a larger lateral section of the surface is covered. Though it could intuitively be assumed that variations between lateral scans are smaller for smoother surfaces, there is no indication of this in the present study.

The second aspect which has to be considered is which possibilities exist to extend the lateral data if only a limited number of parallel scans is available. The results indicate that for rolling loss simulations of smooth surfaces only very few tracks are necessary to obtain adequate results. This is because rolling losses on these surfaces are mostly depending on the large-scale running deflections of the tyre while entering and leaving the contact zone. Details of the road surface profile and lateral variations are of lesser importance as long as the surface is sufficiently smooth. For rougher surfaces the influence of the individual road asperities grows, see *Paper III* and Section 6.3. This means that the detailed profile structure and lateral variations are of concern. In this case, the results for surfaces B and E suggest that around six tracks (i.e. half of the number of actual contact tracks in the model) are necessary.

For rolling noise, the small-scale, high-frequency tyre excitation by the time varying contact forces due to the road texture is of great importance. Accordingly, surface details already have to be considered even for smoother surfaces. This is shown by the fact that at least three tracks seem to be necessary even for rather smooth surfaces if overall tyre/road noise levels shall be predicted with an accuracy of 1 dB. For rough surfaces the number rises again to five or six tracks.

The strong dependence of rolling noise on the road texture is additionally exemplified by the fact that for the majority of cases where the overall reference sound pressure level is sufficiently well approximated, still significant deviations in individual third-octave bands exist.

6.3 Predicting rolling resistance as a function of road surface profile and tyre tread pattern

This is a condensed version of Paper III. Main difference is the omission of results for rubberised surfaces and that no correlation analysis between road surface properties and rolling resistance is performed.

A reduction of rolling resistance is essential for a more environmentally friendly road transportation sector. Both tyre and road design can be utilised to reduce rolling resistance. In both cases a reliable simulation tool is needed which is

able to quantify the influence of design parameters on the rolling resistance of a tyre rolling on a specific road surface. In the present study rolling resistance is calculated for a series of different road surfaces. In addition, the influence of the tyre tread pattern on the rolling resistance is evaluated. Results are compared with the rolling resistance measurements reported in [146].

6.3.1 Tyre input data

In [146] rolling resistance measurements were conducted for two 225/60 R16 tyres: a Uniroyal Tigerpaw standard reference test tyre (SRTT) and a Continental CPC2 LI98 (CPC). The tread patterns of these two tyres and the corresponding local stiffness scaling factor profiles $\Phi_{e,r}$ (cf. Section 4.3) are shown in Fig. 6.9. As no material input data was available for these two tyres, the 205/55 R16 tyre model was used as basis for both tyres. This is deemed a viable solution as the study focuses on the qualitative effects of tread pattern and road surface. The tread patterns are not explicitly modelled; they are included in the tyre and contact simulations as outlined in Section 4.3. In addition to the SRTT and the CPC tyre, simulations are also performed for a slick tyre without any profile, even though no measurement data is available for this tyre. This is done to further evaluate the influence of the tread pattern on the rolling resistance. For the tyre structure non-proportional damping is used, and tyre/road interaction is calculated with a non-linear damping coefficient of $c = 3.25 \text{ Ns}\cdot\text{m}^{-2}$.

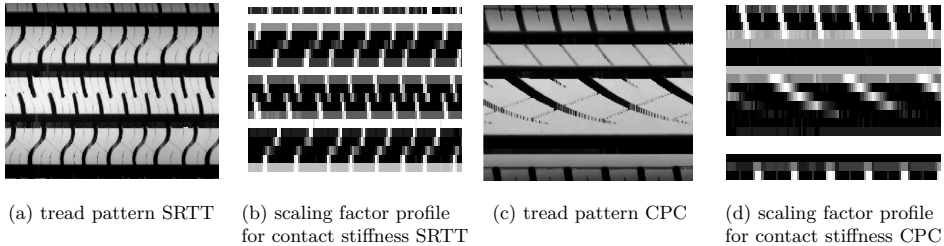


Fig. 6.9 Sections of the tread pattern (a/c) and the corresponding contact stiffness scaling factors $\Phi_{e,r}$ (b/d) of the two tyres. All sections have approximately the same dimensions. Solid white represents a scaling factor of zero and solid black a factor of one in (b/d).

Tab. 6.2 Considered road surfaces.

| road type | abbreviation | aggregate size (layer thickness) |
|-----------------------------------|--------------|---|
| artificial smooth surface | smooth | - |
| ISO 10844 reference surface [143] | ISO | - |
| dense asphalt concrete | DAC | 0/16 |
| thin-layered asphalt | TLA | 2/4, 2/6, 4/8 |
| stone mastic asphalt | SMA | 0/6, 0/8, 0/11, 0/16 |
| porous asphalt concrete | PAC | 2/4, 2/6, 4/8, 0/11, 8/11 (45mm), 8/11 (200mm), 0/16 |
| surface dressing | SD | 5/8, 11/16 |

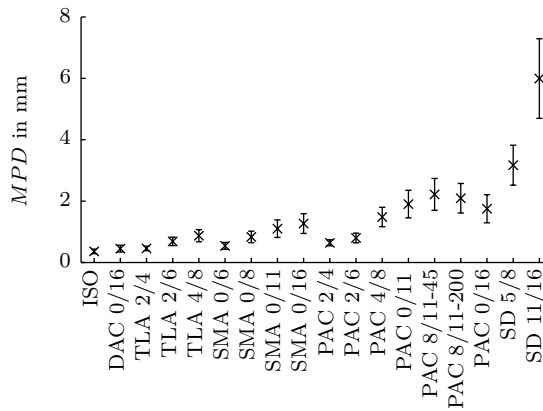


Fig. 6.10 Average of the mean profile depth (*MPD*) for all road surfaces. Average based on all measurement positions and all tracks. Errorbars indicate standard deviation.

6.3.2 Road properties

Simulations are performed for the 19 road surfaces given in Tab. 6.2. All surfaces apart from the smooth one are test fields at a dedicated test site in Kloosterzande, the Netherlands [147]. For each surface, texture scans were performed at six different positions in the corresponding test field. The determination of road properties and the rolling resistance calculations are performed individually for all of the available profile scans for each surface. In the following the average of these results is typically presented.

Each scan consists of 20 parallel tracks of length 2.95 m and a lateral spacing of 0.01 m. The resolution in rolling direction is 0.2 mm for all road surfaces. For the contact simulations, all surface scans are resampled to match the resolution of the

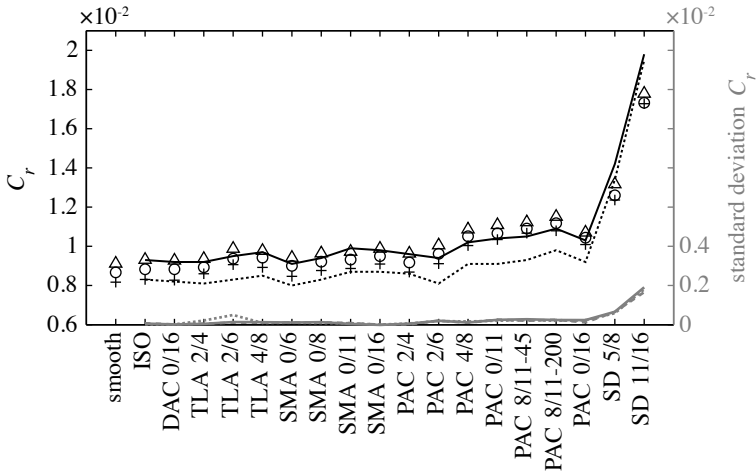


Fig. 6.11 Left y -axis (black): rolling resistance for CPC measured (—) and simulated (\circ), SRTT measured (\cdots) and simulated ($+$), and the simulated slick tyre (Δ). No measured data available for the slick tyre. Right y -axis (grey): standard deviation for CPC (—), SRTT (\cdots), and the slick tyre (—). Note: identical step size on both y -axes.

tyre model, giving a circumferential contact revolution of 1.9 mm.

A single-value characterisation of the road surface profiles is possible by means of the mean profile depth MPD [148]. Results are shown in Fig. 6.10. The MPD correlates approximately with the maximum aggregate size of the road surface. Additionally, an increase in standard deviation can be observed with increasing surface roughness, i.e. increasing MPD .

6.3.3 Rolling resistance calculations

Rolling resistance was measured at the same test site where also the road surface profiles were scanned. A trailer designed by the Technical University of Gdansk was used to directly measure the rolling resistance coefficient C_r . The measurements were conducted at a speed of 80 km/h and axle load of 4100 N [146].

Calculated and measured rolling resistances for the different road surfaces and tyres are shown in Fig. 6.11. For the CPC tyre a generally good agreement with the measurements is achieved. Absolute values and the relative ranking of the road surfaces are captured well with a slight underestimation of the measured values for most of the surfaces. Only the C_r values for the PAC surfaces, apart from the one with aggregate size 2/4, are overestimated by roughly 10%. The SD 11/16

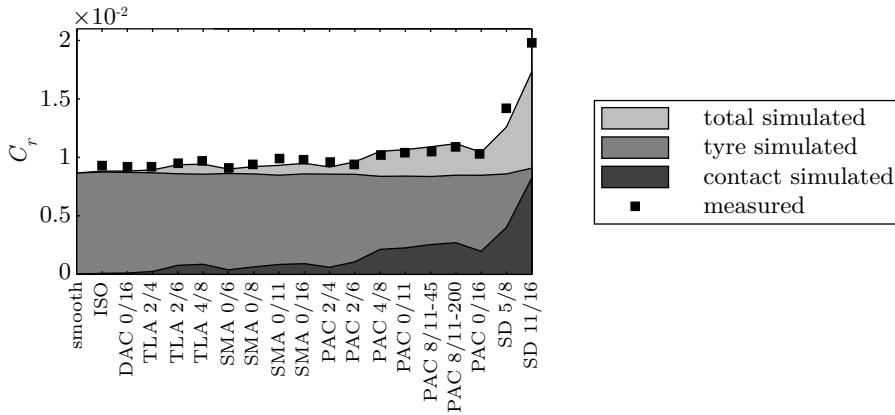


Fig. 6.12 Contribution of the tyre structure and the small-scale tread deformations to the simulated rolling resistance of the CPC tyre.

in contrast, is underestimated by about the same margin. The measurements for the SRTT show a similar behaviour to the CPC results but are around 5% lower for most of the surfaces. This is slightly less than in the measurements where the difference between CPC and SRTT is about 10%. This is most likely related to the fact that an identical tyre structure with only minor adjustments for the tread pattern is used to model both tyres. In reality there are differences in the tyre construction between the SRTT and the CPC, and this affects the rolling resistance as well.

No measured data is available for the slick tyre. Yet, the different road surfaces have a similar influence on the rolling resistance as for the two other tyres. However, the rolling resistance is always higher than for the two tyres with profiles. This agrees with the measurement results reported for other tyres in [149], and can be explained by the additional rubber material in the tread of a slick tyre [16]. For all tyres the lowest rolling resistance is obtained for the smooth surface.

Generally, the biggest difference between simulated and measured values is obtained for the SD 11/16 surface with an underestimation of the C_r by about $0.2 \cdot 10^{-2}$. For the SD 11/16 the standard deviation of C_r is the highest of all surfaces, and of about the same order as the difference between simulations and measurements. It is not completely clear from [146] how the six different scans for each road surface and the driving track for the C_r measurements align, and how the averaging for the latter is done. Accordingly, the higher deviation between simulations and measurements might be explained by variations of the SD 11/16 surface over the complete test field. Another aspect which has to be considered is that an identical contact stiffness k is used for all road surfaces during the sim-

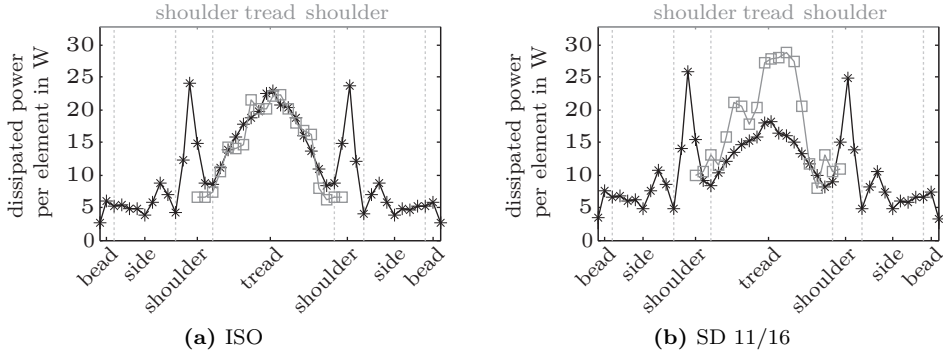


Fig. 6.13 Distribution of dissipation over the CPC tyre cross-section. Each (*) marks one shell element, each (□) one solid element. (···) marks the different tyre regions.

ulations. For most of the surfaces this is a valid simplification as their MPD are within the same limited range of values. This is not the case for the SD 11/16 surface and better match to measurements might be achieved by an appropriately adjusted contact stiffness.

In Fig. 6.12 the distribution of the simulated rolling losses between large-scale tyre structure losses, Eq. (4.45), and small-scale tread losses, Eq. (4.48), is shown for the CPC tyre. Similar results are obtained for the other two tyres. The contribution of the tyre structure to the rolling resistance, $C_{r, \text{tyre}}$, is nearly identical for all road surfaces; the average is around $0.86 \cdot 10^{-2}$ with a range of $0.08 \cdot 10^{-2}$. Even though the total contribution of the tyre structure to the rolling resistance is very similar for all surfaces, there are some differences in which parts of the tyre contribute most. This is shown in Fig. 6.13 where the distribution of losses over the different elements in the WFE mesh is shown for the CPC tyre and the ISO and SD 11/16 surfaces. While the contribution of the bead, sidewall and shoulder areas is nearly identical, some differences are obtained for the tread region. For the ISO surface the losses originating from the solid and the shell elements in the tread region are nearly identical, see Fig. 6.13a. For the SD 11/16 surface, in contrast, there is considerably less contribution from the shell elements, and more contribution from the solid elements, see Fig. 6.13b. Expressed differently, for the ISO surface the tyre contributes more globally with a deformation of the whole belt/tread structure to the losses. For the rougher surface there is less global contribution from the tyre structure and more contribution from a local deformation of the tread rubber by the road surface asperities.

The minimal variation of $C_{r, \text{tyre}}$ for the different road surfaces implies that the

variation of the rolling resistance for the different road surfaces is mainly explained by a variation of the losses originating in the small-scale contact deformation $C_{r,\text{contact}}$. This is confirmed by Fig. 6.12 where the small-scale contribution varies from negligible $0.9 \cdot 10^{-4}$ for the ISO surface to $0.825 \cdot 10^{-2}$ for the SD 11/16, which is nearly half of the overall C_r for this surface. Identical tendencies are visible for the other two tyres.

6.3.4 Concluding remarks

Measured and simulated rolling resistances have been compared for combinations of three different tyres and 19 conventional road surfaces. The agreement between measured and simulated rolling resistance coefficients is very good. The influence of different tread patterns is adequately captured; some limitations compared to measurements on different tyres are given by the fact that only the different tread patterns but not the different tyre structures have been modelled. In the simulations the influence of the road surface texture on the rolling resistance is very similar to the measurements.

It was found that rolling resistance can be split into two parts: one part originating from the large-scale tyre structure deformations, and the other part arising from small-scale tread indentations. The contribution of the tyre structure to the overall rolling resistance is nearly identical for all road surfaces. However, variations of the distribution of losses between the belt package and the tread rubber are observed, with the tread contributing more for rougher surfaces. The losses due to small-scale tread deformations are highly texture depending and range from 0% to nearly 50% of the overall losses. Summarising, it can be concluded that for smooth surfaces rolling resistance is mainly due to a global deformation of the tyre structure, whereas for rougher surfaces significant contributions are made by local deformations of the tread due to roughness asperities. The latter also leads to slightly less global deformation of the tyre, meaning that the tyre structure is of lesser importance for the rolling resistance on rougher road surfaces.

6.4 Simulation of free wave propagation on a truck tyre

This is a condensed version of Paper IV. Main differences are the omission of forced response validation examples, a reduced number of modeshape examples, a shorter analysis of semi-rigid body motion, and no analysis of phase speeds and asymmetric waveforms.

A substantial part of road traffic noise originates from rolling noise caused by the tyres of trucks and other heavy vehicles. These do not only contribute some 10%

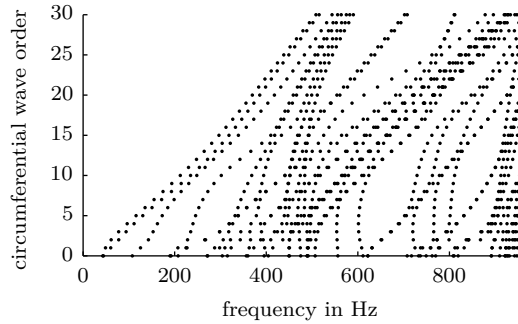


Fig. 6.14 Dispersion relations. Each dot represents a free response solution for the undamped tyre.

to the overall road mileage travelled [150], their maximum pass-by levels are on average also 4 dB to 7 dB higher than those of cars [151]. The majority of research on rolling noise is focussed on car tyres. It is not clear in how far results are applicable to truck tyres as well, as there are structural differences between car and truck tyres. As a first step towards understanding truck tyre rolling noise, the free response of a truck tyre up to 1 kHz is modelled.

6.4.1 Dispersion relations

Valuable insight into the wave propagation on the truck tyre can be gained from a dispersion plot as shown in Fig. 6.14. It shows the relation between frequency and circumferential wave order for a specific eigenvector $\Psi_{n,s}$ in Eq. (4.10). The dispersion relations are rather complicated and consists of 47 branches (or parts thereof) in the range up to 1 kHz. A better picture of the dispersion relations can be obtained by distinguishing whether the waves exhibit a cross-sectional deformation pattern which is symmetric with respect to the tread centre line or not¹. Within this summary section of the thesis the presentation of results will be limited to symmetric cross-sectional deformations; this type of motion is more likely to be excited during rolling. Results for asymmetric mode shapes are included in *Paper IV*.

The corresponding dispersion diagram for the symmetric case can be seen in Fig. 6.15, where each $\Psi_{n,s}$ is marked by a symbol representing the wave group it belongs to. The different waveforms are discussed in Section 6.4.2.

In the dispersion relations branches can be defined as a succession of eigen-solutions with increasing wave orders and similar or closely related cross-sectional

¹In the following this distinction will simply be referred to as “symmetric” and “asymmetric”.

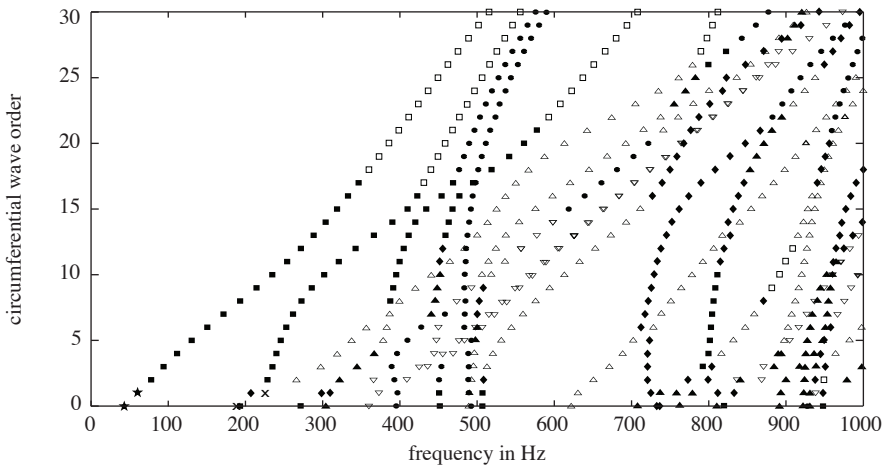


Fig. 6.15 Dispersion relations for symmetric cross-sectional mode shapes. Type of motion: ★ semi-rigid, ■ out-of-plane, □ out-of-plane (sidewall only), ▲ in-plane, △ in-plane (sidewall only), ▽ in-plane (belt only), ◆ in- and out-of-plane, × belt extension/in-plane belt, ● tread block.

mode shapes. This does not include a requirement that mode shapes belonging to low and high circumferential wave orders of one branch necessarily need to be identical. The change in circumferential vibration pattern with increasing wave order, a frequency dependent influence of tyre material and geometry, and other effects, can lead to significant differences between low- and high-wave-order mode shapes. However, a close relation can be expected for vibrational patterns belonging to successive wave orders of a branch.

Branch identification is done by visual inspection of the mode shapes, application of the modal assurance criterion (*MAC*) [152], and identification of degrees-of-freedom with maximum strain energy storage [74].

6.4.2 Wave shape analysis

For car tyres four main wave groups could be identified in [74]: (i) semi-rigid body waves, (ii) slow waves with out-of-plane motion of the cross-section or the sidewalls only, (iii) waves with in-plane motion of the sidewalls, and (iv) fast waves with significant out-of-plane extension of the belt region. In the following the symmetric dispersion relations and waveform shapes for the truck tyre will be evaluated to see if the main types of wave motion are similar to the car tyre.

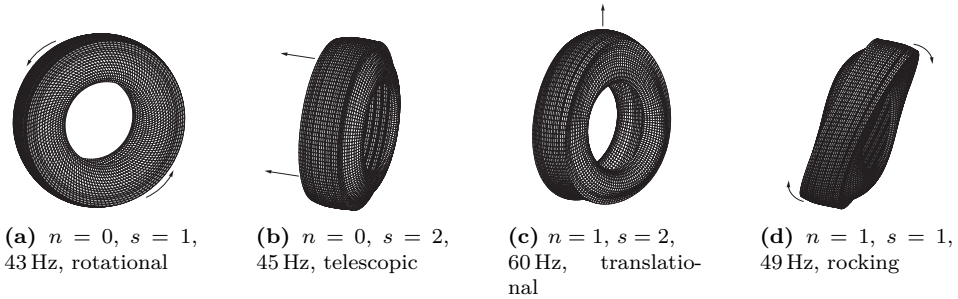


Fig. 6.16 Semi-rigid body modes (★ in Fig. 6.15, (b/d) not shown there since these are asymmetric). The relative motion of the tyre with respect to an assumed fixed wheel is indicated by arrows.

Semi-rigid body waveforms

As the tyre's motion is blocked at the bead, the solutions to the eigenvalue problem Eq. (4.10) for $n = \{0, 1\}$ and $s = \{1, 2\}$ correspond to semi-rigid body motion; the sidewalls act as supporting springs and the belt region moves relative to the rim. The first semi-rigid waveform, Fig. 6.16a, is given by a displacement of the belt in circumferential direction; it is referred to as “rotational” waveform. Similarly, in Fig. 6.16c the belt region is radially displaced in the “translational” waveform. Further waveforms are given by a lateral displacement (“telescopic”) or rotation (“rocking”) of the belt, see Figures 6.16b and 6.16d. The semi-rigid body waveforms are of minor importance for rolling noise under steady-state conditions. The exception is the translational form which is strongly excited by radial forces.

Out-of-plane motion of the tyre cross-section

This type of motion is identical to the behaviour of group (ii) for the car tyre. In the low to medium wave order range it is characterised by a bending type, out-of-plane motion of the complete tyre cross-section. The first symmetric branch evolves out of the translational semi-rigid body waveform and involves a vibrational pattern of $m = 3$ half-wavelengths² over the cross-section. An example of this branch is given in Fig. 6.17a. In [74] a clear succession of branches for this wave type with $m = 3, 5, 7, \dots$ was identified. The second, $m = 5$, branch is still very distinct for the truck tyre, see Fig. 6.15. For higher frequencies, branches can no longer be completely associated with this type of motion as other vibrational patterns appear

²In the following m will be used to denote the number of half-wavelengths of cross-sectional deformation.

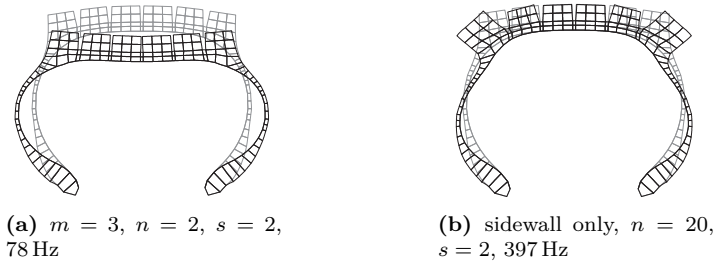


Fig. 6.17 Examples of symmetric out-of-plane cross-sectional mode shapes (■ and □ in Fig. 6.15).

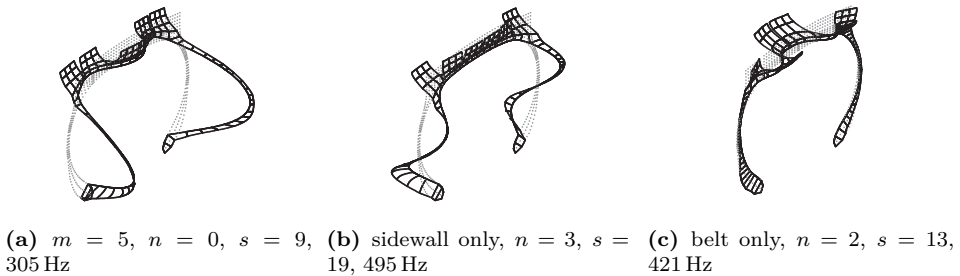


Fig. 6.18 Examples of symmetric in-plane cross-sectional mode shapes (▲, △, and ▽ in Fig. 6.15).

as well. Still, sections of dispersion branches, e.g. from 390 Hz to 450 Hz and $n = 8$ to $n = 17$, or 790 Hz to 830 Hz and $n = 3$ to $n = 10$, can be attributed to strong out-of-plane deformation of the whole cross-section. For higher circumferential orders, approximately $n \geq 15$, the waveforms gradually change to out-of-plane deformation of the sidewalls only. Deformation of the belt region is limited or non-existent, see Fig. 6.17b.

In-plane motion of the tyre cross-section

This type of motion is characterised by a predominantly in-plane deformation of the tyre cross-section. Contrary to group (iii) in [74], deformations are not limited to the sidewalls only for the truck tyre. Similar to the out-of-plane motion, in-plane deformations of odd numbers of half-wavelengths over the complete cross-section can be observed for the symmetric case, see Fig. 6.18a. This type of motion is, however, relatively rare and limited to only short parts of some branches; longer

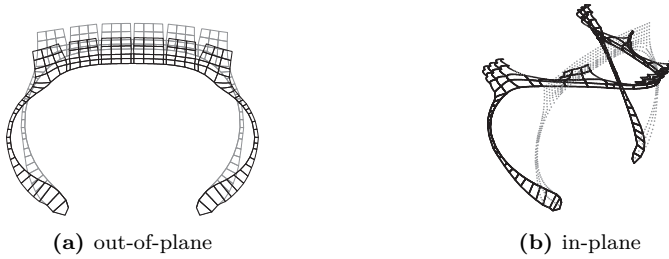


Fig. 6.19 Example ($m = 3$, $n = 0$, $s = 5$, 192 Hz) of symmetric cross-sectional mode shapes with both strong in- and out-of-plane components (♦ in Fig. 6.15).

sections appear only around 900 Hz and above. More common is the sidewall-only in-plane deformation shown in Fig. 6.18b which had also been identified for the car tyre. From Fig. 6.15 it is obvious that this type of motion constitutes prolonged sections of branches or even complete branches. It appears in nearly the complete frequency- and wave-order-range covered in Fig. 6.15, leaving out only the lowest frequencies below 300 Hz. Finally, there is a group of waves for which the in-plane motion is limited to the belt region, see the example in Fig. 6.18c. In Fig. 6.15 it can be seen that these waveforms are mostly limited to two branches starting between 300 Hz and 400 Hz and extending all the way up to 950 Hz and $n = 30$ with nearly constant slope.

Concurrent in- and out-of-plane motion of the tyre cross-section

So far the tyre waveforms have been divided into purely in- or out-of-plane motion. Due to the nature of the wave motion and the tyre construction and shape, no waveform will be exclusively in- or out-of-plane only. There is always an in-plane component for dominantly out-of-plane motion and vice versa. However, for all of the wave groups mentioned so far either in- or out-of-plane deformations are clearly dominating. For some waves such a clear distinction is not possible as the motion consists of both strong in- and out-of-plane components. The resulting waveforms take the shape of a combination of the out-of- and in-plane waveforms presented in the previous two sections, see Fig. 6.19. In the dispersion plot Fig. 6.15 the only prolonged continuous section of this waveform appears in the branch starting at 730 Hz and $n = 0$. All other occurrences are mostly limited to shorter branch sections or isolated free response solutions.

The appearance of this waveform often marks a section of a branch in which the cross-sectional mode shape changes from for example out-of-plane motion at lower wave orders to in-plane wave motion at higher wave orders (or vice versa). One

example is the branch rising as a nearly straight vertical line at around 800 Hz in Fig. 6.15. From $n = 3$ to $n = 10$ waveforms are of out-of-plane type before turning into the combined in-/out-of-plane type at $n = 11$. This waveform continues until $n = 17$, after which the branch continues with in-plane motion.

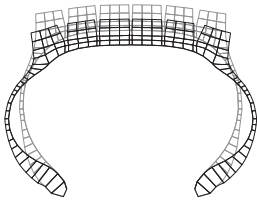
The very localised appearance of the combined in-/out-of-plane motion in the dispersion diagram might be one reason why this waveform has not been mentioned in free response studies of car tyres (e.g. [42, 74, 77]). It is difficult to detect these waveforms unless the deformation shape of every free response solution in the dispersion diagram is analysed with respect to in- and out-of-plane components. Moreover, the construction differences and the higher inflation pressure might make the truck tyre more susceptible for in- and out-of-plane coupling.

Belt extension motion

A second type of wave with symmetric out-of-plane motion of the cross-section has been identified for car tyres. It is indicated as group (iv) in [74], where it is associated with significant extension of the cross-section or the belt region. For the truck tyre a branch with this waveform cuts on at 190 Hz, see Fig. 6.20a and \times in Fig. 6.15. The mode shape in Fig. 6.20a distinguishes itself from the symmetric out-of-plane cross-sectional mode shape shown in Fig. 6.17a by the belt bending which is visible for the latter. In Fig. 6.20a belt motion is purely extensional. This involves significant elongation along the tyre perimeter which makes the tyre behave rather stiff and explains the higher eigenfrequency compared to the out-of-plane waveform. In [74] this waveform is associated with strong curve veering effects and cross-sectional out-of-plane mode shape changes. Similar observations are made for the truck tyre, albeit with even more drastic deformation pattern changes. Fig. 6.20 shows how the waveform rapidly transforms with increasing circumferential wave order n : it changes from out-of-plane extension of the whole cross-section to in-plane deformation of the sidewalls and shoulder regions only. By $n = 2$ the out-of-plane motion is so weak that the waveform has to be considered to be of the in-plane sidewall-only type of deformation discussed in Section 6.4.2. Accordingly, the rest of the branch is marked by \triangle in Fig. 6.15. The change in dominating wave motion is accompanied by an altered branch slope in Fig. 6.15.

For car tyres, this waveform has also been referred to as “fast extensional mode” [53] or “in-plane ring mode” [57]. Though never explicitly stated in [74], this waveform is associated with in-plane motion of longitudinal waves over the tyre circumference. The first wave with $n = 0$ cuts-on at the ring frequency which is roughly 200 Hz for the truck tyre. This is within 5% of the eigenfrequency of the $n = 0$ wave in Fig. 6.20a.

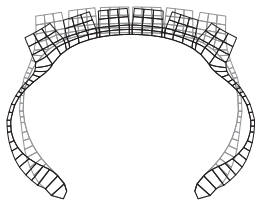
At and below the ring frequency, in- and out-of-plane motion are strongly coupled due to the finite curvature of the tyre. This is the reason why this longitudinal wave is characterised by significant out-of-plane extension of the belt region,



(a) $n = 0, s = 4, 190 \text{ Hz}$, out-of-plane



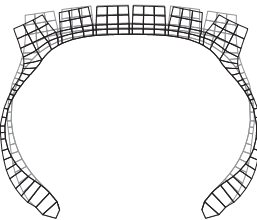
(b) $n = 0, s = 4, 190 \text{ Hz}$, in-plane



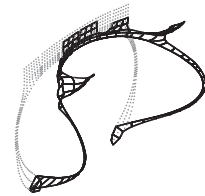
(c) $n = 1, s = 5, 225 \text{ Hz}$, out-of-plane



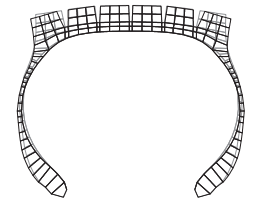
(d) $n = 1, s = 5, 225 \text{ Hz}$, in-plane



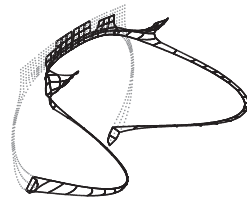
(e) $n = 2, s = 5, 266 \text{ Hz}$, out-of-plane



(f) $n = 2, s = 5, 266 \text{ Hz}$, in-plane



(g) $n = 3, s = 5, 298 \text{ Hz}$, out-of-plane



(h) $n = 3, s = 5, 298 \text{ Hz}$, in-plane

Fig. 6.20 Development of the cross-sectional mode shape for the belt extension. (a) to (d) marked by \times in Fig. 6.15, (e) to (h) by Δ .

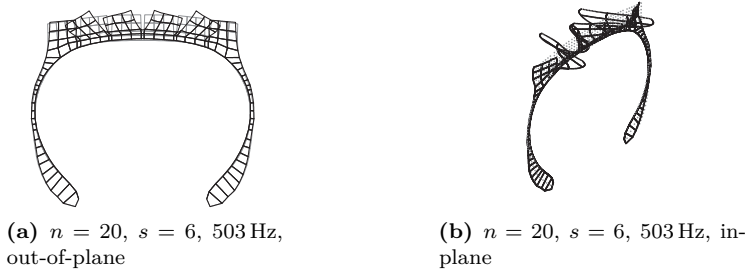


Fig. 6.21 Examples of symmetric tread block mode shapes (\bullet in Fig. 6.15).

at least for lower circumferential orders. Above the ring frequency the coupling decreases gradually, which explains the increasing dominance of in-plane motion for the higher wave orders in Fig. 6.15. The shift from out-of-plane to purely in-plane motion has not been reported for the car tyre in [74]. As in-plane motion was not explicitly shown for this wave type, however, the significance of in-plane motion for this waveform in the car tyre is difficult to assess. It is conceivable that out-of-plane motion remains more dominant for the car tyre because of the significantly lower bending stiffness of its ply and belt laminates, and the lower inflation pressure.

Tread block motion

A type of wave motion which is rarely mentioned in free response studies of car tyres are vibrations of only the tread block. While many waveforms exhibit some form of tread block deformation which is not directly related to the motion of the belt, see e.g. Fig. 6.17b, a large number of waves exist for which belt deformation is minimal and the main type of motion is a combination of in- and out-of-plane tread block vibrations, see the example in Fig. 6.21. In the dispersion relations in Fig. 6.15 it can be seen that this is one of the most frequent types of motion for wave orders of approximately 15 and above. It is, however, not restricted to the high wave order range with waves of this type forming branches in the low to mid-wave order regions between 380 Hz and 500 Hz.

The comparably high frequency of occurrence of this waveform can be explained by the tread blocks' ability to move nearly independently from each other, implying a large variety of possible vibrational patterns for the whole tread.

For typical car tyres tread block dynamics are of minor relevance for free response considerations in frequency regions below roughly 2 kHz [29]. Accordingly, the waves of this group have, comparable to the combined in-/out-of-plane belt deformation waveforms, rarely been mentioned in free response studies of car tyres.

Exceptions are studies explicitly dedicated to tread block dynamics [95] or high frequency vibrations [28, 29].

6.4.3 Concluding remarks

The comparison to results reported for car tyres in literature reveals a much more complex nature of wave motion for the truck tyre. For the semi-rigid body motion differences in order and spacing of the eigenfrequencies could be observed. The waveforms with out-of-plane motion of the cross-section are very similar to those of the car tyre, where this waveform was the most common one. This is no longer the case for the truck tyre where it is only dominating at low frequencies. Waves with in-plane deformation of the cross-section also appear for the truck tyre. However, compared to the car tyre this type of motion is not limited to the sidewalls only; large in-plane motion of the whole cross-section or the belt region only is observed as well. A large part of the free response solutions above 300 Hz belong to this group. This is in contrast to the findings for the car tyre [74], where only four branches of this waveform could be found for frequencies below 1.5 kHz.

Major differences can also be observed for the fourth group of waves, those with significant belt extension. For the truck tyre this cross-sectional mode shape appears at lower frequencies than for the car tyre and only exists for the lowest wave orders. For higher orders the motion quickly changes to a in-plane sidewall deformation.

For the truck tyre two types of waves are observed which have not been reported for the car tyre. The first type combines the motion of the aforementioned in- and out-of-plane waveforms in such a way that neither in- nor out-of-plane motion is clearly dominating. Waves of this type often occur when the cross-sectional motion within a branch changes, for example around a veering zone. The second previously unreported wave group is characterised by strong tread layer deformations with limited or no motion of the tyre carcass. A large number of eigensolutions, especially for higher wave orders, belongs to this group. Due to the reduced geometric dimensions of car tyres, the tread block vibrations often occur at frequencies which are above the typical range covered in free response studies of complete car tyres [95]. Accordingly, it should be possible to observe these waves as well for car tyres provided that a tread pattern is modelled and the frequency range is high enough.

6.5 Simulation of truck tyre rolling noise

This is a condensed version of Paper V.

In Section 6.4 the necessity for a better understanding of truck tyre rolling noise has been pointed out, and results for free wave propagation on a truck tyre have been presented. In this section this work is continued and the 315/80 R22.5 truck tyre model presented in Section 6.4 is used as basis for calculating the exterior rolling noise of a truck tyre rolling on a real road surface under steady-state conditions.

6.5.1 Setup

Simulations are performed for a stone mastic asphalt (SMA) surface with aggregate size 0/8. The surface is a sample from a test field at a dedicated test site in Geilenkirchen, Germany. Surface texture scans were performed at six different positions in the test field. For each position scans of ten parallel tracks of length 1.96 m and a lateral spacing of 0.01 m are available. The scan resolution in rolling direction is 0.2 mm. For the simulations the roughness profile is resampled to match the resolution of the tyre model.

Tyre/road noise measurements were carried out using a dedicated measurement trailer, cf. [147]. Nine microphones were mounted around the tyre in a half-circle of radius 1 m from the tyre centre and a height of 0.25 m over the ground. The first and the last microphone were mounted exactly in the front and the rear of the tyre, and the other microphones were each spaced 22.5° apart from each other. Third-octave bands from 315 Hz to 5 kHz were covered in the measurements.

For the simulations the same nine points are used to evaluate the sound pressure. Additional field points are added every two degrees on the half-circle to minimise the influence of possible directivity deviations. Rolling noise is calculated separately for each of the six texture profile measurement positions within a particular road surface test field. The average and the range of the sound pressures are determined and the corresponding sound pressure levels are calculated.

The measurements were conducted with an axle load of 2000 kg and a driving speed of 60 km/h. The same values are used for the simulations. Rolling is calculated for five full tyre revolutions of which the last one is evaluated. Based on the circumferential tyre resolution this gives a frequency resolution of roughly 5 Hz and a maximum frequency of 2210 Hz.

6.5.2 Results

A comparison between the measured and simulated A-weighted third-octave band rolling noise spectra is shown in Fig. 6.22. The shape of the simulated and the measured spectra is similar. Nearly perfect agreement in sound pressure levels is

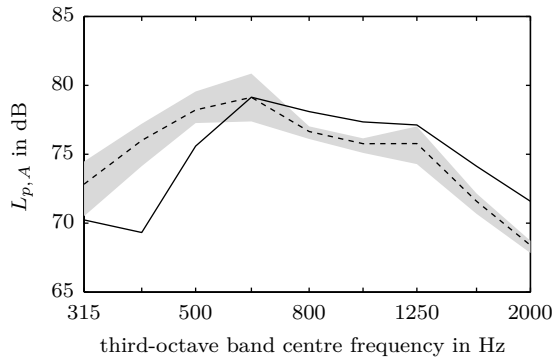


Fig. 6.22 Measured (—) and simulated (---) third-octave band rolling noise spectra. Simulation based on the average sound pressures for all six measurement positions. Grey shading indicates range of results from individual surface scan positions.

obtained for the 630 Hz third-octave band where the maximum of the measured rolling noise spectrum is located. For lower frequencies the simulations overestimate the measured values by 2.6 dB in the 315 Hz and 500 Hz third-octave bands, and by 6.7 dB in the 400 Hz band. It is apparent that the overestimation starts to appear for third-octave bands for which the wave length is in the order of the distance of the microphones/field points to the tyre. Accordingly, near field effects are to be expected for these frequencies. It is possible that the near field is not captured in the same way in the measurements and the simulations.

From 800 Hz to 1.25 kHz good agreement is achieved with an underestimation of maximum 1.6 dB in these frequency bands. For higher frequencies the deviation increases to 3.2 dB at 2 kHz. That the simulated sound pressure levels are too low for higher frequencies can be explained by an increasing importance of aerodynamic sources mechanisms for rolling noise at frequencies of about 1 kHz, see Section 2.2.2. Aerodynamic mechanisms are not accounted for in the simulations and hence a certain underestimation of measured sound pressure levels can be expected.

The total A-weighted sound pressure level is 85.4 dB for both the measurement and the simulations. A large part of this excellent agreement can be attributed to the accurate prediction of the peak sound pressure level in the 630 Hz third-octave band. However, it has to be acknowledged that the overestimation of the measured levels for low frequencies and the underestimation for high frequencies seem to cancel each other out in a beneficial way.

In Fig. 6.22 an important observation can be made regarding the range of the

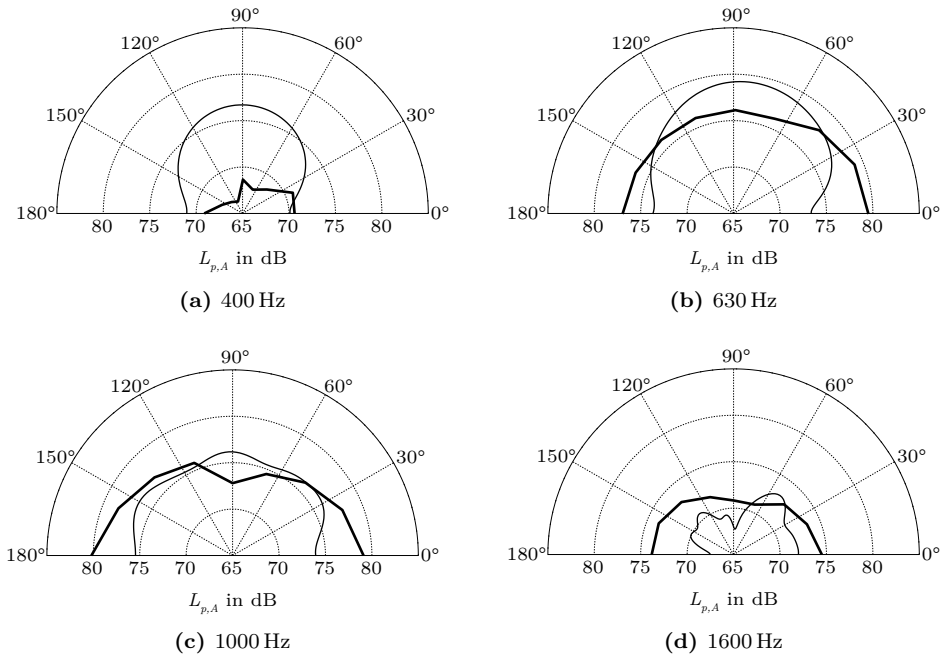


Fig. 6.23 Comparison of directivity between measurements (thick line) and simulations (thin line). Top view with the tyre rolling to the right.

simulated sound pressure levels over the different surface scan positions: for all third-octave bands up to 630 Hz and the 1250 Hz band, the range between the highest and lowest calculated level is between 2 dB to 4 dB. This emphasises the necessity to base the simulations on road surface scans from several locations in the test field. Otherwise there is a risk of obtaining non-representative results; not only for certain frequency bands but possibly also for the total sound pressure level. For higher frequencies the range reduces to maximum 1.5 dB.

Some examples of the directivity of the sound radiation are shown in Fig. 6.23. For the measurements maximum values are always obtained exactly in the front or rear of the tyre. This is not the case for the simulations where radiation is highest directly to the side for all third-octave bands apart from the 1.6 kHz one. Fig. 6.23a gives some insight into why the simulations overestimate the sound pressure levels at lower frequencies: compared to the measurements, levels are nearly identical at the front and rear, yet there is too much sidewall radiation. With increasing frequency, see the 630 Hz and 1 kHz results in Figures 6.23b and 6.23c, there is better agreement between measurements and simulations for the lateral

direction. At the same time there is an increasing tendency of underestimated simulated sound pressures in the front and rear. This might again be related to an increasing importance of aerodynamic sources. Interesting are the results for the 1.6 kHz third-octave band in Fig. 6.23d. The simulated sound pressure is, with the exception of a small area around 60° , again too low. This could be expected from the rolling noise spectra in Fig. 6.22. Somewhat surprising is the difference in the general shape between the directivity of the measured and the simulated radiation. The measurements are characterised by an elliptical directivity which favours the front and aft of the tyre. The simulations, in contrast, show a directivity pattern with distinct lobes around 60° and 120° , and minima at 90° and 180° . This shows that the relevant sound source in the measurements continues to be small compared to the wave length whereas this is not the case anymore for the simulations. This is another indication for over-proportionally high contribution of sidewall radiation in the simulations.

A slight uncertainty about the measurement results in Fig. 6.23d remains because the accuracy of the directivity suffers somewhat from the limited number of microphones. Furthermore, it is not clear if and how measurement results are possibly affected by the measurement trailer, for example due to reflections.

6.5.3 Concluding remarks

Excellent agreement between simulations and measurements has been achieved for the total A-weighted sound pressure level. The dominating third-octave bands in the rolling noise spectrum are also very well predicted. However, an overestimation of the measured spectrum can be observed for lower frequencies, and an underestimation at higher frequencies. The high frequency differences can be explained by not accounting for aerodynamic mechanisms in the simulation tool. Possible reasons for low frequency deviations include an insufficient representation of the near field in the simulation. Based on a directivity analysis there is also too much radiation from the tyre side in the calculations.

The study also reveals that local roughness variations can have a significant influence on the simulated rolling noise spectrum. For some frequency bands several dB difference in calculated rolling noise can be observed depending on where on the surface the profile scan was taken. This means that it is necessary to calculate the average rolling noise for several surface scans of a particular road segment. Otherwise results are possibly not representative and cannot be compared to pass-by or close-proximity measurements.

7 Conclusions and future work

7.1 Conclusions

A tool for the simulation of car and truck tyre vibrations, rolling losses and rolling noise has been presented. It consists of a waveguide finite element model of the tyre structure, a time-domain based non-linear tyre/road contact module, and a boundary element method radiation module. Rolling resistance is calculated based on the input power for steady-state rolling. Additionally, the necessary steps for the reduction of tyre design data into equivalent material properties for the shell and solid elements used in the tyre model have been presented.

WFEM has proven to be a valuable tool for the simulation of the tyre structure. The tyre cross-section can be modelled as detailed as necessary while the analytical wave approach in circumferential direction keeps the numerical effort low. The potential shortcoming of being limited to a homogeneous tyre circumference has so far not been a problem. For almost all applications there is no need to explicitly model geometric details of a circumferential tread pattern. It is sufficient to account for the voids by global mass/stiffness adjustments. The presented method for the estimation of material input data for the tyre model has been successfully demonstrated by the implementation of a 175/65 R14 car tyre (cf. [142]), and a 315/80 R22.5 truck tyre (cf. Section A.3) into the simulation framework.

The quality of free and forced response simulations is satisfying as exemplified by the results presented in *Papers I*¹ and *IV*, and Section A.3. Differences to measurements are in large parts explainable by uncertainties regarding material parameters. Possible problems in the sidewall representation in the WFE model are indicated by the modelled load-deflection curves and the lowest eigenfrequencies in *Paper IV*. It remains unclear if this is caused by the sidewall material properties, the particular cross-sectional WFE mesh of the 175/65 R14 tyre used in that study, or if this caused by the general inability of the WFE model to capture the non-linear softening of the sidewall membrane under loading.

An advantage of WFEM is an easy post-processing because of the inherent differentiation between cross-sectional modes shapes and circumferential waves. This makes data analysis rather simple. The numerical efficiency and effortless post-processing were particularly apparent while working on *Paper I*. The FE

¹To facilitate readability only papers and not also the corresponding sections in Chapter 6 are referred to in the following.

simulations needed considerably more calculation time and post-processing effort. However, at this stage FEM is still better suited as a universal tool for the tyre design process. This is mainly because of the greater flexibility regarding the handling of the tyre geometry and material data, and the ability to use basically the same FE model for different applications (e.g. static and dynamic calculations). WFEM, in contrast, is well suited for parameter studies where not the full capabilities of FEM are needed. This emphasises that WFEM is not competing with FEM; it is rather complementing it.

Numerical efficiency is also an important feature of the chosen time-domain tyre/road contact model, mostly because of the *a priori* knowledge of the influence matrix and the past displacements for each time step. Two important features of the contact formulation are its ability to account for the non-linear interaction between contact forces and displacements, and the use of contact springs to account for small-scale roughness effects.

The quality of the contact model is shown by the quasi-static simulations in *Paper I*, where good agreement of footprint predictions with FE results is obtained. The same results also show that the influence of the tyre load has to be taken into account when choosing an appropriate contact spring stiffness k . This is in addition to the possible dependence of k on the surface roughness.

For the rolling resistance study in *Paper III* an additional non-linear damping term was introduced into the contact algorithm. This allows to calculate losses due to small-scale tread deformations which showed to be of great significance for the rolling resistance on rougher surfaces.

In the same study the tyre and contact models were also extended to include tread pattern effects. In the tyre model a global mass and stiffness adjustment of the tread layer was used, while in the contact model the contact springs were adjusted locally. Using this approach instead of including the tread pattern in the tyre contour \mathbf{Z}_T in Eq. (4.29b), the requirements on the tyre resolution are kept reasonable. The validity of the approach is shown by the rolling resistance results in *Paper III*, where the influence of two different tread patterns is captured well.

For the radiation calculations a well established half-space boundary element method has been used [108]. Apart from the minor adaptations described in Section 4.4.3, no special modifications to the method are necessary.

Using the input power into the tyre, the rolling resistance can be calculated in a very efficient way; the necessary input quantities are already known from the contact calculations. Beneficial is the level of detail with which rolling losses can be analysed. In *Paper III* an analysis of the cross-sectional distribution of losses reveals how with increasing road roughness more dissipation occurs in the tread layer and less in the carcass. In [153] a frequency-wave order representation of rolling losses was instead used to analyse the influence of different tyre properties on the rolling resistance.

Compared to the results shown in [142], where rolling resistance was underestim-

ated by about 40 %, a significant improvement of the accuracy of rolling resistance calculations is achieved by two factors. Firstly, the use of non-proportional damping in the tyre model which allows for a more realistic distribution of losses between tread and carcass. Secondly, extending the contact model to account for the losses due to small-scale tread deformations by the road roughness asperities.

In conclusion, the presented methods have proven to be accurate and numerically efficient tools for the simulation of tyre vibrations, rolling noise and rolling resistance. Particularly useful are the easy post-processing, the many ways in which results can be presented and analysed, and the flexibility with which individual sub-modules can be altered or exchanged. Without these properties and the numerical efficiency some of the extended parameter studies in this thesis would not have been possible: 108 cases were calculated for the rolling noise/rolling loss calculations in *Paper II*, and 376 cases for the rolling resistance study in *Paper III*.

Besides showing that the proposed simulation tool can be successfully used for the prediction of rolling noise and rolling resistance, the appended papers also provide valuable insight into a number of relevant questions. The first of these relates to the necessary quality and quantity of road roughness input data for the contact simulations. It is generally undisputed that in rolling direction several meters of road roughness need to be scanned at a very small spacing (typically < 1 mm), and with a very high vertical resolution (typically micrometers). In contrast to this, there is a tendency to keep the number of parallel scan lines and the number of different scan locations on a particular road surface as low as possible to reduce the measurement effort. This raises the question of how representative a limited number of surface profile scans is for the whole surface. In *Paper II* it is shown that for typical road surfaces considerable differences exist between parallel scan lines which are taken at the same location. The road surface properties analysed in *Papers III* and *V* reveal that the same differences can be observed between scans for different locations on the surface. These surface property variations are directly reflected in the simulation results shown in *Papers II* and *V*. Notable variations in simulated rolling resistance and rolling noise are observed for simulations based on different road roughness scans of the same road surface². Therefore, it is recommended to calculate rolling noise and rolling resistance as the average of simulations for several road roughness scans taken from different locations on the road surface. Each of these scans should consist of a minimum of five or six unique lateral scan lines (*Paper II*). A lower number of lines is only acceptable if rolling loss calculations for very smooth surfaces are conducted (*Paper II*).

These findings can be related to *Paper III*, where it is shown that rolling resistance can be split into two parts: one part originating from the large-scale tyre structure deformations, and the other part arising from small-scale tread indent-

²Though not explicitly reported in *Paper III*, similar variations of rolling resistance could be observed in that study.

ations. The contribution of the tyre structure to the overall rolling resistance is nearly identical for all road surfaces. The losses due to small-scale tread deformations are highly texture dependent and vary between 0% and 50% of the overall losses. It follows that for smooth surfaces rolling resistance is mainly caused by a global deformation of the tyre structure, whereas for rougher surfaces significant contributions are made by local deformations of the tread due to the road roughness. This also explains why the calculation of rolling losses on smooth surfaces is less susceptible for local variations of the road surface roughness.

Another important question is in how far knowledge about car tyre vibrations and rolling noise is applicable to truck tyres as well. As a first step in an attempt to answer this question, the free wave propagation on a truck tyre up to 1 kHz was analysed in *Paper IV*. Compared to car tyres a more complex nature of wave motion is observed. Six main wave groups can be identified: semi-rigid body waves, waves with out-of-plane motion of the cross-section or the sidewalls only, waves with in-plane motion of the sidewalls, waves with combined in- and out-of-plane motion, fast out-of-plane belt extension waves, and finally waves characterised by strong tread layer deformations with limited or no motion of the tyre carcass. The last two types of waves have not been reported for car tyres. This, however, can only be partly explained by the structural differences between truck and car tyres. The typical car tyre study methodology and setup, and the considered frequency range make these waves also simply more difficult to identify for car tyres.

Explainable by structural differences between car and truck tyres are differences in the order and spacing of the semi-rigid body eigenforms, differences in the frequency of occurrence of particular waveforms, and a significant change in behaviour of the belt extension waveform. For the truck tyre this wave appears at lower frequencies than for the car tyre and only exists for the lowest wave orders. For higher orders the motion quickly changes to in-plane sidewall deformation.

As a final step the sound radiation for a rolling truck tyre was calculated and compared to measurements. The results are promising but a more thorough analysis and simulations for a larger selection of road surfaces are necessary before a substantiated assessment of truck tyre rolling noise is possible.

To summarise, the proposed simulation tool has successfully been used to calculate the vibrations, rolling resistance and rolling noise of car and truck tyres. There is good agreement between simulations and measurements of rolling resistance and rolling noise, making this the first tool which can be successfully used for the simulation of both rolling resistance and rolling noise. The method has proven to be exceptionally suitable for extended parameter studies because it combines good accuracy with reasonable calculation times and fast post-processing. New light could be shed on questions relating to the dependence of car tyre rolling resistance on road roughness and tread pattern, the free wave propagation on truck tyres, and the influence of road roughness input data on simulations of rolling resistance and rolling noise.

7.2 Future work

The presented tyre/road interaction model has been developed with the long term goal of providing a reliable, easy to use, efficient, and flexible tool for the calculation of tyre vibrations, rolling resistance and rolling noise. While the tool is at a development stage where it can successfully be used for many of the intended purposes, some uncertainties and room for improvement remain. The most important open questions and possible next steps can be summarised as follows:

- Straightforward is to include the rim in the tyre model in order to increase the low-frequency accuracy. The additional computational effort should be negligible.
- The question of appropriate material input data for the tyre model is probably the biggest challenge. The WFE model is too detailed to determine material parameters without direct input from the tyre manufacturer. Even if tyre design data is provided, the suitability of material values is unknown. The stiffness property of the viscoelastic parts of the tyre is extremely sensitive to temperature, frequency and strain conditions. Although specific constant values of these properties may be *a priori* chosen, this will always be some sort of compromise, depending on the nature of the excitation and the environmental conditions, see *Paper I*. For the model of the 315/80 R22.5 truck tyre already a simplified frequency dependency of viscoelastic properties was assumed. Further steps in this direction might be needed to account for the difference in material properties caused by the varying operating conditions for free and forced response, footprint analysis, or rolling.
- The chosen contact spring stiffness has a large influence on the tyre/road interaction. The current way of determining the stiffness based on the simulated footprint size seems overly simplified. Also, at the moment only linear springs are used. This neglects the change in real contact area during contact. In [97] non-linear contact springs are used to account for this. However, this requires very detailed road surface data to determine the spring characteristics. In *Paper III* a strong correlation between rolling resistance, especially the small-scale tread deformation related part, and the minimum profile depth *MPD* of the road surface was found. It seems conceivable that contact stiffnesses for different surfaces can possibly be related to the *MPD* of the surfaces. Additionally, also the relation between contact spring stiffness and static load needs to be better understood.
- So far only normal contact is considered. A logical step is to extend the contact model to include tangential contact forces. This has been partly done in [75]; yet, without including tangential contact springs or damping.

- Regarding the numerical effort the radiation module is the bottleneck of the calculations: depending on circumstances, two-thirds or more of the total calculation time are spend for the BEM. A speed increase would open new possibilities for rolling noise related parameter studies. It is, however, not believed that a substantial speedup can be achieved without a significant rewrite of the BEM code, e.g. in the form of a fast-multipole BEM [110].
- In this thesis only the reflection from a perfectly rigid ground has been considered. The original implementation of the half-space BEM in [108] includes formulations for different ground impedances. Assuming there is access to acoustic impedance measurements for road surfaces, this feature could be used to simulate rolling noise for newer absorbing road surfaces.
- For traditional road surfaces the rolling loss calculations might benefit from a scaling of the contact stiffness with the road roughness. The results for rubberised surfaces presented in *Paper III* indicate that for these surfaces one or more contributing mechanisms are missing from the simulations, e.g. adhesion, friction, or the elasticity of the road. A precise assessment of possible reasons for the mismatch needs a broader set of data and should include simulations for newer rubberised surfaces which have been reported to have rolling resistance more equal to traditional surfaces.
- The tread pattern has so far only been accounted for in the rolling resistance calculations in *Paper III*. Considering the importance of the tread impact for rolling noise generation the obvious next task is to investigate whether the proposed method for including tread pattern effects also can be applied to simulations of tyre/road noise.

On goal of the thesis was to gain knowledge about the physical processes (e.g. in terms of source localisation, or identification of vibration patterns which are strong contributors to sound radiation), and the differences and commonalities between truck and car tyre rolling noise. The first steps towards this goal have been taken in *Papers IV* and *V*. The tyre/road noise model from *Paper V* needs to be further verified by calculating rolling noise for more road surfaces for which measurements, preferably also in the far field, exist. After this, the contribution of the different waves to the sound radiation from a rolling truck tyre should be investigated in a similar way as was done for car tyre rolling noise in [76].

Finally, tyre development is always driven by a multitude of difference performance criteria. Some examples besides rolling noise and rolling resistance include handling, wet traction, wear, ride quality, etc. Usually none of these criteria can be considered independently from the others. In view of this, it might be desirable to develop a single tool which can predict the influence of for example changes in tyre structure on some or all of these criteria. With the tool presented in this

thesis this is already possible for rolling noise and rolling resistance. This has for example been used in *Paper II* or [153]. The modular nature of the proposed tool makes it relatively easy to add additional sub-modules. Accordingly, it might be possible to include simulations of other performance criteria such as wear.

A Implemented tyre models

Throughout this thesis WFE models of the three tyres shown in Fig. A.1 are used: a slick 205/55 R16 car tyre, a 175/65 R14 car tyre, and a 315/80 R22.5 truck tyre with circumferential grooves. The models are described in the following.

A.1 205/55 R16 car tyre

This is a slick Continental 205/55 R16 tyre, see Fig. A.1a. The WFE mesh is shown in Fig. 4.3. It consists of 46 shell elements for the sidewalls and belt, and 20 solid elements for the tread. As no data on damping properties was provided, loss factors are determined manually. Based on half-power bandwidth estimations in a measured input mobility, loss factors can be estimated below 300 Hz. Values outside this region are determined by matching simulated mobilities to measured ones. This also gives the distribution of losses between solid and shell elements for non-proportional damping. The resulting loss factors for both damping models are shown in Fig. A.2. The remaining material data was provided by the manufacturer, details about it can be found in [74], where the model is also validated against measured mobilities. The tyre is used for the study in *Paper II*. In Section 6.3 and *Paper III* versions of this tyre are used which are adjusted to account for the influence of different tread patterns on tread mass and stiffness.



(a) 205/55 R16



(b) 175/65 R14



(c) 315/80 R22.5

Fig. A.1 The three tyres modelled in this thesis.

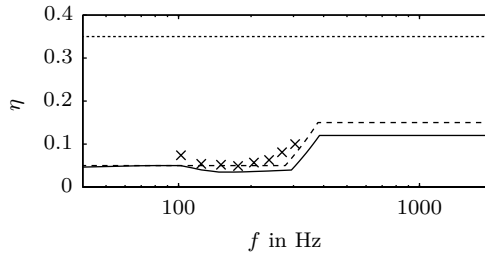


Fig. A.2 Loss factors for the 205/55 R16 tyre. Proportional damping (---), non-proportional damping shell (—) and solid (···) elements. Results from half-power bandwidth measurements marked by \times .

A.2 175/65 R14 car tyre

This is a Continental 175/65 R14 T XL tyre. The tread pattern is characterised by three prominent circumferential grooves, see Fig. A.1b. The cross-sectional mesh with 37 shell and 12 solid elements is shown in Fig. A.3. Frequency-dependent proportional damping based on measurement data is implemented. From half-power bandwidth evaluations of the first five resonance peaks in the measured input mobility the loss factor for low frequencies is estimated. Additionally modal damping data is available for the frequency range up to 500 Hz. After further adjustment to give better match between measured and simulated mobilities, the loss factor is obtained as shown in Fig. A.4. Further details about the input data and an extensive validation against measured mobilities can be found in [142]. This tyre is used in *Papers I* and *II*, and Sections 6.1 and 6.2.

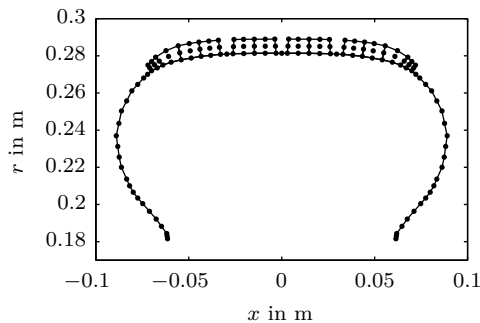


Fig. A.3 WFEM mesh of the 175/65 R14 tyre with 37 shell and 12 solid elements. Each \bullet represents one node.

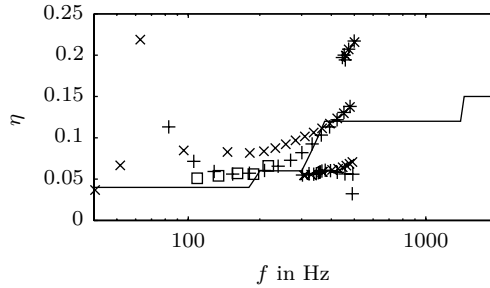


Fig. A.4 Loss factor data for the 175/65 R14 tyre as obtained from the half-power bandwidth method (\square), as obtained as modal damping for modes with even (\times), or odd ($+$) numbers of half wave lengths over the cross-section, and as used for proportional damping in WFEM ($—$).

A.3 315/80 R22.5 truck tyre

The considered tyre is a Continental 315/80 R22.5 model with circumferential grooves (“airplane profile”) as shown in Fig. A.1c. It is used for the studies presented in *Papers IV* and *V*, and Sections 6.4 and 6.5.

Geometry and bulk material data for 20 °C were provided by the manufacturer. The cross-sectional mesh is shown in Fig. A.5. Contrary to the two car tyres the bulk of the tyre is not modelled using shell elements but 126 solid elements, 65 shell elements are only used for the ply. The preferred use of solid elements is motivated by a better representation of the thicker truck tyre geometry, and a reduced need to determine material parameters for elements encompassing several material groups. The inflation pressure is 670 kPa; it is included as ply pre-tension. The frequency-dependent loss factor for proportional damping is shown in Fig. A.6. It is based on half-power bandwidth estimations and optimisation of simulated mobilities. Based on data on dynamic viscoelastic material behaviour, Young’s moduli for rubber materials are, slightly simplified, assumed to be frequency dependent below 200 Hz. For higher frequencies constant values are used. Due to material changes during tyre curing and uncertainties in the material parameter condensation process, a manual adjustment of the radial extensional and lateral shear stiffness terms is necessary in the belt region. The shell pre-tension is furthermore increased by 30% in lateral direction and reduced by 20% in circumferential direction. The resulting pre-tension is shown in see Fig. A.7.

In order to validate the truck tyre model, simulated and measured point and transfer mobilities $Y(\omega)$ are compared. The general measurement setup is identical to the one for the 175/65 R14 car tyre described in [142, Appendix C]. A shaker fed with band-limited white noise was used to excite the tyre via a 16 mm \times 16 mm

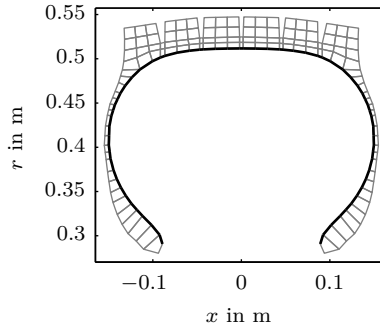


Fig. A.5 WFEM mesh of the 315/80 R22.5 tyre with 65 shell (black) and 126 solid elements (gray).

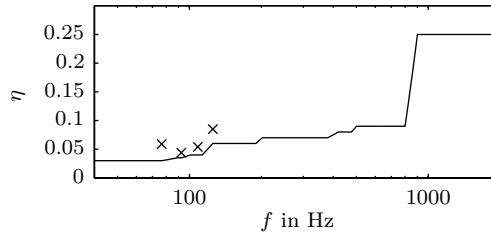


Fig. A.6 Loss factors for proportional damping for the 315/80 R22.5 tyre. Results from half-power bandwidth measurements marked by \times .

aluminium plate glued to one of the centre tread bands. A force transducer was mounted between shaker and plate, and accelerometers were used to pick up the tyre response at several positions over the tyre width and circumference. Mobilities are simulated using Eq. (4.12) for a uniform pressure acting over the same region as the aluminium plate in the measurements. Some examples of measured and simulated mobilities are given in Figures A.8 and A.9.

Two differences in boundary conditions between measurements and simulations affect the lowest frequencies in Figures A.8 and A.9. Firstly, the wheel mass is not included in the simulations. Secondly, due to difficulties in realising a truly clamped rim condition for the heavy truck tyre, measurements were conducted on a freely suspended tyre. As a consequence the peak at 60 Hz is not visible in the measurements. This peak corresponds to the translational semi-rigid body motion shown in Fig. 6.16c, which is discussed in detail in Section 6.4.2.

For frequencies above 70 Hz the agreement of the simulated radial input mobility to the measured one is excellent apart from the region from 150 Hz to 200 Hz,

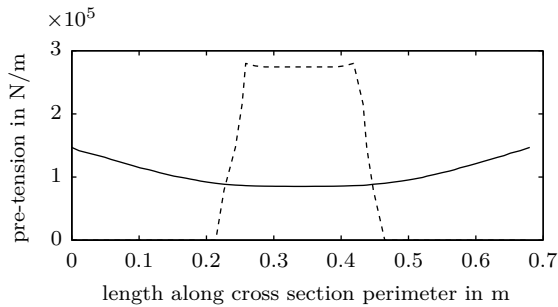


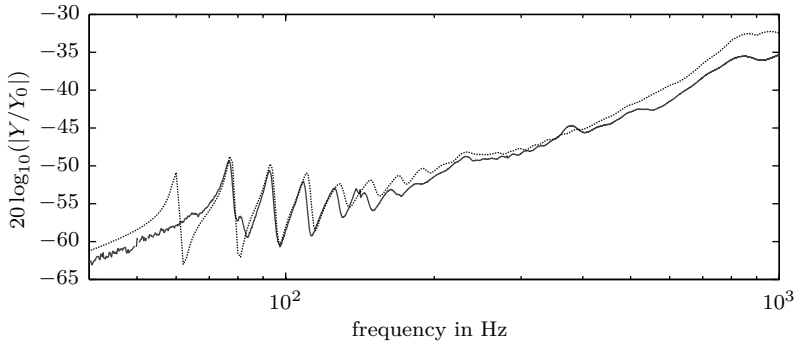
Fig. A.7 Lateral (—) and circumferential (---) pre-tension along the tyre cross-section.

where frequencies and amplitudes are slightly overestimated in the simulations, see Fig. A.8a. Above 400 Hz the amplitude is again overestimated. The effect is explained by differences in local excitation between a glued plate (measurements) and a uniform pressure (simulations) [74]. The local nature of this effect can be confirmed by a comparison of the real part of the input mobilities as this quantity is less sensitive to local deformations. This is done in Fig. A.8b, where very good agreement of amplitudes is achieved also for medium to high frequencies.

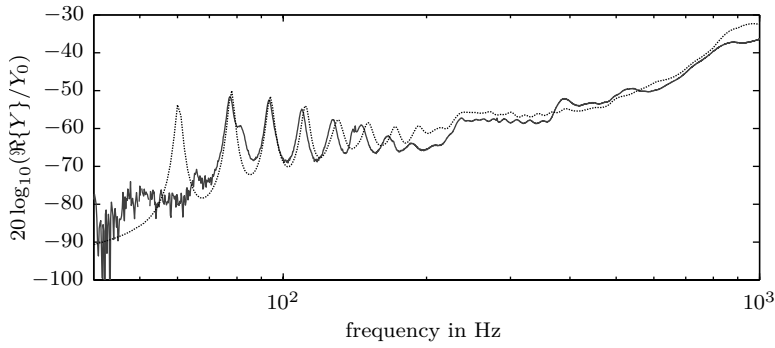
Fig. A.8c shows the real part of the tangential input mobility. This quantity is mostly dependent on the Young's modulus of the tread rubber. Agreement is generally good. In the mid-frequency region a frequency- and amplitude-shift is observed, and the anti-resonance around 490 Hz is missing from the simulation. This is most likely due to neglecting the influence of the aluminium plate and the attached transducers in the simulations, cf. [154]. The assumption of a frequency-independent Young's modulus above 200 Hz might also be too simplified.

In Fig. A.9 results for transfer mobilities are shown. The response at a point at some distance away from the excitation is given by the superposition of a multitude of difference waves propagating through the tyre structure. A precise prediction of the response, especially if it is far away from the excitation, is only possible if the amplitude and phase speed of each of these waves are modelled accurately. In view of this, the results in Fig. A.9 are very satisfying. For low frequencies measured and simulated mobilities generally agree very well. For higher frequencies most of the features of the measured mobilities can be recognised in the simulations as well, albeit with small frequency and/or amplitude shifts. Average orders of response magnitude agree very well over the whole frequency region.

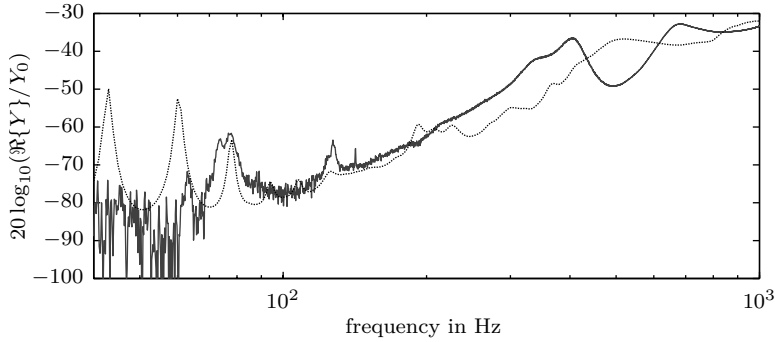
In conclusion, a good general agreement between simulated and measured mobilities is achieved. This indicates that the tyre model and the chosen material values adequately represent the chosen tyre.



(a) magnitude radial input mobility



(b) real part radial input mobility



(c) real part tangential input mobility

Fig. A.8 Comparison of input mobilities from measurements (—) and simulations (···). $Y_0 = 1 \text{ N}(\text{ms})^{-1}$.

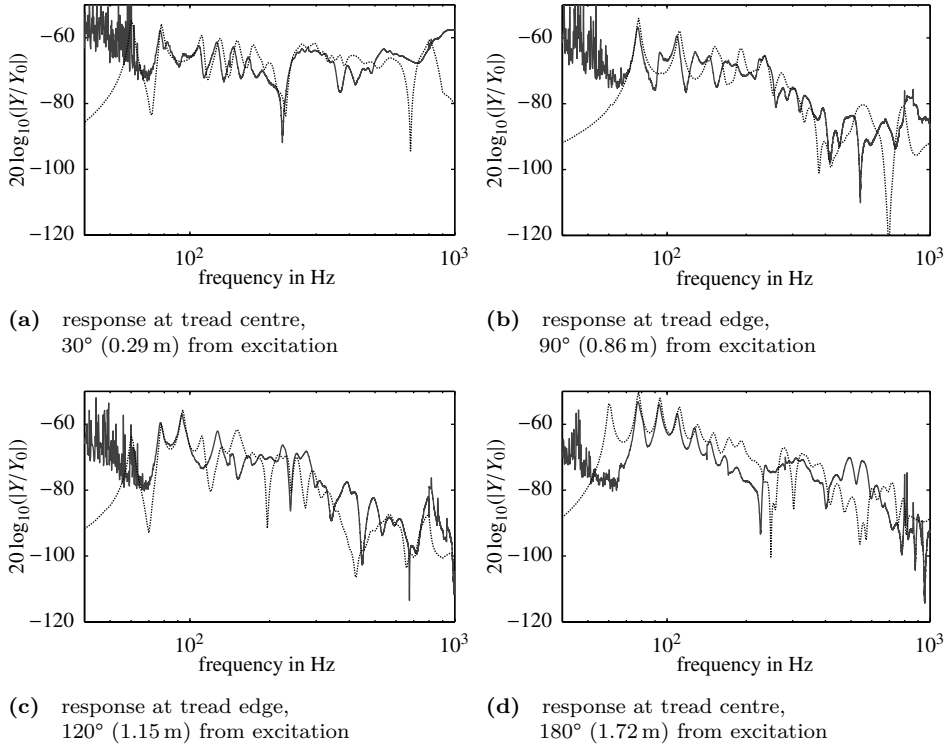


Fig. A.9 Comparison of magnitude of radial transfer mobilities from measurement (—) and simulations (···). $Y_0 = 1 \text{ N}(\text{ms})^{-1}$.

B Simulation configurations

In the following Tables B.1 to B.4 the most important simulation parameters for the studies presented in thesis are given. For the sake of brevity the studies are only referred to by the paper they pertain to. The same settings also apply to the corresponding sections from Chapter 6 unless otherwise noted.

Used abbreviations: circ. – circumferential, cross-sect. – cross-section, elem. – elements, infl. – inflation, lat. – lateral, resp. – response

Tab. B.1 General simulation parameters.

| study | tyre | infl. pressure in kPa | tread pattern |
|------------------|---|--------------------------|------------------|
| <i>Paper I</i> | 175/65 R14 | 200 | no |
| <i>Paper II</i> | 175/65 R14 , 205/55 R16 ¹ | 200 200 | no no |
| <i>Paper III</i> | 205/55 R16 | 200 | yes |
| <i>Paper IV</i> | 315/80 R22.5 | 670 | no |
| <i>Paper V</i> | 315/80 R22.5 | 670 | no |

¹ Not included in Section 6.2.

Tab. B.2 Parameters for the WFE tyre model.

| study | no. of circ. segments | N in Eqs. (4.18)/(4.22) | S in Eq. (4.18) | damping model | forced resp. solver |
|------------------------------|--------------------------|------------------------------|----------------------|------------------|------------------------|
| <i>Paper I</i> | 512 | 420 | 150 | prop. | modal |
| <i>Paper II</i> | 512 | 250 | 100 | prop. | modal |
| <i>Paper III</i> | 1024 | 256 | - | non-prop. | direct |
| <i>Paper IV</i> ¹ | 912 | 456 | 50 | prop. | modal |
| <i>Paper V</i> | 912 | 456 | 50 | prop. | modal |

¹ Only relevant for the forced response calculations which are not included in Section 6.4.

Tab. B.3 Parameters for tyre/road interaction. *Paper IV* not shown as there is no tyre/road interaction in that particular study.

| study | axle load in N | speed in km/h | no. of lat. contact tracks | k in N/m | c in Ns/m ² |
|------------------|-------------------|------------------|-------------------------------|-------------------|-----------------------------|
| <i>Paper I</i> | varying | 0 | 12 | $5.00 \cdot 10^4$ | 0.00 |
| <i>Paper II</i> | 3415 | 80 | 12/10 ¹ | $5.00 \cdot 10^4$ | 0.00 |
| <i>Paper III</i> | 4100 | 80 | 20 | $1.25 \cdot 10^4$ | 3.25 |
| <i>Paper V</i> | 19620 | 60 | 18 | $1.25 \cdot 10^4$ | 0.00 |

¹ 175/65 R14 respectively 205/55 R16 tyre.

Tab. B.4 Parameters for the BEM calculations.

| study | no. of elem. over cross-sect. | no. of circ. segments | max circ./ cross-sect. order | tyre lift in mm | CHIEF points |
|-----------------|----------------------------------|--------------------------|---------------------------------|--------------------|-----------------|
| <i>Paper II</i> | 39/38 ¹ | 128 | 24/20 | 1 | 11 |
| <i>Paper V</i> | 77 | 152 | 50/50 | 1 | 12 |

¹ 175/65 R14 respectively 205/55 R16 tyre.

C Reference frames and coordinate systems

C.1 Reference frames

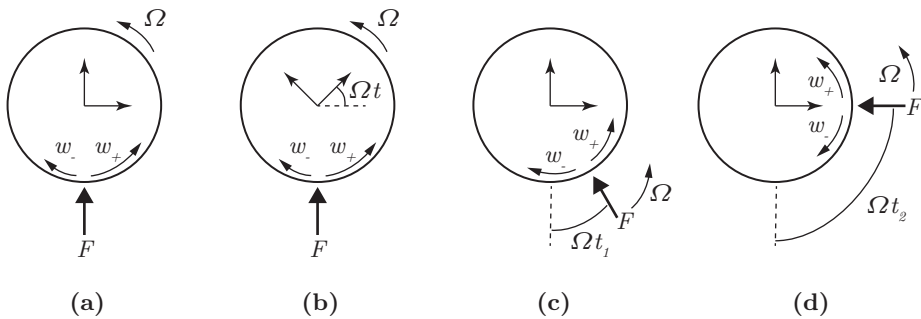


Fig. C.1 The Euler and Lagrange reference systems for a tyre rotating at an angular speed Ω . (a) Euler reference system, (b) Lagrange reference system as seen by external observer, (c) and (d) Lagrange reference system at two different times t_1 and t_2 as seen by an internal observer.

For all questions relating to the kinematics of bodies, it is essential in which way the reference system is defined in which the physical processes are observed. Generally, there are two options: the first one is the Euler reference system in which the position of an external observer is assumed who observes the body moving through space. The second alternative is the Lagrange reference system in which the observer is moving with the body and in which all exterior objects and events are observed as moving relative to the body.

In Fig. C.1 the difference between the two systems is exemplified for the case of a tyre rotating at an angular speed Ω . It is assumed that the tyre is in contact with the ground; the resulting force F excites waves w_+ propagating in the direction of rotation, and waves w_- propagating against the direction of rotation. In the Euler reference system, case (a) in Fig. C.1, the force is observed as stationary and the tyre is rotating. This rotation leads to the Doppler effect: the wave lengths

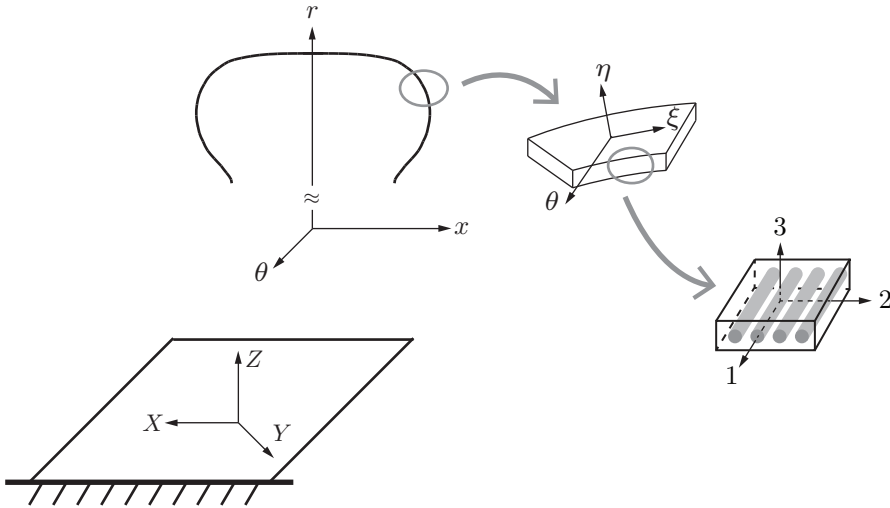


Fig. C.2 Overview of the different coordinate systems.

of waves travelling in (against) the direction of rotation get longer (shorter). In case (b), the Lagrangian reference system is depicted as it is seen by an outside observer. The coordinate system rotates with the tyre, so that at a time t , it is rotated by Ωt from the initial position. Because this is just an outside view of the Lagrangian system, the Doppler effect is still observed. In (c) and (d) the position of an observer inside the Lagrangian reference system at two different time t_1 and t_2 is taken. In this system the tyre does not rotate, instead the force F moves around the tyre. At every different time instant the waves w_+ and w_- are excited at a different position along the tyre circumference. Because the tyre is at rest, the medium of wave propagation also does not move anymore. There is no Doppler effect.

C.2 Coordinate systems

Throughout the different stages of the tyre simulations several coordinate systems are used. As each of them is introduced one at a time in separate parts of this report, it is useful to present all of them in a condensed form in a common context to avoid confusion. All used coordinate systems are shown in Fig. C.2 and can be described as follows:

(X, Y, Z) This is the global cartesian coordinate system in an Eulerian reference frame, i.e. the ground is fixed and the tyre rotates in space. It is used for

modelling the tyre/road interaction and the radiation.

(x, r, θ) This is a cartesian coordinate system affixed to the tyre. Its origin is placed in the wheel centre and it rotates with the tyre, i.e. it lies in a Lagrangian reference frame. All WFE modelling is performed in this coordinate system. The relation between the (x, r, θ) system and an (X, Y, Z) Eulerian system with origin at the wheel centre is

$$\begin{bmatrix} x \\ r \\ \theta \end{bmatrix} = \begin{bmatrix} -1 & 0 & 0 \\ 0 & \cos \Omega t & \sin \Omega t \\ 0 & -\sin \Omega t & \cos \Omega t \end{bmatrix} \begin{bmatrix} X \\ Y \\ Z \end{bmatrix}. \quad (\text{C.1})$$

Here, Ω is the rotational speed of the tyre and t the time.

(ξ, η, θ) The curvilinear coordinate system of an individual condensed waveguide finite element or shell-like individual material layer in the laminate. It is used during the WFE modelling and the derivation of the tyre's material properties. Transformations between this coordinate system and the (x, r, θ) system are a fundamental part of the WFEM formulations [72].

(1, 2, 3) Material coordinate system for a fibrous composite (i.e. the belt or ply layer) which aligns with the composite's principal axes of orthogonality. More specifically, the 1-axis is along the cord direction, the 2-axis is the in-plane normal to the cord direction and the 3-axis is the out-of-plane direction. It is used during the estimation of the material properties to derive the stress-strain relations in the principal material axes of a fibrous composite layer. The stress-strain relationship in (ξ, η, θ) coordinates then follows from (5.17).

References

- [1] Annual European Community greenhouse gas inventory 1990–2006 and inventory report 2008, Technical Report No 6/2008, European Environment Agency, 2008.
- [2] Inventory of U.S. greenhouse gas emissions and sinks: 1990 – 2008, Report EPA 430-R-10-006, U.S. Environmental Protection Agency, 2010.
- [3] Verkehrsverflechtungsprognose 2030, Final report 96.0981/2011, German Federal Ministry of Transport and Digital Infrastructure, 2014.
- [4] J. Barrand, J. Bokar, Reducing tire rolling resistance to save fuel and lower emissions, SAE International Journal of Passenger Cars – Mechanical Systems 1 (2009) 9–17.
- [5] Tires and Passenger Vehicle Fuel Economy: Informing Consumers, Improving Performance, TRB Special Report 286, Transportation Research Board, 2006.
- [6] G. Fontaras, Z. Samaras, On the way to 130 g CO₂/km—Estimating the future characteristics of the average European passenger car, Energy Policy 38 (2010) 1826–1833.
- [7] N. Demirdöven, J. Deutch, Hybrid cars now, fuel cell cars later, Science 305 (2004) 974–976.
- [8] Burden of disease from environmental noise — Quantification of healthy life years lost in Europe, Report, WHO, 2011.
- [9] T. Kihlman, W. Kropp, W. Lang, Quieter Cities of the Future, Technical Report, International Institute of Noise Control Engineering, CAETS, 2014.
- [10] L. den Boer, A. Schrotten, Traffic noise reduction in Europe, Technical Report 07.4451.27, CE Delft, 2007.
- [11] W. van Keulen, M. Duškov, Inventory study of basic knowledge on tyre/road noise, Project report DWW-2005-022, IPG, 2005.
- [12] U. Sandberg, J. Ejsmont, Tyre/road noise reference book, Informex, Kisa, Sweden, 2002.

-
- [13] Regulation (EC) No 1222/2009 of the European Parliament and of the Council of 25 November 2009 on the labelling of tyres with respect to fuel efficiency and other essential parameters, Official Journal L 342, 22/12/2009.
- [14] UNECE - United Nations Economic Commission for Europe, Regulation no. 117 - uniform provisions concerning the approval of tyres with regard to rolling sound emissions and to adhesion on wet surfaces and/or to rolling resistance, 2011.
- [15] International Organization for Standardization ISO 18164:2005 Passenger car, truck, bus and motorcycle tyres — Methods of measuring rolling resistance, 2005.
- [16] A. Gent, J. Walter (Eds.), The pneumatic tire, U.S. Department of Transportation, National Highway Traffic Safety Administration, 2006.
- [17] D. Hall, J. Moreland, Fundamentals of rolling resistance, Rubber Chemistry and Technology 74 (2001) 525–539.
- [18] A. Nashif, D. Jones, J. Henderson, Vibration damping, Wiley-Interscience, New York, 1985.
- [19] H. Bendtsen, Rolling resistance, fuel consumption and emissions: A literature review, SILVIA Project Report SILVIA-DTF-ATKINS-007-02-WP3-060204, Danish Road Institute, 2004.
- [20] S. Boere, I. Lopez, A. Kuijpers, H. Nijmeijer, Prediction of road texture influence on rolling resistance and tyre/road noise, in: Proceedings of Euronoise 2009, Edinburgh, United Kingdom, 2009 October 26-28.
- [21] S. Bandyopadhyay, A. Chandra, R. Mukhopadhyay, An overview of tyre rolling loss, Progress in rubber and plastics technology 10 (1994) 20–53.
- [22] International Committee for Weights and Measures, The International System of Units (SI), 2006.
- [23] A. Kuijpers, Further analysis of the Sperenberg data — Towards a better understanding of the processes influencing tyre/road noise, Technical Report M+P.MVM.99.3.1, M+P - consulting engineers, 2001.
- [24] K. Mak, W. Hung, S. Lee, Exploring the impacts of road surface texture on tyre/road noise — A case study in Hong Kong, Transportation Research Part D: Transport and Environment 17 (2012) 104 – 107.
- [25] M. Heckl, Tyre noise generation, Wear 113 (1986) 157–170.

-
- [26] P. Dinkova, Truck tyre vibration behaviour — Measurements and high frequency modelling, Licentiate thesis, Chalmers University of Technology, Gothenburg, 2006.
- [27] P. Andersson, K. Larsson, F. Wullens, W. Kropp, High frequency dynamic behaviour of smooth and patterned passenger car tyres, *Acta Acustica united with Acustica* 90 (2004) 445–456.
- [28] R. Pinnington, A. Briscoe, A wave model for a pneumatic tyre belt, *Journal of Sound and Vibration* 253 (2002) 941–959.
- [29] K. Larsson, W. Kropp, A high-frequency three-dimensional tyre model based on two coupled elastic layers, *Journal of Sound and Vibration* 253 (2002) 889–908.
- [30] T. Sakata, H. Morimura, H. Ide, Effects of tire cavity resonance on vehicle road noise, *Tire Science and Technology* 18 (1990) 68–79.
- [31] A. Jessop, J. Bolton, Tire surface vibration and sound radiation resulting from the tire cavity mode, *Tire Science and Technology* 39 (2011) 245–255.
- [32] D. Ronneberger, Experimentelle und theoretische Untersuchung spezieller Mechanismen der Rollgeräuschenstehung und -abstrahlung, *Mitteilung* 57, Institut für Straßen-, Eisenbahn- und Felsbau der E.T.H. Zürich, 1984.
- [33] N. Nilsson, O. Bennerhult, S. Söderqvist, Air-resonant radiation — A possible mechanism for high frequency noise from cross-bar tires, IFM Research Report 6.084.02, IFM Akustikbyrån AB, 1979.
- [34] W. Kropp, F.-X. Becot, S. Barrelet, On the sound radiation from tyres, *Acta Acustica united with Acustica* 86 (2000) 769–779.
- [35] R. Graf, C.-Y. Kuo, A. Dowling, W. Graham, On the horn effect of a tyre/road interface, part I: Experiment and computation, *Journal of Sound and Vibration* 256 (2002) 417–431.
- [36] E.-U. Saemann, H. Schmidt, Schallmessungen bei der Entwicklung von Reifen mit geringem Vorbeifahrtpegel, *Zeitschrift für Lärmbekämpfung* 49 (2002) 59–62.
- [37] J. Ejsmont, Tire/road noise and rolling resistance — Is there a trade-off?, in: U. Sandberg (Ed.), *International Tire/Road Noise Conference 1990 (INTROC 90)*, 8-10 August 1990, Gothenburg, Sweden, volume 1, pp. 439–452.

-
- [38] U. Sandberg, J. Ejsmont, Noise emission, friction and rolling resistance of car tires — Summary of an experimental study, in: Proceedings of the 2000 National Conference on Noise Control Engineering (NOISE-CON 2000), Dec. 3-5, Newport Beach, USA.
- [39] R. Stenschke, P. Vietzke, Noise and use characteristics of modern car tyres (State of the art), in: Seventh International Congress on Sound and Vibration, 4-7 July 2000, Garmisch-Partenkirchen, Germany, pp. 2781–2788.
- [40] O. Bschorr, A. Wolf, Reifenschwingungen als Ursache von Lärm und Rollwiderstand, *Automobil-Industrie* 27 (1982) 451–458.
- [41] A. Miège, A. Popov, The rolling resistance of truck tyres under a dynamic vertical load, *Vehicle System Dynamics: International Journal of Vehicle Mechanics and Mobility* 43 (2005) 135–144.
- [42] M. Fraggstedt, Vibrations, damping and power dissipation in car tyres, Ph.D. thesis, KTH Royal Institute of Sciences, Stockholm, 2008.
- [43] G. Descornet, U. Sandberg, Road surface influence on tire/road noise — Part II, in: Proceedings Internoise 80, Miami, USA, 8-10 December, 1980, pp. 267–272.
- [44] U. Sandberg, G. Descornet, Road surface influence on tire/road noise — Part I, in: Proceedings Internoise 80, Miami, USA, 8-10 December, 1980, pp. 259–266.
- [45] T. Beckenbauer, A. Kuijpers, Prediction of pass-by levels depending on road surface parameters by means of a hybrid model, in: [155], pp. 2611–2616.
- [46] A. Kuijpers, G. van Blokland, Tyre/road noise models in the last two decades: a critical evaluation, in: [155].
- [47] F. Böhm, Mechanik des Gürtelreifens, *Archive of Applied Mechanics* 35 (1966) 82–101.
- [48] L. Kung, W. Soedel, T. Yang, Free vibration of a pneumatic tire-wheel unit using a ring on an elastic foundation and a finite element model, *Journal of Sound and Vibration* 107 (1986) 181–194.
- [49] W. Kropp, Structure-borne sound on a smooth tyre, *Applied Acoustics* 26 (1989) 181–192.
- [50] P. Kindt, P. Sas, W. Desmet, Development and validation of a three-dimensional ring-based structural tyre model, *Journal of Sound and Vibration* 326 (2009) 852 – 869.

-
- [51] A. Tsotras, On the interaction between modal behaviour and contact force development of a pneumatic tyre, Ph.D. thesis, Loughborough University, 2010.
- [52] F. Wullens, Excitation of tyre vibrations due to tyre/road interaction, Ph.D. thesis, Chalmers University of Technology, Gothenburg, 2004.
- [53] Y. Kim, J. Bolton, Modelling tyre treadband vibration, in: [155].
- [54] J. Muggleton, B. Mace, M. Brennan, Vibrational response prediction of a pneumatic tyre using an orthotropic two-plate wave model, *Journal of Sound and Vibration* 264 (2003) 929–950.
- [55] D. O’Boy, A. Dowling, Tyre/road interaction noise — Numerical noise prediction of a patterned tyre on a rough road surface, *Journal of Sound and Vibration* 323 (2009) 270 – 291.
- [56] R. Pinnington, Radial force transmission to the hub from an unloaded stationary tyre, *Journal of Sound and Vibration* 253 (2002) 961–983.
- [57] R. Pinnington, A wave model of a circular tyre. Part 1: belt modelling, *Journal of Sound and Vibration* 290 (2006) 101–132.
- [58] R. Pinnington, A wave model of a circular tyre. Part 2: side-wall and force transmission modelling, *Journal of Sound and Vibration* 290 (2006) 133–168.
- [59] C. Lecomte, W. Graham, M. Dale, A shell model for tyre belt vibrations, *Journal of Sound and Vibration* 329 (2010) 1717–1742.
- [60] Y. Chang, T. Yang, W. Soedel, Dynamic analysis of a radial tire by finite elements and modal expansion, *Journal of Sound and Vibration* 96 (1984) 1–11.
- [61] S. Saigal, T. Yang, H. Kim, W. Soedel, Free vibrations of a tire as a toroidal membrane, *Journal of Sound and Vibration* 107 (1986) 71–82.
- [62] T. Richards, Finite element analysis of structural-acoustic coupling in tyres, *Journal of Sound and Vibration* 149 (1991) 235–243.
- [63] M. Brinkmeier, U. Nackenhorst, H. Volk, A finite element approach to the transient dynamics of rolling tires with emphasis on rolling noise simulation, *Tire Science and Technology* 35 (2007) 165–182.
- [64] A. Pietrzyk, Prediction of the dynamic response of a tyre, in: [155].
- [65] A. Fadavi, D. Duhamel, H. Yin, Tyre/road noise: finite element modelling of tyre vibrations, in: [155].

-
- [66] I. Lopez, R. Blom, N. Roozen, H. Nijmeijer, Modelling vibrations on deformed rolling tyres—a modal approach, *Journal of Sound and Vibration* 307 (2007) 481–494.
- [67] I. Lopez, Influence of material damping on the prediction of road texture and tread pattern related rolling resistance, in: P. Sas, B. Bergen (Eds.), *Proceedings of the International Conference on Noise and Vibration Engineering ISMA 2010*, Katholieke Universiteit Leuven, Belgium, pp. 4039–4052.
- [68] M. Brinkmeier, U. Nackenhorst, S. Petersen, O. von Estorff, A finite element approach for the simulation of tire rolling noise, *Journal of Sound and Vibration* 309 (2008) 20–39.
- [69] J. Biermann, O. von Estorff, S. Petersen, H. Schmidt, Computational model to investigate the sound radiation from rolling tires, *Tire Science and Technology* 35 (2007) 209–225.
- [70] J. Schutte, Numerical Simulation of Tyre/Road Noise, Ph.D. thesis, University of Twente, Enschede, The Netherlands, 2011.
- [71] C.-M. Nilsson, Waveguide finite elements applied on a car tyre, Ph.D. thesis, KTH Royal Institute of Sciences, Stockholm, 2004.
- [72] S. Finnveden, M. Fraggstedt, Waveguide finite elements for curved structures, *Journal of Sound and Vibration* 312 (2008) 644–671.
- [73] E. Rustighi, S. Elliott, S. Finnveden, K. Gulyás, T. Mócsai, M. Danti, Linear stochastic evaluation of tyre vibration due to tyre/road excitation, *Journal of Sound and Vibration* 310 (2008) 1112–1127.
- [74] P. Sabiniarz, W. Kropp, A waveguide finite element aided analysis of the wave field on a stationary tyre, not in contact with the ground, *Journal of Sound and Vibration* 329 (2010) 3041–3064.
- [75] P. Sabiniarz, Modelling the vibrations on a rolling tyre and their relation to exterior and interior noise, Ph.D. thesis, Chalmers University of Technology, Gothenburg, 2011.
- [76] W. Kropp, P. Sabiniarz, H. Brick, T. Beckenbauer, On the sound radiation of a rolling tyre, *Journal of Sound and Vibration* 331 (2012) 1789–1805.
- [77] Y. Waki, B. Mace, M. Brennan, Free and forced vibrations of a tyre using a wave/finite element approach, *Journal of Sound and Vibration* 323 (2009) 737–756.

-
- [78] Y. Waki, B. Mace, M. Brennan, Numerical issues concerning the wave and finite element method for free and forced vibrations of waveguides, *Journal of Sound and Vibration* 327 (2009) 92–108.
- [79] D. Duhamel, S. Erlicher, H. Nguyen, A recursive finite element method for computing tyre vibrations, *European Journal of Computational Mechanics* 20 (2011) 9–27.
- [80] W. Reiter, A. Eberhardt, L. Harper, Truck tire vibration/noise, in: INTER-NOISE and NOISE-CON Congress and Conference Proceedings, NoiseCon73, Washington DC, pp. 202–205.
- [81] A. Eberhardt, Truck tire vibration sound, in: INTER-NOISE and NOISE-CON Congress and Conference Proceedings, InterNoise80, Miami, pp. 281–284.
- [82] A. Eberhardt, Source identification of the noise from non-stationary truck tire vibration and sound, in: INTER-NOISE and NOISE-CON Congress and Conference Proceedings, NoiseCon81, Raleigh, USA, pp. 43–48.
- [83] R. Keltie, Analytical model of the truck tire vibration sound mechanism, *The Journal of the Acoustical Society of America* 71 (1982) 359–367.
- [84] S. Chae, M. Trivedi, M. El-Gindy, I. Johansson, F. Öijer, Dynamic response predictions of a truck tire using detailed finite element and rigid ring models, in: 2004 ASME International Mechanical Engineering Congress and Exposition, IMECE, Anaheim, USA, 13–19 November 2004, volume 117, pp. 861–871.
- [85] X. Zhang, S. Rakheja, R. Ganesan, Modal analysis of a truck tyre using FE tyre model, *Heavy Vehicle Systems-International Journal of Vehicle Design* 11 (2004) 133–154.
- [86] A. Miège, A. Popov, Truck tyre modelling for rolling resistance calculations under a dynamic vertical load., *Proceedings of the Institution of Mechanical Engineers – Part D – Journal of Automobile Engineering* 219 (2005) 441–456.
- [87] P. Dinkova, W. Kropp, Modeling the vibrational response of truck tyres, in: *Proceedings of Euronoise 2006*, 30 May – 1 June 2006, Tampere, Finland.
- [88] T. Clapp, A. Eberhardt, C. Kelley, Development and validation of a method for approximating road surface texture-induced contact pressure in tire-pavement interaction, *Tire Science and Technology* 16 (1988) 2–17.

-
- [89] G. Dubois, J. Cesbron, H. Yin, F. Anfosso-Lédée, Macro-scale approach for rough frictionless multi-indentation on a viscoelastic half-space, *Wear* 272 (2011) 69–78.
- [90] J. Winroth, P. Andersson, Influence of tread inertia during deformation using a detailed numerical tyre/road contact model, in: *Proceedings 6th Forum Acusticum*, Aalborg, Denmark, 2011, EAA, pp. 2431–2436.
- [91] H.-P. Yin, G. Dubois, J. Cesbron, F. Anfosso-Lédée, Q.-H. Bui, D. Duhamel, A numerical macro-scale approach for the tire/road viscoelastic contact for the noise prediction, in: *Proceedings of the Internoise 2012/ASME NCAD meeting August 19-22, 2012*, New York City, USA.
- [92] M. McIntyre, J. Woodhouse, On the fundamentals of bowed string dynamics, *Acustica* 43 (1979) 93–108.
- [93] W. Kropp, A mathematical model of tyre noise generation, *International Journal of Vehicle Design* 6 (1999) 310–329.
- [94] W. Kropp, Ein Modell zur Beschreibung des Rollgeräusches eines unprofilier-ten Gürtelreifens auf rauher Straßenoberfläche, number 166 in *Fortschritt-berichte VDI, Reihe 11: Schwingungstechnik*, VDI Verlag, 1992.
- [95] K. Larsson, S. Barrelet, W. Kropp, The modelling of the dynamic behaviour of tyre tread blocks, *Applied Acoustics* 63 (2002) 659–677.
- [96] F. Wullens, W. Kropp, A three-dimensional contact model for tyre/road interaction in rolling conditions, *Acta Acustica united with Acustica* 90 (2004) 702–711.
- [97] P. Andersson, W. Kropp, Time domain contact model for tyre/road interaction including nonlinear contact stiffness due to small-scale roughness, *Journal of Sound and Vibration* 318 (2008) 296–312.
- [98] J.-F. Hamet, P. Klein, Road texture and tire noise, in: *Proceedings Inter-noise 2000, 27-30 August 2000*, Nice, France, pp. 178–183.
- [99] R. Graf, Tyre-road interaction noise, Ph.D. thesis, University of Cambridge, 2002.
- [100] F. Liu, M. Sutcliffe, W. Graham, Prediction of tread block forces for a free-rolling tyre in contact with a smooth road, *Wear* 269 (2010) 672–683.
- [101] I. Lopez Arteaga, Green’s functions for a loaded rolling tyre, *International Journal of Solids and Structures* 48 (2011) 3462–3470.

-
- [102] S. Boere, I. Lopez Arteaga, A. Kuijpers, H. Nijmeijer, Tyre/road interaction model for the prediction of road texture influence on rolling resistance, *International Journal of Vehicle Design* 65 (2014) 202–221.
- [103] R. Pinnington, Tyre–road contact using a particle–envelope surface model, *Journal of Sound and Vibration* 332 (2013) 7055–7075.
- [104] S. Kim, A. Savkoor, The contact problem of in-plane rolling of tires on a flat road, *Vehicle System Dynamics* 27 (1997) 189–206.
- [105] S. Kim, P. Nikraves, G. Gim, A two-dimensional tire model on uneven roads for vehicle dynamic simulation, *Vehicle System Dynamics* 46 (2008) 913–930.
- [106] F.-X. Bécot, Tyre noise over impedance surfaces — Efficient application of the equivalent sources method, Ph.D. thesis, Chalmers University of Technology Gothenburg/INSA Lyon, 2003.
- [107] E.-J. Ni, D. Snyder, G. Walton, N. Mallard, G. Barron, J. Browell, B. Aljundi, Radiated noise from tire/wheel vibration, *Tire Science and Technology* 25 (1997) 29–42.
- [108] H. Brick, Application of the Boundary Element Method to combustion noise and half-space problems, Ph.D. thesis, Chalmers University of Technology, 2009.
- [109] W. Graham, Influence of tire geometry on the horn effect, in: *Proceedings of the Internoise 2012/ASME NCAD meeting August 19-22, 2012, New York City, NY, USA*.
- [110] D. Brunner, Fast Boundary Element Methods for Large-Scale Simulations of the Vibro-Acoustic Behavior of Ship-Like Structures, Ph.D. thesis, Universität Stuttgart, 2009.
- [111] S. Keuchel, J. Biermann, M. Gehlken, O. von Estorff, Speed up of 3D-acoustics in frequency domain by the Fast Multipole Method in combination with Krylov Subspace Recycling based iterative solvers, in: *AIA-DAGA 2013 Conference on Acoustics, EAA Euroregio/EAA Winter School, 18–21 March 2013 in Merano, Italy*, pp. 1995–1998.
- [112] C. Bückers, U. Stöckert, Quiet Road Traffic 3 - An interdisciplinary approach to reduce the noise emission at the source, in: [156].
- [113] C.-Y. Kuo, R. Graf, A. Dowling, W. Graham, On the horn effect of a tyre/road interface, part ii: Asymptotic theories, *Journal of Sound and Vibration* 256 (2002) 433–445.

-
- [114] P. Pillai, Total tire energy loss comparison by the whole tire hysteresis and the rolling resistance methods, *Tire Science and Technology* 23 (1995) 256–265.
- [115] L. Yam, J. Shang, D. Guan, A. Zhang, Study on tyre rolling resistance using experimental modal analysis, *International Journal of Vehicle Design* 30 (2002) 251–262.
- [116] D. Stutts, W. Soedel, A simplified dynamic model of the effect of internal damping on the rolling resistance in pneumatic tires, *Journal of Sound and Vibration* 155 (1992) 153–164.
- [117] H. Park, S.-K. Youn, T. Song, N.-J. Kim, Analysis of temperature distribution in a rolling tire due to strain energy dissipation, *Tire Science and Technology* 25 (1997) 214–228.
- [118] K. Rao, R. Kumar, P. Bohara, A sensitivity analysis of design attributes and operating conditions on tyre operating temperatures and rolling resistance using finite element analysis., *Proceedings of the Institution of Mechanical Engineers – Part D – Journal of Automobile Engineering* 220 (2006) 501–517.
- [119] Y.-J. Lin, S.-J. Hwang, Temperature prediction of rolling tires by computer simulation, *Mathematics and Computers in Simulation* 67 (2004) 235–249.
- [120] J. Cho, H. Lee, W. Jeong, K. Jeong, K. Kim, Numerical estimation of rolling resistance and temperature distribution of 3-D periodic patterned tire, *International Journal of Solids and Structures* 50 (2013) 86–96.
- [121] P. Ghosh, A. Saha, R. Mukhopadhyay, Prediction of tyre rolling resistance using FEA, in: J. Busfield, A. Muhr (Eds.), *Constitutive Models for Rubber III*, Swets & Zeitlinger, Lisse, 2003.
- [122] J. Luchini, J. Peters, R. Arthur, Tire rolling loss computation with the finite element method, *Tire Science and Technology* 22 (1994) 206–222.
- [123] R. Ali, R. Dhillon, M. El-Gindy, F. Öjier, I. Johansson, M. Trivedi, Prediction of rolling resistance and steering characteristics using finite element analysis truck tyre model, *International Journal of Vehicle Systems Modelling and Testing* 8 (2013) 179–201.
- [124] D. Duhamel, B. Mace, M. Brennan, Finite element analysis of the vibrations of waveguides and periodic structures, *Journal of Sound and Vibration* 294 (2006) 205–220.
- [125] L. Gavric, Computation of propagative waves in free rail using a finite element technique, *Journal of Sound and Vibration* 185 (1995) 531–543.

-
- [126] A. Pieringer, Time-domain modelling of high-frequency wheel/rail interaction, Ph.D. thesis, Chalmers University of Technology, Gothenburg, 2011.
- [127] Y. Fung, P. Tong, Classical and computational solid mechanics, World Scientific, Singapore, 2001.
- [128] K. Larsson, Modelling of dynamic contact — Exemplified on the tyre/road interaction, Ph.D. thesis, Chalmers University of Technology, Gothenburg, 2002.
- [129] G. Gilardi, I. Sharf, Literature survey of contact dynamics modelling, *Mechanism and Machine Theory* 37 (2002) 1213–1239.
- [130] SPERoN acoustic optimization tool, <http://www.speron.net>, last visited 14/08/2014.
- [131] R. Ciskowski, C. Brebbia (Eds.), *Boundary Element Methods in Acoustics, Computational Mechanics Publications*, Co-published with Elsevier Applied Science, Southampton, Boston, London, New York, 1991.
- [132] Y. J. Kim, J. Bolton, Effects of rotation on the dynamics of a circular cylindrical shell with application to tire vibration, *Journal of Sound and Vibration* 275 (2004) 605–621.
- [133] S. Vercammen, P. Kindt, C. González Díaz, W. Desmet, Analyses on the effects of rolling on the tire dynamics, in: *Internoise 2013, The 42nd International Congress and Exposition on Noise Control Engineering*, Innsbruck, 15.-18. Sept. 2013, I-INCE, I-INCE, 2013.
- [134] Tyre Basics Passenger Car Tyres, Technical Report 0130 1607, Continental Reifen Deutschland, 2012.
- [135] D. O’Boy, A. Dowling, Tyre/road interaction noise — A 3D viscoelastic multilayer model of a tyre belt, *Journal of Sound and Vibration* 322 (2009) 829–850.
- [136] K. Altena, WFEM applied to a car tyre, Master’s thesis, TU Delft, The Netherlands, 2007.
- [137] W. Soedel, *Vibrations of Shells and Plates*, Marcel Dekker, New York, 3rd edition, 2004.
- [138] J. Halpin, *Primer on composite materials analysis*, Technomic Publishing Company, Lancaster, Basel, 2nd edition, 1992.
- [139] R. Jones, *Mechanics of composite materials*, Taylor & Francis, Philadelphia, 2nd edition, 1999.

-
- [140] S. Finnveden, C.-M. Nilsson, Waveguide Finite Elements for Analysis of Car Tyre Vibrations, RATIN Deliverable D1.2.3, 2003.
- [141] M. Petyt, Introduction to finite element vibration analysis, Cambridge University Press, Cambridge, 1990.
- [142] C. Hoever, The influence of modelling parameters on the simulation of car tyre rolling losses and rolling noise, Licentiate thesis, Chalmers University of Technology, Gothenburg, 2012.
- [143] International Organization for Standardization ISO 10844:2011 Acoustics – Specification of test tracks for measuring noise emitted by road vehicles and their tyres, 2011.
- [144] International Organization for Standardization ISO/TS 13473-4:2008 Characterization of pavement texture by use of surface profiles — Part 4: Spectral analysis of surface profiles, 2008.
- [145] A. Pieringer, W. Kropp, D. Thompson, Investigation of the dynamic contact filter effect in vertical wheel/rail interaction using a 2D and a 3D non-Hertzian contact model, *Wear* 271 (2011) 328–338.
- [146] S. Boere, G. van Blokland, Influence of road surface properties on rolling resistance of car tyres, Technical Report M+P.DVS.08.17.1, M+P - consulting engineers, 2008.
- [147] W. Schwanen, H. van Leeuwen, A. Peeters, G. van Blokland, H. Reinink, W. Kropp, Acoustic Optimization Tool — RE3: Measurement data Kloosterzande test track, Technical Report M+P.DWW.06.04.8, M+P - consulting engineers, 2007.
- [148] International Organization for Standardization ISO 13473-2:2002 Characterization of pavement texture by use of surface profiles — Part 2: Terminology and basic requirements related to pavement texture profile analysis, 2002.
- [149] M. Roovers, D. de Graff, R. van Moppes, Round Robin Test Rolling Resistance / Energy Consumption, Technical Report DWW-2005-046, IPG, 2005.
- [150] U. Kunert, S. Radke, D. Chlond, M. Kagerbauer, Auto-Mobilität: Fahrleistungen steigen 2011 weiter, *DIW Wochenbericht* 47.2012 (2012) 3–14.
- [151] E. Schreurs, L. Brown, D. Tomerini, Maximum pass-by noise levels from vehicles in real road traffic streams: Comparison to modeled levels and measurement protocol issues, in: *Proceedings of Internoise 2011*, September 4-7, 2011, Osaka, Japan.

-
- [152] D. Ewins, *Modal Testing: Theory, Practice and Application*, Research Studies Press, Baldock, 2nd edition, 2000.
- [153] C. Hoever, W. Kropp, A simulation-based parameter study of car tyre rolling losses and sound generation, in: [156], pp. 926–931.
- [154] P. Andersson, K. Larsson, Validation of a high frequency tyre model based on the elastic field equations, in: 10th International Congress on Sound and Vibration, July 7-10 2003, Stockholm, Sweden.
- [155] *Internoise 2001*, The 2001 International Congress and Exhibition on Noise Control Engineering, The Hague, The Netherlands, 2001 August 27-30, 2001.
- [156] *Euronoise Prague 2012*, 10-13 June 2012, 2012.

